ROTORDYNAMIC ENHANCEMENT BY UTILIZING THE CONTROLLED HYDROSTATIC INJECTION OF HYBRID AIR FOIL BEARING

by

Behzad Zamanian Yazdi

Presented to the Faculty of the Graduate School of

The University of Texas at Arlington in Partial Fulfillment

of the Requirements for the Degree of

DOCTOR OF PHILOSOPHY

THE UNIVERSITY OF TEXAS AT ARLINGTON
November 2017

DEDICATION

To my parents who endlessly loved and supported me.

ACKNOWLEDGEMENTS

I would like to express my deepest appreciation to Dr. Daejong Kim for his guidance and support throughout the course of my research. I was very fortunate to have him as my academic advisor. Dr. Kim has always motivated me and his passion and dedication have been extremely inspirational for me. I am also grateful to Dr. Alan bowling, Dr. B. P. Wang, Dr. Kyung Suk Yum, and Dr. Kent Lawrence for serving as my committee members.

I want to express my gratitude to the UTA machine shop, specially, Mr. Kermit Bird for his constant support and assistance at each stage in the fabrication of the foil bearings and test rig components.

I would like to thank all my friends at UTA. Special thank goes to Hamideh Riazi who has always gave me emotional support to overcome every difficulty encountered during this work. Finally, this work was not possible without endless love and unconditional support of my parents during all these years.

Dr. Daejong Kim has a potential research conflict of interest due to a financial interest with company Bellkim Energy LLC. A management plan has been created to preserve objectivity in research in accordance with UTA policy.

November 12, 2017

ABSTRACT

ROTORDYNAMIC ENHANCEMENT BY UTILIZING THE CONTROLLED HYDROSTATIC INJECTION OF HYBRID AIR FOIL BEARING

Behzad Zamanian Yazdi, PhD

The University of Texas at Arlington, 2017

Supervising Professor: Daejong Kim

Air foil bearings (AFBs) are introduced as promising bearings for oil-free turbomachinery applications. Air foil bearing (AFB) technology has made substantial advancement during the past decades and found its applications in various small turbomachinery. AFBs provide reliable operation at high speed and high temperature with negligible power loss. However, rotordynamic instability, friction and drag during the start/stop, and thermal management are still challenges for further application of the technology. Hybrid Air Foil Bearing (HAFB) technology utilizes the radial injection of externally pressurized air into the traditional hydrodynamic AFB's film thickness through orifices attached to the top foil. HAFB is one of the technology advancements to the conventional AFB. Previous studies on HAFBs demonstrate the enhancement in the load capacity at low speeds, reduction or elimination of the friction and wear during starts/stops, better heat dissipation capability, and enhancement in rotordynamic stability. This dissertation is dedicated to explore the benefit of the HAFB to enhance the rotordynamic stability by employing a controlled hydrostatic injection. Moreover, this dissertation investigates the effect of circumferential location of radial injection on the rotordynamic performance of HAFB.

Analytical and experimental evaluations of the rotordynamic performance of a rotor supported by two HAFBs with the controlled hydrostatic injection, which utilizes the injections at particular locations to control eccentricity and attitude angle are presented.

To investigate the effect of circumferential location of orifices, parametric studies are conducted using three sets of single-pad HAFBs. The circumferential locations of orifices are different for each set.

The presented simulation analyses consist of time-domain orbit simulation and frequency-domain modal analysis. The simulations in both time-domain orbit simulations and frequency-domain modal analyses indicate a substantial improvement of the rotor-bearing performance. The simulation results were verified in a high speed test rig (maximum speed of 70,000 rpm). Both simulations and experiments clearly demonstrate the effectiveness of the controlled hydrostatic injection on improving the rotordynamic performance of AFB. Imbalance responses of rotor-HAFB were measured with various orifice locations and the results agree well with predictions. Comparison of the rotordynamic performance of HAFBs with different orifice configurations demonstrate substantial improvement in rotordynamic stability as well as enhancement in the stiffness and damping coefficients of HAFBs by choosing the best circumferential location for radial injection to control rotor eccentricity and attitude angle.

TABLE OF CONTENTS

LIST OF FIGURES

LIST OF TABLES

NOMENCELATURE

A_{bump}	Effective area of a single bump [m^2]
A_o	Effective orifice area [m^2]
C	Bearing nominal radial clearance [m]
C_{bump}	Bump equivalent viscous damping coefficient [N m/sec]
C_d	Orifice discharge coefficient
C_m	Bearing set bore clearance [m]
c_p, c_v	Specific heat [J/K]
$C_{XX}, C_{XY}, C_{YX}, C_{YY}$	Bearing damping coefficient [N m/sec]
D	Bearing inner diameter [m]
$\hat{D}$	Empirical load capacity coefficient
d_o	Orifice diameter [m]
e_X, e_Y	Rotor eccentricity [m]
e_{X0}, e_{Y0}	Rotor center eccentricity at equilibrium position [m]
F_{brg_X}, F_{brg_Y}	Bearing reaction forces [N]
F_{imb_X}, F_{imb_Y}	Imbalance forces [N]
f_{bump}	Pressure force acting on a single bump [N]

g	Gravitational acceleration $[\mathrm{m/s^2}]$
h	Local fluid film thickness [m]
I_P, I_T	Polar and translation moments of inertia $[\mathrm{kg\ m^2}]$
K_{bump}	Bump stiffness [N m]
$\hat{i}, \hat{j}, \hat{k}$	Unit vectors
k	Specific heat ratio
$K_{XX}, K_{XY}, K_{YX}, K_{YY}$	Bearing stiffness coefficient [N m]
L	Bearing axial length [m]
L_b	Bearing span [m]
L_r	Rotor length [m]
l_i	Imbalance mass axial location [m]
$M_{brg\_\xi}, M_{brg\_\psi}$	Moment to rotor due to the bearing force [N m]
$M_{imb\_\xi}, M_{imb\_\psi}$	Moment to rotor due to imbalance force [N m]
m_R	Rotor mass [kg]
$\dot{m}_s$	Air mass flow rate [kg/sec]
N_{bumps}	Number of bumps per pad
p_a	Ambient pressure [Pa]
p_j	Hydrodynamic pressure in gas film [Pa]

p_s	Supply pressure into the orifice [Pa]
p_X, p_Y	Perturbed pressure
R	Rotor radius [m]
R_g	Gas constant
r_p	Bearing hydrodynamic preload [m]
T	Temperature [K]
t	Time [sec]
u	Bump deflection [m]
u_i	Imbalance radius [m]
W	Applied load [N]
w_j	Elastic deflection of top foil and bump foil [m]
x, y, z	Inertial reference coordinate [m]
Z_1, Z_2	Bearing modal impedance
Z_i	Bearing center line axial coordinate [m]
$Z_{XX}, Z_{XY}, Z_{YX}, Z_{YY}$	Bearing impedances
z_j	Axial local coordinate in the bearing [m]
η	Structural loss factor
Γ	Feed parameter
Λ	Bearing number

γ	Offset ratio
υ	Excitation frequency ratio
θ	Circumferential coordinate [rad]
θ_{pad}	Top foil angular width [rad]
θ_{SB}	Angular location of set bore clearance [rad]
ω	Rotational speed of the rotor [rad/sec]
ω_s	Excitation frequency [Hz]
ξ, ψ	Rotations of rotor about X and Y axes [rad]
μ	Dynamic viscosity [Pa sec]
ϕ	Attitude angle[rad]

Chapter 1

INTRODUCTION

Designing a reliable and high performance bearing is one of the most crucial challenges in any high-speed turbomachinery system. The conventional oil-lubricated bearings show low performance or even fail to operate for applications with relatively high temperatures and high surface speeds [1]. Utilization of the oil-lubricated bearings increases the overall system's complexity and cost of maintenances, as well as decreases the overall efficiency of the system. As an example, in a 3 KW micro-gas turbine there is a power loss of about 900 W due to the poor operation of the oil-lubricated bearings [2]. The conventional oil-lubricated bearings are harmful to the environment because of the hazardous chemical components in the petroleum-based lubricants. Numerus limitations of oil-lubricated bearings and the fact that todays advanced turbomachinery systems often require operating in the extreme temperatures and speeds have been the motivation of the researchers for decades to develop and improve oil-free bearings as a substitute for oil-lubricated bearings.

Oil-free bearings consist of magnetic bearings, rigid-walled gas bearings, and air foil bearings. The magnetic bearings require complicated controllers, and an external power source to supply electricity and maintain the magnetic field. Magnetic bearings always need another type of mechanical bearing as a backup bearing for the case of power outage. Due to the existence of backup bearings, the overall weight and complexity of a turbomachinery system increases. Rigid-walled gas bearings ten suffers from a very poor stability characteristics at high speeds therefore they are not suitable for high-speed applications.

1. 1. Air foil bearing

Air foil bearings (AFBs) are hydrodynamic air-lubricated bearings with a compliant bearing surface that provides stiffness and damping to the bearing. AFB technology has made substantial advancement during the past decades and found its applications in various small turbomachinery. AFBs operate well at high temperatures and high speeds with negligible power loss. Oil-free operation of AFBs reduces scheduled maintenances/costs and eliminates environmental risks. Elimination of the oil lubricating systems in the traditional oil-lubricated rotor-bearing systems results in a compact and simpler system configuration. Compare to the rigid-walled air bearing, AFB show higher rotordynamic stability due to the improved damping mechanism from the compliant support structure [3]. Higher film thickness of AFB in comparison to the rigid-walled air bearing provides a solution to overcome the manufacturing tolerances, minor shaft misalignments, and external shocks, and the problems related to the thermal expansion of the rotor and bearing. Successful applications of the AFB have been found in small high-speed oil-free turbomachinery. One of the first commercialized applications of the AFB is in the air cycle machine (ACM) of the Boeing 747 aircraft. The ACM that operates by AFB on the 747 aircraft has a proven lifetime before failure over 100,000 hours [4]. Successful applications of AFB in oil-free micro gas turbines [5, 6], and micro gas turbines for the bottoming cycle device for solid oxide fuel cells [7-9] are reported. AFB consists of three main components: (1) bearing surface (top foil), (2) compliant support structure which provides stiffness and damping to the bearing, (3) and bearing sleeve (Figure 1-1). AFB comprises one or multiple compliant support structures underneath the bearing surface (top foil). The compliant structure and the top foil are fixed inside the bearing sleeve. The compliant support structure enables AFBs to accommodate minor shaft misalignment and shaft distortions due to thermal and

centrifugal loads. Researchers introduced several types of compliant structures such as corrugated bump foils, compression springs [10,11], and metal mesh material [12-14]. Ertas [12, 15] proclaim the favorable effect of the metal mesh material, as a support structure, on the stability of the AFB. However, as reported in [16], AFB with the metal mesh has a lower stiffness than the typical bump foil AFB, which may result in a lower damping coefficient even if the loss factor of metal mesh AFB is higher than bump foil AFB. Lee et al [17] estimated the linear stiffness coefficient and the damping loss factor of the metal mesh AFB with different metal mesh densities. The results showed that, in order to increase the linear stiffness and the loss factor of the metal mesh AFB, a relatively high mesh density is required.

The most common type of compliant support structure for AFB is a corrugated bump foil structure (as shown in Figure 1-1) because of ease manufacturing and predictable stiffness and damping characteristics. The typical materials for AFB bump foil and top foil is the nickel-based super-alloys because of their outstanding mechanical properties at high temperature, excellent corrosion resistance, and acceptable surface stability. DellaCorte et al [18] present the fabrication method of the bump-type gas foil bearing. The manufacturing process of the foils involves cold forming followed by heat treatment to remove the stresses generated during the forming process and to achieve the desirable elastic property.

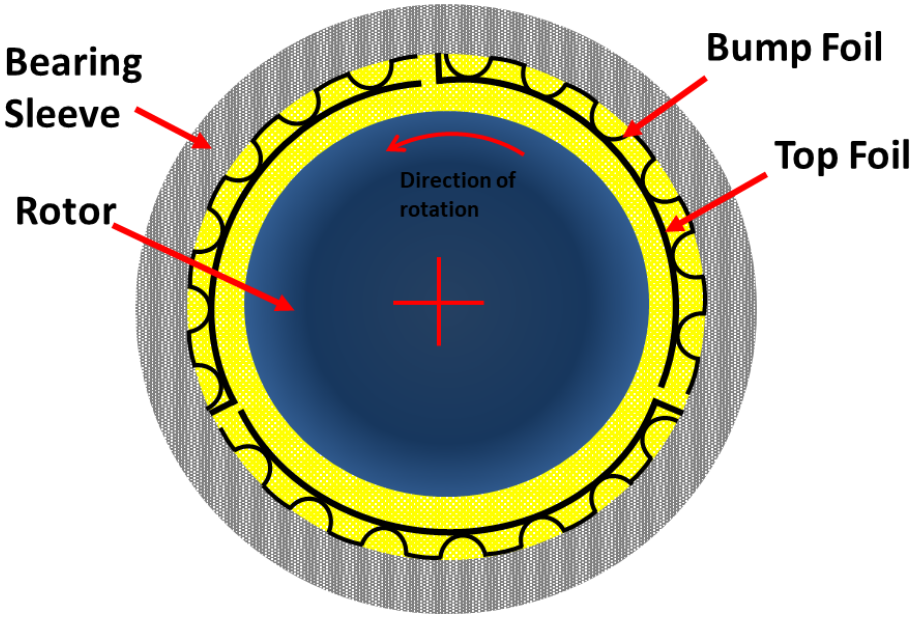

Figure 1-1 Schematic of a three-pad bump type air foil bearing

AFBs are operating by the hydrodynamic pressure build-ups within the small gap (film) between the top foil and the rotating shaft surface. The pressure within the film (bearing clearance) is generated by two mechanisms. The first mechanism is the wedge effect between top foil and shaft surface. When bearing sleeve is stationary and shaft is rotating, two converging surfaces are formed to maintain the airflow and the pressure build-ups between top foil and shaft surface. The second mechanism is the squeeze film effect. Because of the sudden squeeze of the air film inside the bearing clearance, a positive pressure is generated inside the air film.

Due to the operating nature of AFB, excessive friction and rubbing between bearing surface and shaft is generated during system start/stop. To mitigate the adverse effect of the rubbing and friction on the lifetime of the bearing, and reduce the friction between bearing surface and shaft, a low friction surface coating (such as Teflon® for applications at lower temperatures) is usually applied on the top foil [19-21].

1. 2. Foil bearing characteristics

DellaCorte and Valco [22] conducted empirical studies on the foil bearing load carrying capacity. They used existing experimental data from prior published literature with their own experimental studies and developed a rule of thumb (ROT) to estimate AFB load carrying capacity. They claimed that the load carrying capacity of AFB is a function of bearing axial length, journal diameter, and rotational speed. The ROT model can be expressed by:

$$W = \hat{D}(L \times D)(D \times \omega) \qquad (1\text{-}1)$$

, where W is the maximum constant load to the AFB at steady-state condition and at constant rotational speed, $\hat{D}$ is a load capacity coefficient, L is the bearing axial length, D is the journal diameter, and ω is the shaft rotational speed. Bearing load capacity coefficient ($\hat{D}$) is related to the bearing compliant support design features (bump foil geometries and bump foil arrangement), and operating conditions (operating speed and ambient temperature). The proposed ROT model does not consider some factors such as bearing hydrodynamic preload, nominal clearance, bearing surface condition (top foil coating), gas density, and operating temperature, among others. Kim [23] conducted numerical parametric studies on the static performance of AFBs under variation of the bump stiffness and bearing's geometry. From the load capacity analysis, he suggested that the stiffness variation in the AFB's support structure has a minor effect on bearing load carrying capacity, which contradicts the previous study by DellaCorte et al [22], in which they claimed that by tailoring the bearing support stiffness, the load carrying capacity can be enhanced by up to five times. Kim [23] reported that AFB geometries variation and radial clearance have a significant effect on the bearing load carrying

capacity, i.e., a single-pad AFB has a larger load carrying capacity than a three-pad AFB regardless of the bump stiffness variation within the bearing.

Bruckner et al [24] performed experimental studies on the load carrying capacity of AFBs with different boundary pressures and temperatures. For the experimental analysis they used a coated journal (PS304 coating) and they tests are performed for temperature range of 25 to 500 C and ambient pressure range of 0.1 to 2.5 bar. Authors reported an increase in AFB load carrying capacity by increasing the ambient pressure and reduction in the AFB load carrying capacity by increasing the ambient temperature. DellaCorte et al [25, 26] presented a foil bearing performance map based on the experimental studies. The proposed performance map is useful for early design stages to identify AFB operating regimes. The AFB performance map presents a performance safety margins for AFB based on the bearing load and other limiting factors.

Thermal runaway and low stability are among the main limiting factors which cause failure in the AFBs. Radial et al [27] showed that the AFBs are usually subjected to a thermal runaway failure when the operating clearance is too small. They suggest that an appropriate radial clearance is crucial for the AFBs to avoid the thermal runaway. However, if clearance is too large, the load capacity of the bearing is compromised. Dykas et al [28] presented journal design guidelines to prevent thermal runaway. They suggested that a thicker-walled journal helps to prevent failure related to the centrifugal expansion of the bearing journal. However, using a thick-walled bearing journal increases the overall weight of the system, which is a negative factor especially in aerospace applications. In addition, they suggested that, using a small amount of air through the underlying compliant structure can help to avoid the thermal seizure and related bearing failure. Injection of externally pressurized air in the leading edge groove region is reported as an alternative solution for the thermal management of AFBs [29, 30].

Shrestha et al [29] implemented the radial air injection into the leading edge grooves for the thermal management of a three-pad AFB. They compared the effectiveness of the axial cooling versus the radial injection cooling. They reported that the axial cooling is not effective beyond certain journal speed when the pressure drop across bearing becomes significant. However, the effectiveness of the radial injection cooling is not affected by journal speed as long as the injection speed exceeds rotor surface speed. Radil and Batcho [30]. studied the feasibility of radial air injection for thermal management of a single-pad AFB. However, the air injection speed was low through relatively large injection holes in their experiment, which resulted in poor cooling performance compare to the other traditional thermal management methods.

1. 3. Foil bearing force coefficients and predictive models

Many researchers presented numerical models to predict AFB force coefficients and rotordynamic performance. Ku and Heshmat [31] developed an analytical model to predict the bump foil stiffness by considering friction forces between the top foil and bump foil, and between the bearing sleeve and bump foil, as well as, the local interactive force between bumps. They presented the equivalent friction coefficient and overall stiffness of the bump foil strip under various load distributions. Authors reported that the bumps near the fixed-end have higher stiffness than the bumps near the free -end. Because the fixed bumps have much lower deflection under static load. It is shown that an increase in the friction coefficient between the bump foil and the top foil results in a higher Coulomb damping and higher stiffness. In addition, increasing the bump thickness or bump height and decreasing the bump length increases the stiffness. Same authors in another study [32] developed a model to predict damping characteristics of a bump foil strip. In the proposed model, the structural stiffness was calculated for a small perturbation of the journal center around its static equilibrium position. The equivalent viscous damping

coefficients were calculated from the area of a closed hysteresis loop of the journal center motion. It was reported that the bump foil strip acts as a nonlinear spring-damper, and that the stiffness and damping coefficients are a function of static journal eccentricity, perturbation amplitude, and excitation frequency.

Peng and Caprine [33] investigated the effect of Coulomb friction damping on the damping and stiffness coefficients of a bump foil structure. Authors developed a model to predict the stiffness and damping coefficients. A perturbation method was used to find the dynamic coefficients. It was shown that the friction force due to the sliding motion of the bump foil structure to the bearing sleeve generates the damping. It was reported that as bearing number increases or the minimum clearance decreases the stiffness coefficient increases.

Ku and Heshmat [34] conducted experimental analysis to calculate the structural stiffness of bump foil strips and validate the previous theoretical model presented by the authors. They used a series of load-deflection tests for different operating conditions and measured the two-dimensional deflection of a bump foil strip (horizontal and vertical deflections). It was reported that the bump foil thickness has a small effect on the local stiffness. Also, it was shown that reducing the pitch of the bump foil strip increases the local stiffness dramatically. As for the bump foil's surface coating, having a higher friction coefficient between the bump foil, top foil and the bearing sleeve result in a higher stiffness coefficient. Heshmat and Ku [35] experimentally evaluated the dynamic characteristics of a bump-type AFB. The authors utilized two shakers to introduce dynamic loads on a non-rotating journal supported by bump foil strips. The dynamic structural stiffness and equivalent viscous damping of the bump foil stripes were calculated for a wide range of operating conditions. The results showed that the bump foil's direct stiffness and damping decreases as the amplitude of dynamic load increases.

As the shaker excitation frequency increases, the direct damping decreases whereas the direct stiffness increases. However, later experimental studies from different authors [11, 36, 37] showed that the direct damping increases as the amplitude of the dynamic load increases. Rubio and San Andres [36] measured the stiffness and damping coefficients of AFBs under dynamic load. They show that stiffness decreases and equivalent viscous damping coefficient increases as the amplitude of dynamic load increases. Song and Kim [11] measured the frequency-dependent stiffness and damping coefficients of an AFB with a series of compression springs as support structure of top foil. They report increases in damping coefficient and decreases in stiffness coefficient as the frequency of the dynamic load increases.

Howard [38, 39] presented an experimental study to measure AFB's steady-state stiffness under variation of static load, operating temperature, and rotor speed using a high speed foil bearing test rig operating at high temperature. The steady-state stiffness of an AFB was evaluated while a known external load was applied to the bearing (vertical direction), and the resulting displacement was measured using a fiber optic displacement probe. The steady-state stiffness is defined as the applied external load divided by the bearing sleeve's displacement. Authors reported that the AFB's steady-state stiffness increases as the magnitude of the external load increases. However, the steady-state stiffness decreases as the rotor speed increases under a fixed static external load. Moreover, it was reported that the AFB's stiffness drops as the operating temperature increases. Howard et al [40] measured the dynamic stiffness and damping of an AFB. An impact hammer was used to deliver an impact load to the bearing housing. The frequency of the vibration decay was measured to calculate the dynamic stiffness, and the rate of decay was measured to calculate the damping coefficient.

1. 4. Rotordynamic measurements

Rotordynamic instability is one of the main challenges for the operation of AFBs. AFBs can usually operate at very high speeds, but any rotor-bearing instability can lead to a catastrophic failure. Rotordynamic analysis is an important tool to ensure the stable operation of rotor-AFBs. Rotordynamic analysis is usually performed through imbalance response measurements of rotor-bearing systems to identify the critical speeds and detect the existence of the onset speed of instability. Simulation tools are also available in the literature to predict the rotor vibrations under imbalance forces.

Circular hydrodynamic AFBs with single top foil tend to have a poor rotordynamic stability, and they often require very large bearing clearance to make the rotor stable [23]. Heshmat et al [41] introduced a three-pad bump foil AFB with the angular stiffness variation in the bump foil strip (the design was claimed to provide superior rotordynamic stability characteristics). In the proposed three-pad AFB, the bump foils were welded to the top foil at the trailing edge of each pad. Because of the weld juncture at the trailing edge, the stiffness of the bump foil strip reduces from the trailing edge (welded end) toward the leading edge (free end). Having a variable stiffness provides a lobing effect due to the hydrodynamic pressure gradient. As the hydrodynamic pressure builds up, pads are forced outward and they form a converging wedge (the lobing effect provides a varying preload along each pad). The lobing effect is more pronounced at higher speeds due to higher hydrodynamic pressure. Stiffness variation along the pads was measured by a load-deflection test. The test results demonstrate that the proposed three-pad AFB has excellent rotordynamic stability when the rotor is rotating in the direction from the free-end of the pads toward the welded-end. Tests with different in-phase imbalance masses showed that the onset speed of instability is inversely proportional to the magnitude of the rotor imbalance level. San Andres et al [42] conducted experimental

and numerical analysis on rotordynamic performance of a rotor supported by two AFBs. The measured imbalance response with a large imbalance shows large subsynchronous motion at low frequencies, and they claim the large imbalance is the source of subsynchronous vibration. Balducchi et al [43] conducted experimental analysis on stability of a rotor supported by AFBs. The static measurements showed an anisotropic behavior of AFB, which comes from an improper manufacturing process. This can be reduced significantly by using precise and more accurate manufacturing methods. Moreover, the imbalance response of the rotor under different unbalance residues showed that the stability decreases by increasing the imbalance mass; their findings are contrary to the claim in [42]. The authors used a theoretical model to simulate the experimental results, but the results from the theoretical model have limited agreement with the experimental results.

Kim [23] conducted parametric studies on the rotordynamic performance of AFBs under variation of bearing geometries. It was reported that the rotor-bearing stability is much more sensitive to the overall bearing shape than bump foil stiffness variation. Stability analysis showed a much better stability for the three-pad AFB compared to the single-pad AFB. Kim and San Andres [44] investigated the effect of side flow through an AFB on the rotor-bearing stability. The authors claimed that when the axial flow is forced into the bearing's film, the amplitude of the subsynchronous vibration decreases, and it disappears under relatively very high feed pressures. However, it should be pointed out that the high feed pressure results in a high air consumption, which is impractical.

Sim et. al [45] showed that the hydrodynamic preload have a beneficial effect on the AFB stability. Increasing the hydrodynamic preload increases the onset speed of subsynchronous vibration. However, prediction showed that the damping coefficient decreases as the hydrodynamic preload increases, which seems contrary to their claim

that the hydrodynamic preload increases the stability. LaTray and Kim [46] evaluated the rotordynamic performance of AFBs supporting a rotor with a large overhung mass for high-speed applications. The rotor-AFB configuration had a large overhung mass at one end of the rotor. A high-speed rotordynamic test rig was used for experimental evaluation. In the high-speed test rig, a pair of two-pad AFBs supported the rotor's radial motion, and the rotor's axial motion was constrained by a pair of six-pad air foil thrust bearings. The high-speed rotordynamic test rig was driven by an impulse turbine which can operates up to 185,000 rpm. The authors presented both analytical and experimental analyses. On the analytical part, three different approaches (non-linear rigid shaft, linear flexible shaft, and non-linear flexible shaft) for modeling rotor-AFB were presented and the effectiveness of all three methods to accurately predict the rotordynamic performance was compared. High speed tests showed stable steady-state operation for up to 160,000 rpm with a small bounded subsynchronous vibration, however the simulated imbalance responses didn't show subsynchronous rotor vibration up to 200,000 rpm.

1. 5. Hybrid air foil bearing

Although AFB demonstrate promising improvements for the oil-free turbomachinery, there still exist some drawbacks their performance. One of the limitations of AFB is the lower stability in comparison to the roller element bearings. Friction and wear between the bearing surface and the rotor during the start/stop, zero load capacity during startup and shutdown, and the thermal runaway are known as the major challenges for AFB. Hybrid air foil bearings (HAFBs) were suggested as a prominent solution for overcoming those limitations of AFBs [47-51]. HAFBs utilize injection of externally pressurized air into the bearing's radial clearance. Figure 1-2 presents examples of HAFBs manufactured at the Turbomachinery and Energy Systems Laboratory at the University of Texas at Arlington.

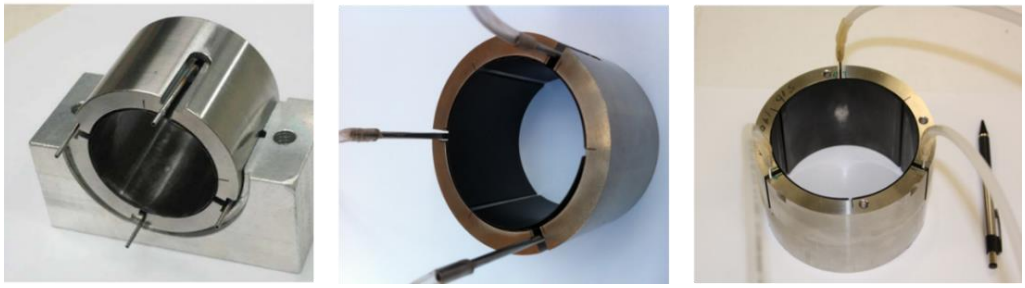

Figure 1-2 Hybrid air foil bearing [52]

The injection of externally pressurized air is widely used in rigid wall hydrostatic gas bearings. Numerous studies on the rigid wall hydrostatic gas bearings are available in the literature [53-55], however, lack of a damping mechanism and lower stability are the challenges for the rigid wall hydrostatic gas bearings.

The concept of hybrid air foil bearing is first introduced by Kim and Park [47] with radial injection of pressurized air into the bearing clearance through orifice tubes attached to the top foil. In their proposed HAFB, a flexible steel tube was welded to the back side of the top foil where the orifice holes were drilled. An external compressor pressurized the air and the externally pressurized air was directly supplied to the bearing clearance to lift off the rotor when the rotor is stationary. Figure 1-3 illustrates the cross-section view of a three-pad HAFB.

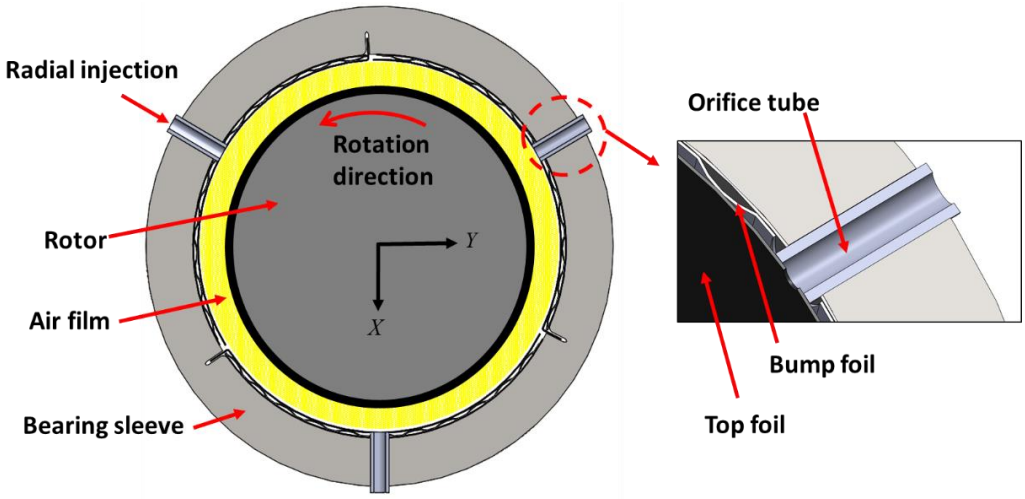

Figure 1-3 Cross-section view of a three-pad HAFB

Several studies show that the radial injection of externally pressurized air into HAFB clearance improves the bearing load carrying capacity and eliminates the initial friction and wear between rotor and HAFB. Kim and Park [47] measured the load capacity of a prototype HAFB with four orifices attached to the top foil. The HAFB load carrying capacity was measured experimentally at 20,000 rpm, and the top foil temperature at the loaded region was used to indicate the load capacity limit. A significant reduction in temperature and higher load carrying capacity compare to the previously published data for a similar hydrodynamic AFB was reported. Moreover, they measured and compared the start/stop friction torque of a HAFB and a hydrodynamic AFB. In hydrodynamic operation, dry sliding contact between the rotor and the top foil during start/stop produces a large friction torque, and the friction torque reduces immediately after the rotor is fully lifted-off. For hybrid operation, the friction between the rotor and the top foil during start/stop is negligible since the rotor is fully lifted-off even during start/stop. For both hydrodynamic and hybrid operations, the friction torque after

rotor's lift-off is equal to air frictional torque. Figure 1-4) shows a comparison between friction torque of HAFB and AFB [47].

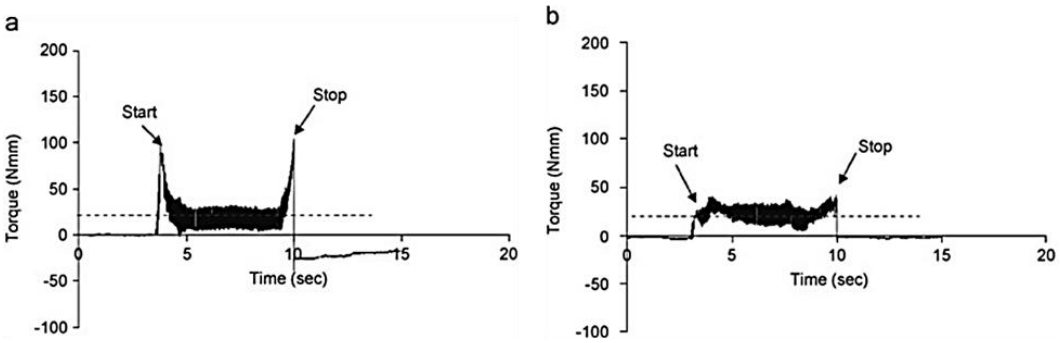

Figure 1-4 Friction torque during rotor speedup to 6,500rpm and shutdown (a) hydrodynamic operation and (b) hybrid operation ([47])

Kumar and Kim [56] studied the load carrying capacity of a second generation HAFB. Experimental studies on the load carrying capacity at low speed (10,000rpm) showed a better performance for the HAFB compared to the hydrodynamic AFB. However, at high speeds, enhancement in the HAFB load carrying capacity is not significant. Kim and Zimbru [48] investigated the thermal behavior of a large HAFB (101.6 mm) under various supply pressures, external loads, and operating speeds. Comparison of the measured data for the HAFB to the previously published data for a hydrodynamic AFB [1] showed that the HAFB friction torque under moderate loads is much lower than the hydrodynamic AFB. Thermal transient measurements at different speeds showed that the temperature of the bearing compartment increases with operating speed. The authors conducted an endurance test to evaluate the lifetime and reliability of the HAFB. In the endurance test, the HAFB successfully operated for 1000 cycles (start/stop) under external load of 365 N and supply pressure of 4.48 bar.

Kumar and Kim [49] presented a computational model to predict the stiffness and damping coefficients of HAFBs. They calculated force coefficients for a single-pad HAFB

using a linear perturbation method. A much smaller cross-coupled stiffness for the HAFB compare to the hydrodynamic AFB is reported. The authors reported that the HAFB's stiffness and damping coefficients are a function of the orifice size and supply pressure, i.e., the direct and cross-coupled stiffness decrease with either supply pressure or feed parameter while the direct and cross-coupled damping increases with either supply pressure or feed parameter. Wang and Kim [50] conducted experimental investigation on the force coefficients of a large HAFB. Static force coefficients were measured by the load-deflection tests. Dynamic force coefficients were measured by applying an impulse excitation force to the bearing sleeve using an impact hammer and measuring the response vibration using two eddy current type proximity probes while the rotor was spinning. The authors claimed that the HAFB's hydrostatic injection results in a higher static stiffness coefficient compared to the pure hydrodynamic AFB. Also, the HAFB's static stiffness coefficient increases with rotor speed, static load, and the hydrostatic pressure. The measured dynamic stiffness coefficients from impulse response tests showed that the HAFB's dynamic stiffness increases with speed and load. The stiffness and damping coefficients for the large HAFB at 18,000 rpm were measured to be around 6 MN/m and 2 kN-s/m, respectively. Kim and Varrey [57] demonstrated the usefulness of the radial air injection on the stability of a rigid rotor supported by HAFBs. Rotordynamic stability of rotor-HAFB system was evaluated both experimentally and numerically using a three-pad HAFB. Rotor imbalance response was measured for different supply pressures with in-phase imbalance masses. It was reported that as the supply pressure increases the bearing becomes more stable, allowing higher operating speeds.

Utilization of controlled hydrostatic injection in the radial direction was reported as a beneficial method to increase the rotordynamic stability. Numerous studies on active and semi-active lubrication of rigid wall gas bearings are available in the literature.

Horikawa et al. [58] proposed the first gas journal bearing with the active lubrication mechanism in which the shaft was supported by a bearing with four pads controlled by non-contact actuators. The active lubrication mechanism was realized by measuring the radial position of the shaft using non-contact sensors, and regulating the actuators based on the sensors signal. The results showed that the stiffness is improved and the damping is increased by using the active control. However, the bandwidth for the position sensor on the shaft is a limiting factor. Mizumoto et al. [59] presented a hydrostatic air bearing with active inherent restrictor to control the pressure in the bearing film. The authors reported that the dynamic performance of the rotor-bearing system was improved by using the active hydrostatic air bearing. They also claimed that the pneumatic hammer did not occur by implementing the active inherent restrictor. However, the limitation in the bandwidth and the excessive cost of the control system are the major drawbacks of the active control system. San Andres and Ryu [60] evaluated the rotordynamic performance of a hybrid flexure pivot tilting pad air bearing with various supply pressures. Tests showed that the amplitude of the rotor synchronous response while passing the critical speed can be reduced by controlling the supply pressure. Pierart and Santos [61] evaluated the dynamic characteristics of a rotor-air bearing system with adjustable external pressurization. The active hydrostatic gas bearing had four adjustable injectors controlled by piezoactuators. It was shown that the injector position and the amount of mass flow rate through the injector have a direct effect on the dynamic characteristics of the rotor-bearing system. They claimed that the damping coefficient of the active air journal bearing was increased significantly.

1. 6. Problem statement and motivation

Although extensive studies have been conducted on the controlled pressurization of the rigid wall air/gas journal bearings, there is no work reported on the active or semi-

active lubrication of the AFBs. So far, the hydrostatic injection adopted in the HAFBs was for improvement of the load capacity at low speeds and reduction of friction torque during start/stop, and effective thermal management. However, controlled hydrostatic injection in HAFB can be also utilized to improve the dynamic characteristics of the HAFB. Even if damping of AFB is higher than that of rigid-walled air/gas bearings, cross-coupled stiffness still exists. Important parameters related to the cross-coupled stiffness are the attitude angle and rotor eccentricity. In general, the large attitude angle along with small eccentricity results in a large cross-coupled stiffness. The controlled injection of the pressurized air can be used to control the rotor position inside the bearing in order to achieve small attitude angle and large eccentricity.

The circumferential location of the hydrostatic injection is another important parameter which has a significant effect on the HAFBs performance. The circumferential position of hydrostatic injections in HAFBs can be optimized based on the rotor attitude angle and eccentricity to further improve the dynamic characteristics and stability of HAFBs.

In this dissertation, controlled radial injection of the pressurized air is used as an external force on the rotor to improve the stability of the rotor-HAFB system. Moreover, the effect of the circumferential location of hydrostatic injection on rotordynamic performance of HAFB is investigated through rotordynamic measurements and numerical predictions. Both experimental works and numerical simulations are presented.

Chapter 2

NUMERICAL MODELING

2. 1. Orbit simulation

Numerical analyses and predictions presented in this dissertation consist of orbit simulation to predict rotor imbalance responses, and perturbation analyses to predict the force coefficients of the HAFBs. For orbit simulation, transient motion of the rotor is predicted by numerical time integration of rotor equation of motion. Reaction forces and moments from bearings are predicted by solving the transient Reynolds equation and finding the pressure distribution inside the bearing film. Numerical analyses are performed in isothermal condition, and air is considered to be isoviscous ideal gas. The other assumptions are, (1) two bearings are concentric, and (2) entire rotor is a rigid body with four degrees of freedom (4 DOF) motions. Similar approach using 4 DOF rigid rotor model was used in the other previous studies [46, 51, 62].

Rotor 4 DOF motions are translation motions along the x and y directions, and rotational motions about x and y axes (represented by ξ and ψ respectively). Figure 2-1 depicts the rotor-bearing system configuration and the global coordinate system. The equations of 4DOF motion of the rotor is expressed as:

$$\begin{aligned} m_R\ddot{x} &= F_{brg\_X} + F_{imb\_X} + m_R g \\ m_R\ddot{y} &= F_{brg\_Y} + F_{imb\_Y} \\ I_T\ddot{\xi} + I_P\omega\dot{\psi} &= M_{brg\_\xi} + M_{imb\_\xi} \\ I_T\ddot{\psi} + I_P\omega\dot{\xi} &= M_{brg\_\psi} + M_{imb\_\psi} \end{aligned} \tag{2-1}$$

, where m_R is the rotor mass, I_T and I_P are the rotor polar and transverse moments of inertia. $F_{brg\_X/Y}$ and $F_{imb\_X/Y}$ are the bearing reaction forces and the imbalance forces, and $M_{brg\_\xi/\psi}$ and $M_{imb\_\xi/\psi}$ are the moments from the bearing reaction forces and moment from imbalance forces, respectively.

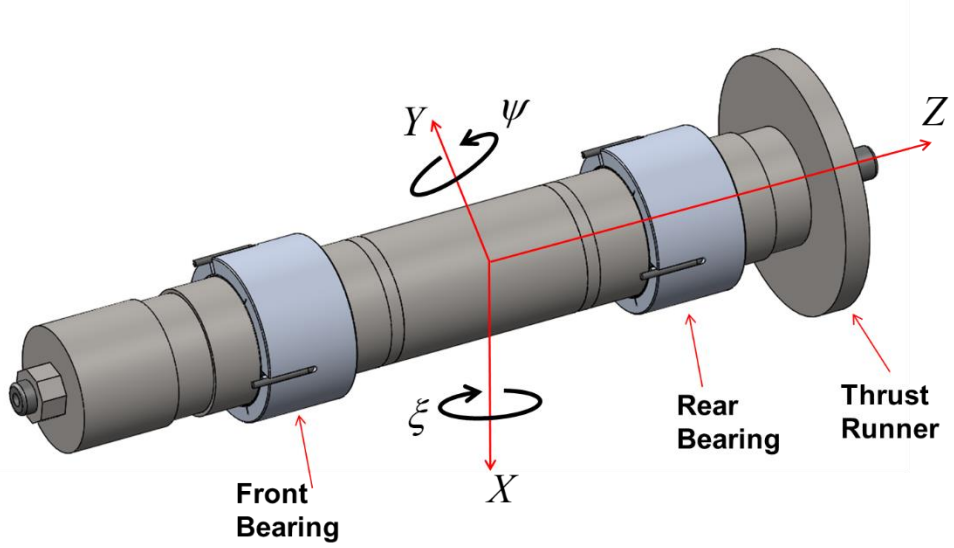

Figure 2-1 Rotor-HAFB configuration and the coordinate system

The imbalance forces and imbalance moments on the rotor are given as:

$$F_{imb\_X}\hat{i} + F_{imb\_Y}\hat{j} = \omega^2 \sum_{i=1,2}\left[m_R u_i \cos\left(\omega t + \phi_i\right)\hat{i} + m_R u_i \sin\left(\omega t + \phi_i\right)\hat{j}\right] \quad (2\text{-}2)$$

$$M_{imb\_Y}\hat{i} + M_{imb\_X}\hat{j} = \sum_{i=1,2} l_i \hat{k} \times \left(F_{imb\_X}\hat{i} + F_{imb\_Y}\hat{j}\right) \quad (2\text{-}3)$$

, where $\hat{i}$, $\hat{j}$ and $\hat{k}$ are unit vectors corresponding to radial (x, y) and axial (z) directions respectively. u_i is the imbalance radius, and l_i is the axial coordinate of the

imbalance masses from the rotor mass center of gravity. The bearing reaction forces, and the moments due to the bearing reaction forces are expressed as following:

$$F_{brg\_X}\hat{\imath} + F_{brg\_Y}\hat{\jmath} = \sum_{j=1,2} p_j \iint \left(cos\theta_{\hat{\imath}} + sin\theta_{\hat{\jmath}}\right) R d\theta dz_i \tag{2-4}$$

$$M_{brg\_\xi}\hat{\imath} + M_{brg\_\psi}\hat{\jmath} = \sum_{i=1,2} (Z_j K \times p_j \iint \left(cos\theta_{\hat{\imath}} + sin\theta_{\hat{\jmath}}\right) R d\theta dz_i \tag{2-5}$$

, where Z is the axial location of bearing's center from the rotor's mass center of gravity. R is the bearing journal radius. Pressure profile over the bearing surface (p) is calculated by solving the transient Reynolds equation for the HAFB (Eq.(2-6)). Details and procedure for derivation of Reynolds equation for HAFB is available in [54, 55]

$$\frac{\partial}{\partial x}\left(-\frac{ph^3}{12\mu}\frac{\partial p}{\partial x} + \frac{R\omega}{2}ph\right)_j + \frac{\partial}{\partial z}\left(-\frac{ph^3}{12\mu}\frac{\partial p}{\partial z}\right)_j + \frac{\partial}{\partial t}\left(ph\right)_j = \frac{R_g T \dot{m}_s}{\left(\Delta x \Delta z\right)_{brg}} \tag{2-6}$$

, where x represents the bearing's local coordinate along circumferential direction, and z represents the bearing's local coordinate along the axial direction. Figure 2-2 depicts the relation between the global axial coordinate (Z_j), and bearing's local axial coordinate (z_j). R is the radius of bearing journal. ω is the angular velocity of the rotor. μ is the air viscosity , and R_g is the gas constant for the air . T is the temperature of the supplied air ($T = 293K$), and $\dot{m}_s$ is the air mass flow rate through the orifice tube and it is calculated from isentropic flow model through the orifice following [49].

$$\dot{m}_s = \frac{p_s}{\sqrt{R_g T_s}} C_d A_O \left[2\gamma_g \frac{k}{k-1} \left(\left(\frac{p}{p_s} \right)^{\frac{2}{k}} - \left(\frac{p}{p_s} \right)^{\frac{(k-1)}{k}} \right) \right]^{\frac{1}{2}}, \left(\frac{p}{p_s} \right) < \left(\frac{2}{k+1} \right)^{\frac{k}{(k-1)}} \quad \text{(2-7)}$$

$$\dot{m}_s = \frac{p_s}{\sqrt{R_g T_s}} C_d A_O \left(2\gamma_g \frac{k}{k-1} \right)^{\frac{1}{2}} \left(\frac{k}{k-1} \right)^{\frac{1}{(k-1)}}, \left(\frac{p}{p_s} \right) > \left(\frac{2}{k+1} \right)^{\frac{k}{(k-1)}} \quad \text{(2-8)}$$

Equations (2-7) and (2-8) correspond to the unchoked and choked conditions, respectively. $A_O = \pi d_O h$ is an effective orifice area, d_O is the orifice diameter, p_s is the supply pressure into the orifice, and C_d is a discharge coefficient of orifice which is an empirical number. k is the ratio of specific heat ($k = c_p / c_v$). For the numerical modeling, the Reynolds equation (Eq.(2-6)) is used in a non-dimensional format using $\theta = x/R$, $Z = z/R$, $p = p/p_a$, $H = h/C$, and $\nu = \omega_s/\omega$. The non-dimensional Reynolds equation is expressed as:

$$\frac{\partial}{\partial\theta}(PH^3\frac{\partial P}{\partial\theta}) + \frac{\partial}{\partial Z}(PH^3\frac{\partial P}{\partial Z}) = \Lambda\frac{\partial}{\partial\theta}(PH) + 2\Lambda\nu\frac{\partial}{\partial\tau}(PH) - \frac{12\mu R^2}{{p_a}^2 C^3}\frac{R_g T\dot{m}_s}{A} \quad \text{(2-9)}$$

, where the bearing number is defined as: ($\Lambda = 6\mu\omega/\, p_a(R/C)^2$)

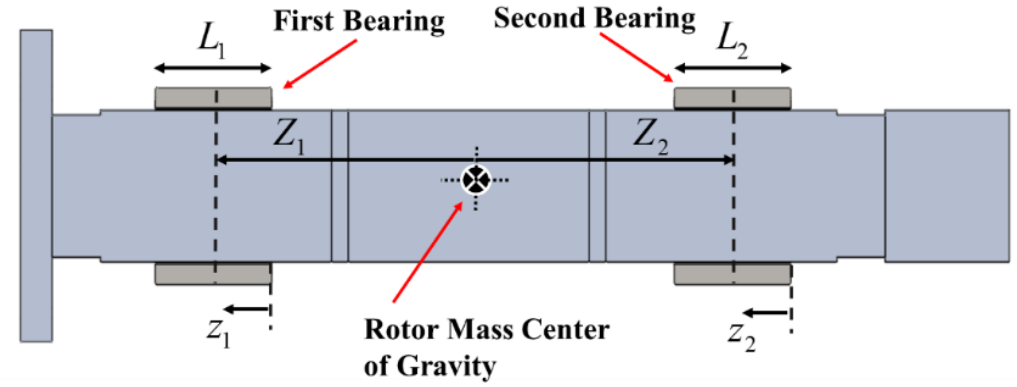

Figure 2-2 Rotor-bearing axial coordinate configuration

HAFB film thickness (h) is expressed as the following:

$$h_j\left(\theta, z_j\right) = C + \left(x + \psi Z_j\right)\cos\theta + \left(y - \xi Z_j\right)\sin\theta + w_j\left(\theta, z_j\right) - r_p\cos\left(\theta - \theta_{pad}\right) \quad (2\text{-}10)$$

, where C is the bearing radial clearance, X and Y are the displacement of the rotor's center (found from rotor's equation of motion), and $w_j(\theta, z_j)$ is the equation of the elastic deflection for the underlying support structure (top foil and bump foil), which is a function of the pressure force, material property, and geometries of the support structure [47]. r_p is a hydrodynamic preload of each top foil pad. The hydrodynamic preload is the difference between the nominal clearance (C) and the minimum clearance (C_m), i.e. $r_p = C - C_m$, as illustrated in Figure 2-3. The angular width of each top foil pad is expressed by θ_{pad}, and the location of the minimum clearance of each pad (set bore clearance) is shown by θ_{SB} as depicted in Figure 2-4. Because of the hydrodynamic

preload, bearing film thickness converges from the leading edge until θ_{SB}, and diverge again after θ_{SB}. The ratio of pad angle and set bore angle is defined as offset ratio (γ)

$$\gamma = \frac{\theta_{SB}}{\theta_{pad}} \tag{2-11}$$

The amount of hydrodynamic preload (r_p) and offset ratio (γ) are design parameters of the AFB, and they are determined based on the performance requirement of the rotor-bearing.

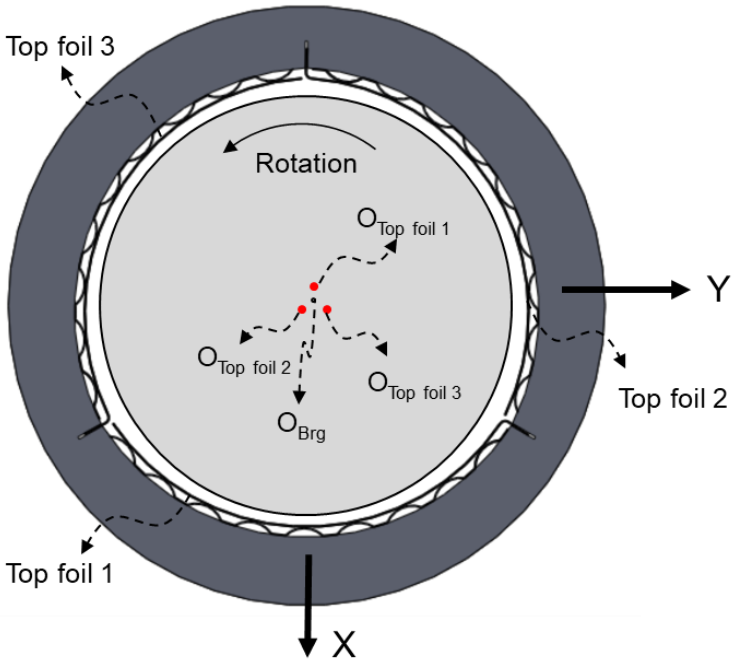

Figure 2-3 Schematic of a pre-loaded three-pad AFB

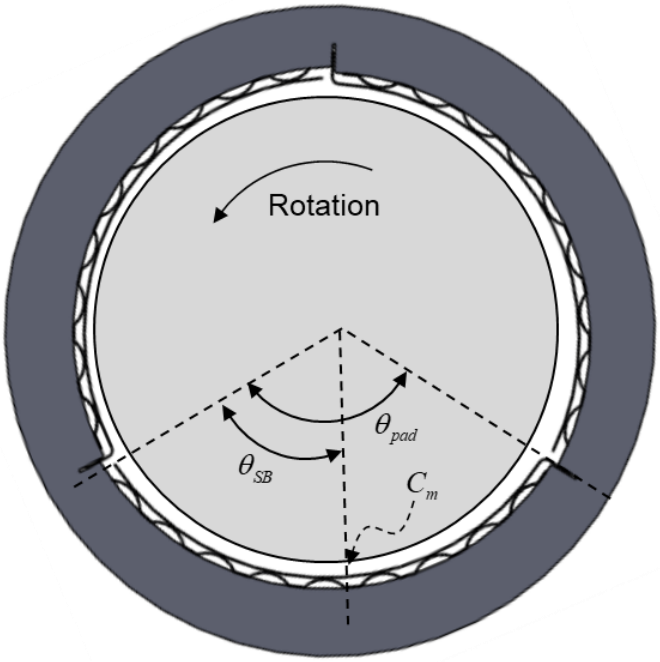

Figure 2-4 Definition of pad angle and offset angle

2. 2. Perturbation formulation

Frequency-domain perturbation analyses are used to identify the HAFBs force coefficients, and to predict natural frequencies of the rotor-HAFB system. The details of the perturbation method for HAFB that presented in this section are a summary of the work presented by Kumar [63] and Kumar and Kim [49]. The frequency dependent stiffness and damping coefficients of the bearing are predicted for a small excitation of rotor center (Δe_X , Δe_Y), with the frequency of ω_s with respect to the static equilibrium position (e_{X0}, e_{Y0}). Therefore, the perturbed rotor eccentricity is expressed as

$$\begin{aligned} e_X &= e_{X0} + \Delta e_X e^{i\omega_s t} \\ e_Y &= e_{Y0} + \Delta e_Y e^{i\omega_s t} \end{aligned} \tag{2-12}$$

Perturbed bump deflection and perturbed film thickness for the above rotor perturbation are given as:

$$u = u_0 + \Delta u_X e^{i\omega_s t} + \Delta u_Y e^{i\omega_s t} \tag{2-13}$$

$$h = h_0 + \Delta h_X e^{i\omega_s t} + \Delta h_Y e^{i\omega_s t} \tag{2-14}$$

, where $h_0 = C + e_{X0}\cos\theta + e_{Y0}\sin\theta + u_o$, and $\Delta h_X = \Delta e_X \cos\theta + \Delta u_X$, and $\Delta h_Y = \Delta e_Y \sin\theta + \Delta u_Y$. $\Delta u_{X/Y}$ is a bump deflection due to rotor perturbation ($\Delta e_{X/Y}$). Because of film thickness perturbation, the perturbed pressure is expressed be Eq.(2-15) , where P_X and P_Y are complex numbers with real and imaginary parts.

$$p = p_0 + \Delta e_X p_X e^{i\omega_s t} + \Delta e_Y p_Y e^{i\omega_s t} \tag{2-15}$$

The bump foil structure is assumed as independent elastic foundation support (spring-damper); therefore, equation of motion of the bump foil structure is given by:

$$f_{bump} = K_{bump} u + C_{bump} \frac{du}{dt} \tag{2-16}$$

, where $f_{bump} = pA_{bump}$ is the pressure force acting on a bump, A_{bump} is the effective area that the bump covers. K_{bump} is the bump stiffness, C_{bump} is the equivalent viscous damping coefficient of the bump (independent spring-damper model), and u is the bump deflection. Assuming sinusoidal motion for the bump foil, the equivalent viscous damping coefficient of the bump foil can be calculated from the structural loss model:

$$C_{bump} = \frac{\eta K_{bump}}{\omega_s} \tag{2-17}$$

, where η is an empirical parameter for the structural loss factor of each independent spring-damper, and ω_s is the excitation frequency of an independent spring-damper. Inserting Eq. (2-17) into Eq. (2-16), we have

$$pA_{bump} = K_{bump}u + \eta \frac{K_{bump}}{\omega_s}\frac{du}{dt} \tag{2-18}$$

Inserting Eq. (2-14) and Eq. (2-15) into Eq. (2-6), and following procedure described in [63], yields the first order Reynolds equations for the perturbed pressure, where $\Gamma_s = 12\mu C_d A_o \sqrt{R_g T} \Big/ p_a C^3$ is a feed parameter:

$$\begin{aligned}
&\frac{\partial}{\partial\theta}\left[P_0 {H_0}^3 \frac{\partial P_X}{\partial\theta}\right] + \frac{\partial}{\partial\theta}\left[\left(3{H_0}^2 P_0\left(\frac{P_X}{K_{bumo}+C_{bump}\nu i}+\cos\theta\right)+{H_0}^3 P_X\right)\frac{\partial P_0}{\partial\theta}\right] \\
&+\frac{\partial}{\partial Z}\left[-P_0 {H_0}^3 \frac{\partial P_X}{\partial Z}\right] + \frac{\partial}{\partial Z}\left[\left(3{H_0}^2 P_0\left(\frac{P_X}{K_{bump}+C_{bump}\nu i}+\cos\theta\right)+{H_0}^3 P_X\right)\frac{\partial P_0}{\partial Z}\right] \\
&= 2\Lambda\nu i\left(P_0\left(\frac{P_X}{K_{bump}+C_{bump}\nu i}+\cos\theta\right)+P_X H_0\right)+\Lambda\frac{\partial}{\partial\theta}\left[P_0\left(\frac{P_X}{K_{bump}+C_{bump}\nu i}+\cos\theta\right)+\left(P_X \Lambda H_0\right)\right] \\
&-\left(\frac{2k}{k-1}\right)^{\frac{1}{2}}\frac{\Gamma_s P_s}{\Delta Z\Delta\theta}\left[\left.\frac{\partial f(P,H)}{\partial P}\right|_{P_0,H_0} P_X + \left.\frac{\partial f(P,H)}{\partial H}\right|_{P_0,H_0}\left(\frac{P_X}{K_{bump}+C_{bump}\nu i}+\cos\theta\right)\right]
\end{aligned} \tag{2-19}$$

$$\frac{\partial}{\partial\theta}\left[P_0{H_0}^3\frac{\partial P_Y}{\partial\theta}\right]+\frac{\partial}{\partial\theta}\left[\left(3{H_0}^2P_0\left(\frac{P_Y}{K_{bump}+C_{bump}\nu i}+\sin\theta\right)+{H_0}^3P_Y\right)\frac{\partial P_0}{\partial\theta}\right]$$
$$+\frac{\partial}{\partial Z}\left[-P_0{H_0}^3\frac{\partial P_Y}{\partial Z}\right]+\frac{\partial}{\partial Z}\left[\left(3{H_0}^2P_0\left(\frac{P_Y}{K_{bump}+C_{bump}\nu i}+\sin\theta\right)+{H_0}^3P_Y\right)\frac{\partial P_0}{\partial Z}\right]$$
$$=2\Lambda\nu i\left(P_0\left(\frac{P_Y}{K_{bump}+C_{bump}\nu i}+\sin\theta\right)+P_YH_0\right)+\Lambda\frac{\partial}{\partial\theta}\left[P_0\left(\frac{P_Y}{K_{bump}+C_{bump}\nu i}+\sin\theta\right)+\left(P_Y\Lambda H_0\right)\right] \quad (2\text{-}20)$$
$$-\left(\frac{2k}{k-1}\right)^{\frac{1}{2}}\frac{\Gamma_sP_s}{\Delta Z\Delta\theta}\left[\left.\frac{\partial f(P,H)}{\partial P}\right|_{P_0,H_0}P_X+\left.\frac{\partial f(P,H)}{\partial H}\right|_{P_0,H_0}\left(\frac{P_Y}{K_{bump}+C_{bump}\nu i}+\sin\theta\right)\right]$$

$f(H_0,P_0)$ and its derivatives for choked and unchoked conditions are given by:

Choked:

$$f(H_0,P_0)=H_0$$
$$\left.\frac{\partial f(H,P)}{\partial P}\right|_{H_0,P_0}=0 \quad (2\text{-}21)$$
$$\left.\frac{\partial f(H,P)}{\partial H}\right|_{H_0,P_0}=1$$

Unchoked:

$$f(H_0,P_0)=H_0\left(\left(\frac{P_0}{P_s}\right)^{\frac{2}{k}}-\left(\frac{P_0}{P_s}\right)^{\frac{(k+1)}{k}}\right)^{\frac{1}{2}}$$
$$\left.\frac{\partial f(H,P)}{\partial P}\right|_{H_0,P_0}=H_0\frac{1}{2}\left(\left(\frac{P_0}{P_s}\right)^{\frac{2}{k}}-\left(\frac{P_0}{P_s}\right)^{\frac{k+1}{k}}\right)^{\frac{-1}{2}}\left(\frac{2}{k}\left(\frac{1}{P_s}\right)^{\frac{2}{k}}P_0^{\left(\frac{2}{k}-1\right)}-\frac{k+1}{k}\left(\frac{1}{P_s}\right)^{\frac{k+1}{k}}P_0^{\frac{1}{k}}\right) \quad (2\text{-}22)$$
$$\left.\frac{\partial f(P,H)}{\partial H}\right|_{H_0,P_0}=\left(\left(\frac{P_0}{P_s}\right)^{\frac{2}{k}}-\left(\frac{P_0}{P_s}\right)^{\frac{k+1}{k}}\right)^{\frac{1}{2}}$$

Once the perturbed pressure profile is found (P_X, P_Y), the frequency dependent stiffness and damping coefficients are calculated from the following equations:

$$\begin{bmatrix} K_{XX} & K_{XY} \\ K_{YX} & K_{YY} \end{bmatrix} = \frac{W_0}{C}\frac{R}{2L}\int\int \begin{bmatrix} \mathrm{Re}(P_X)\cos\theta & \mathrm{Re}(P_Y)\cos\theta \\ \mathrm{Re}(P_X)\sin\theta & \mathrm{Re}(P_Y)\sin\theta \end{bmatrix}$$

$$\begin{bmatrix} C_{XX} & C_{XY} \\ C_{YX} & C_{YY} \end{bmatrix} = \frac{W_0}{C\omega_s}\frac{R}{2L}\int\int \begin{bmatrix} \mathrm{Im}(P_X)\cos\theta & \mathrm{Im}(P_Y)\cos\theta \\ \mathrm{Im}(P_X)\sin\theta & \mathrm{Im}(P_Y)\sin\theta \end{bmatrix} \quad (2\text{-}23)$$

, where $W_0 = 2p_aRL$. (K_{XX}, K_{YY}) and (C_{XX}, C_{YY}) are frequency dependent direct stiffness and direct damping coefficients. (K_{XY}, K_{YX}) and (C_{XY}, C_{YX}) are cross-coupled stiffness and cross-coupled damping coefficients. Figure 2-4 illustrates the physical representation of direct and cross-coupled stiffness and damping coefficients.

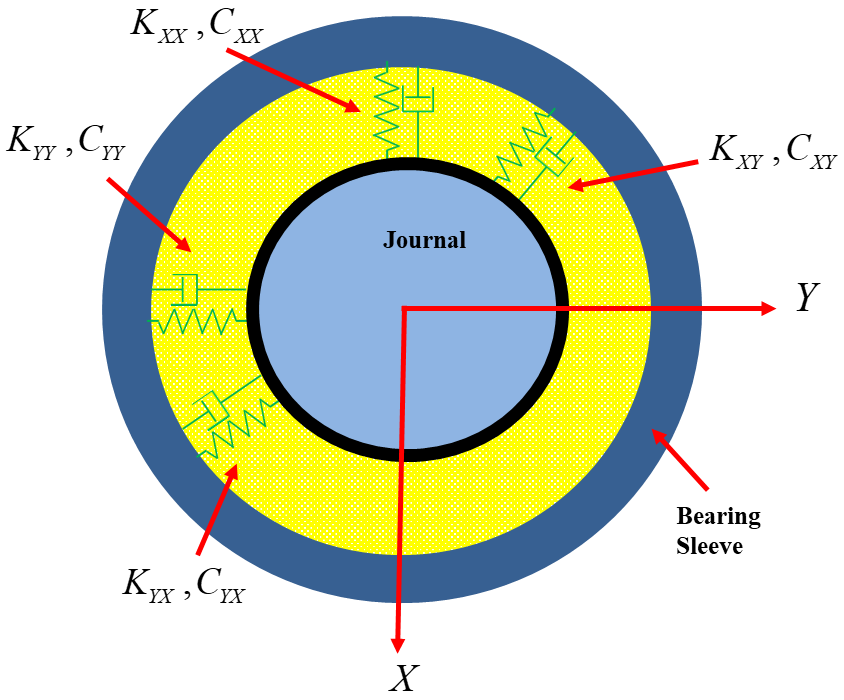

Figure 2-5 Physical representation of HAFB force coefficients

2. 3. Modal analysis

Modal analysis is an important tool for rotordynamic stability analysis. Modal analysis provides deeper insight into rotordynamic stability and rotor critical speeds. In this section, the mathematical formulation for modal analysis and the procedure to calculate HAFBs modal impedances are described.

The rotor-bearing system can be modeled as a spring-damper-mass system, which is illustrated in Figure 2-5. The equation of motion for the rotor following the rotor-bearing configuration presents in Figure 2-5 can be expressed as:

$$\begin{aligned} m_R\ddot{x}_R + K_{XX}x_R + K_{XY}y_R + C_{XX}\dot{x}_R + C_{XY}\dot{y}_R = 0 \\ m_R\ddot{y}_R + K_{YX}x_R + K_{YY}y_R + C_{YX}\dot{x}_R + C_{YY}\dot{y}_R = 0 \end{aligned} \tag{2-24}$$

, where x_R and y_R are small displacements of rotor center around its static equilibrium position and along x and y directions. The static equilibrium of the rotor's center is found by balancing the bearing reaction forces with the external forces on the rotor (the imbalance forces are assumed to be zero). Assuming an oscillating motion for the rotor with the frequency of ω_s around its equilibrium position ($x_R(t) = \delta x_R\, e^{i\omega_s t}$, $y_R(t) = \delta y_R\, e^{i\omega_s t}$), rotor equations of motion can be written as:

$$\begin{aligned} &m_R(-\delta x_R \omega_s^2\, e^{i\omega_s t}) + K_{XX}(\delta x_R\, e^{i\omega_s t}) + K_{XY}(\delta y_R\, e^{i\omega_s t}) \\ &\qquad + C_{XX}(\delta x_R i\omega_s\, e^{i\omega_s t}) + C_{XY}(\delta y_R i\omega_s\, e^{i\omega_s t}) = 0 \\ &m_R(-\delta y_R \omega_s^2\, e^{i\omega_s t}) + K_{YX}(\delta x_R\, e^{i\omega_s t}) + K_{YY}(\delta y_R\, e^{i\omega_s t}) \\ &\qquad + C_{YX}(\delta x_R i\omega_s\, e^{i\omega_s t}) + C_{YY}(\delta y_R i\omega_s\, e^{i\omega_s t}) = 0 \end{aligned} \tag{2-25}$$

Bearing impedances ($Z_{\alpha\beta}$) are expresses as;

$$\begin{aligned} Z_{XX} &= K_{XX} + iC_{XX}\omega_s \\ Z_{YX} &= K_{YX} + iC_{YX}\omega_s \\ Z_{XY} &= K_{XY} + iC_{XY}\omega_s \\ Z_{YY} &= K_{YY} + iC_{YY}\omega_s \end{aligned} \tag{2-26}$$

Considering $s = i\omega_s$, Eq. (2-24) can be written in the following form

$$\begin{bmatrix} m_R s^2 & 0 \\ 0 & m_R s^2 \end{bmatrix} \begin{Bmatrix} \delta x_R \\ \delta y_R \end{Bmatrix} + \begin{bmatrix} Z_{XX} & Z_{XY} \\ Z_{YX} & Z_{YY} \end{bmatrix} \begin{Bmatrix} \delta x_R \\ \delta y_R \end{Bmatrix} = 0 \tag{2-27}$$

Modal impedances are defined as ($Z_{K=1,2} = m_R s$) therefore Eq.(2-27) can be rearranged and written as:

$$\begin{bmatrix} Z_{XX} - Z_K & Z_{XY} \\ Z_{YX} & Z_{YY} - Z_K \end{bmatrix} \begin{Bmatrix} \delta x_R \\ \delta y_R \end{Bmatrix} = 0 \tag{2-28}$$

Solutions of above equation for existing $\begin{Bmatrix} \delta x_R \\ \delta y_R \end{Bmatrix}$ can be found by putting the impedances matrix equal to zero

$$(Z_{XX} - Z_K)(Z_{YY} - Z_K) - Z_{XY} Z_{YX} = 0 \tag{2-29}$$

, therefore;

$$\begin{aligned} Z_{K=1} &= \frac{Z_{XX} + Z_{YY}}{2} + \sqrt{\left(\frac{Z_{XX} + Z_{YY}}{2}\right)^2 - \left(Z_{XX} Z_{YY} - Z_{XY} Z_{YX}\right)} \\ Z_{K=2} &= \frac{Z_{XX} + Z_{YY}}{2} - \sqrt{\left(\frac{Z_{XX} + Z_{YY}}{2}\right)^2 - \left(Z_{XX} Z_{YY} - Z_{XY} Z_{YX}\right)} \end{aligned} \tag{2-30}$$

, where Z_1 and Z_2 are the forward and backward modal impedances respectively. Since the modal impedances are complex numbers, the real part is modal stiffness and the imaginary part is modal damping.

Chapter 3

FOIL BEARING MANUFACTURING PROCESS AND HIGH-SPEED ROTORDYNAMIC TEST RIG DESCRIPTION

This chapter introduces the test foil bearings and the high-speed test-rig for experimental evaluation. Procedure of manufacturing the foil bearings and a detailed overview of material properties and dimensions of the test foil bearings are presented. The imbalance condition and the natural frequencies of the shaft are characterized. Also, the high-speed rotordynamic test rig facility and the instrumentation for rotordynamic test are described.

3. 1. Description of test foil bearings

Figure 3-1 shows the three-pad HAFB. The three-pad HAFB consists of three top foils, and each top foil has a Stainless Steel orifice tube which is laser welded on the back side of the top foil. Figure 3-2 shows a top foil for the three-pad HAFB with welded orifice tube.

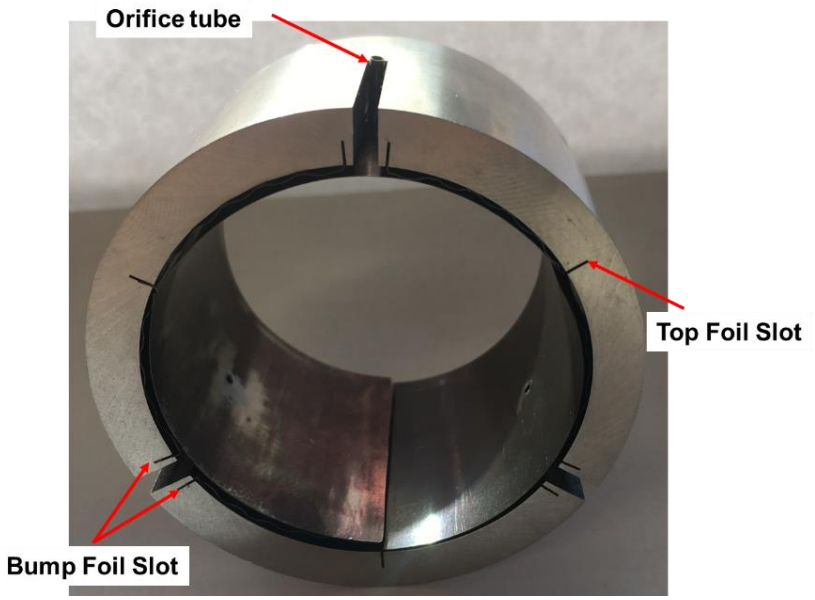

Figure 3-1 Three pad HAFB

The top foils are made from Inconel 750 material with 0.127 mm thickness. The manufacturing process of the top foil starts by cutting the flat annealed Inconel 750 sheets into top foil blanks. To achieve the circular contour of top foil, the blanks are curved through cold forming process. The fixed edge (leading edge) of the top foil is bended using a specific tooling made for forming the top foil lip area. Top foil lip area is used for assembling the top foils into the bearing sleeve. After forming the top foil and the top foil's lip area, the annealed top foils are going through a heat treatment process (up to 750 degree C) in order to release the stresses generated during the forming process and to achieve the desirable hardening and elastic properties. After heat treatment process, the orifice holes (0.4 mm diameter) are drilled in to the top foil, and the orifice tubes are welded to the top foils using the laser-welding machine.

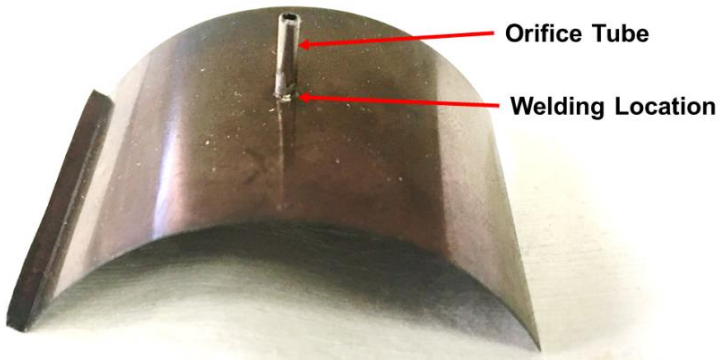

Figure 3-2 Top foil for three-pad HAFB with welded orifice tube

During the welding process of the orifice tubes, a slight bulge is created at the welding location due to the excessive heat generation from welding process and local thermal distortion around the orifice location. To remove the slight bulge, the inside of the top foils are grinded using a fine grinding wheel. Figure 3-3 shows the top foil holding tool

for grinding the welded location. Vacuum ports on the top foil holding tool are used to insure that the top foil is fixed inside the holding tool during the grinding process.

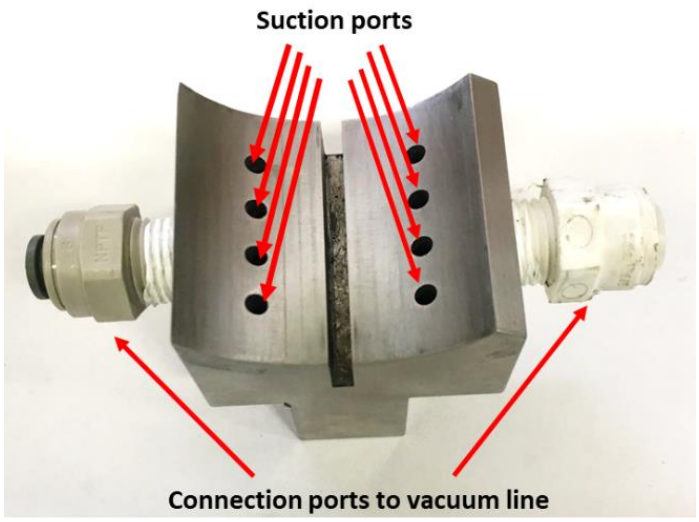

Figure 3-3 Top foil holding tool for grinding top foils

The three-pad HAFB (shown in Figure 3-1) has three bump foil stripes. Each bump foil stripe has 11 bumps. The bump foils are made from Inconel 750 material (0.127 mm thickness). Bump foils are formed using a high precision bump foil tooling (Figure 3-4). As shown in Figure 3-5, bump foil tooling consists of four components. During the forming process, bump foil blanks are fixed inside the foil holder, and up to 8 Tons pressure is applied to the top tooling, using a hydraulic press, to form the bumps. The bump foil tooling is capable of forming five bumps at each time. The complete 11 bumps for each bump foil stripe is formed by rotating the bottom tooling and forming 5 bumps at a time. The circular shape of the bottom tooling provides the required curvature for the bump foil stripes. The lip area formed by the foil holder is used for assembling the bump foils inside the bearing sleeve.

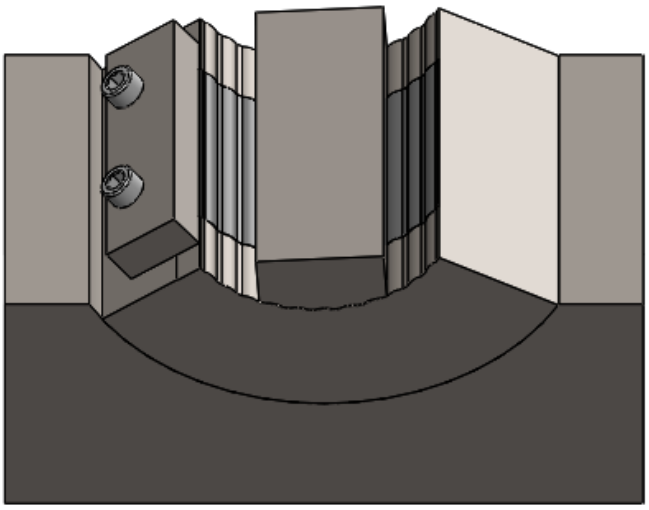

Figure 3-4 Schematic of the bump foil tooling

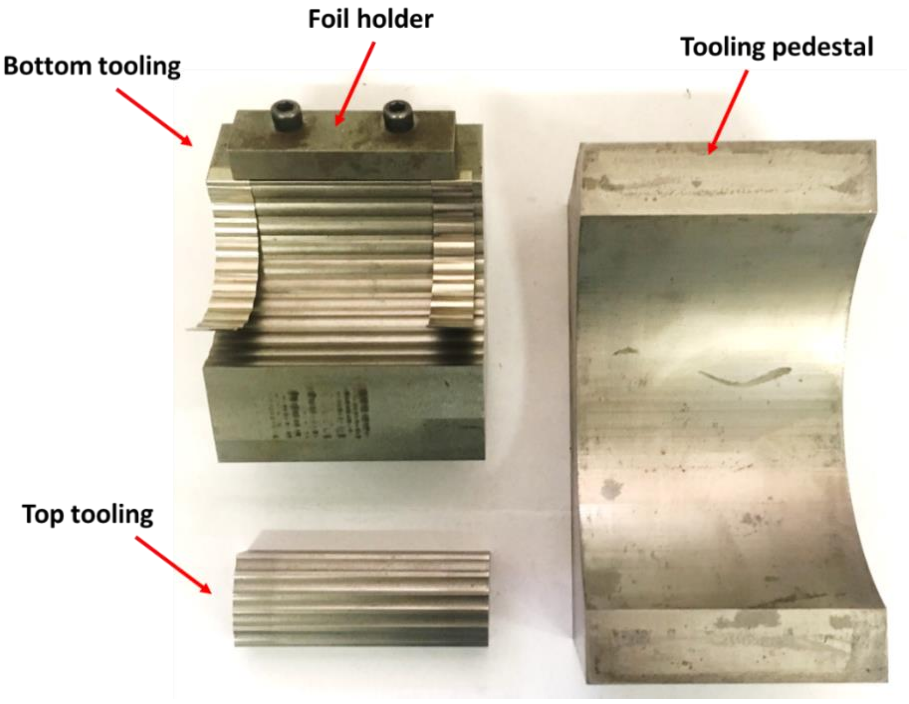

Figure 3-5 Bump foil tooling

Bump foil tooling is designed to create bump height of 0.506 mm (as illustrated in Figure 3-6). After the heat treatment of each bump foil stripe, the bump height of each individual bump is measured with a micrometer at four different axial location.

Table 1 presents of the bump height distribution of one bump foil stripe. The measured bump height is 0.506 +/- 0.002 mm, which is consistent with the original design value of the bump foil tooling .

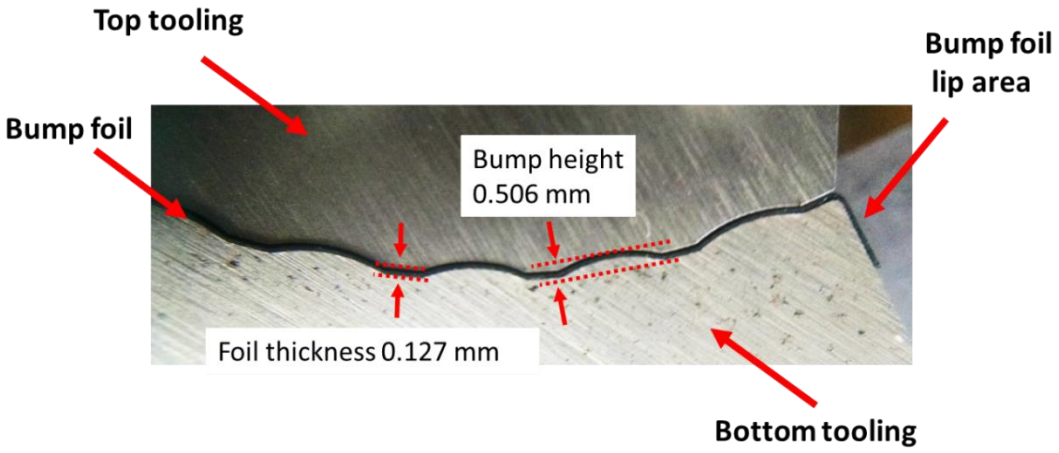

Figure 3-6 Bump foil inside the bump foil tooling

Table 1 Measured bump height values

Bump #	Bump height (mm)			
1	0.508	0.508	0.509	0.509
2	0.507	0.508	0.507	0.507
3	0.506	0.508	0.505	0.506
4	0.506	0.505	0.507	0.507
5	0.508	0.507	0.508	0.507
6	0.508	0.508	0.506	0.508

7	0.505	0.505	0.503	0.503
8	0.506	0.503	0.506	0.506
9	0.505	0.503	0.503	0.503
10	0.504	0.505	0.506	0.506
11	0.504	0.505	0.506	0.505

To confirm the performance of the foil bearing based on the initial design parameters, the static and dynamic characteristics of the foil bearing are evaluated. The static characteristic are evaluated by measuring the cold assembly radial clearance, and measuring the static stiffness coefficient and loss factor. These characteristics are evaluated by conducting load-deflection tests. The details and description of the load-deflection test is presented in Appendix A. for evaluation of dynamic performance, lift-off tests are conducted. In the lift-off test, the lift-off speed of the foil bearing is measured. Comparison between the measured lift-off speed and the calculated lift-off speed based on design parameters reveals whether the manufacturing process is performed properly or not. The details and procedure of lift-off test is described in Appendix B.

3. 2. Shaft characteristics and free-free natural frequencies

Figure 3-7 shows the front view and cross-section view of the shaft. The shaft is made from five different components. The center part is the rotor component. On both side of the rotor is a bearing journal. One end of the shaft is open (right hand side in Figure 3-7) and the other end has a thrust runner (left hand side in Figure 3-7). The imbalance masses are added to the shaft using six 2-56 UNC threaded holes available on both ends of the rotor (circle diameter of threaded holes is 38.1 mm). The balancing holes are circumferentially offset by 60 degree and they are symmetrical for both ends. The shaft's components are assembled using two tension bolts.

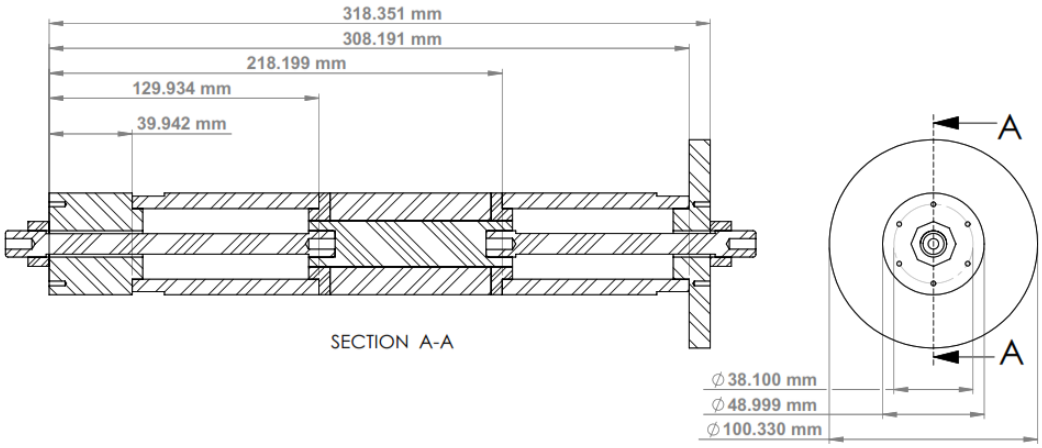

Figure 3-7 Cross-section view of the shaft

In order to have a rigid body shaft, bending mode natural frequency of the shaft should be above the shaft operating speed (the shaft is designed for maximum speed of 70,000 rpm). To find the appropriate tension force on the tension bolts that provides enough clamping force to have a rigid body shaft, the natural frequencies of the shaft for the case of a single rigid-body shaft is calculated from FEM model, and beam element model. Figure 3-8 shows the bending mode of a single rigid-body shaft from FEM model. The natural frequency of the bending mode is 1666.6 Hz (99,996 rpm).

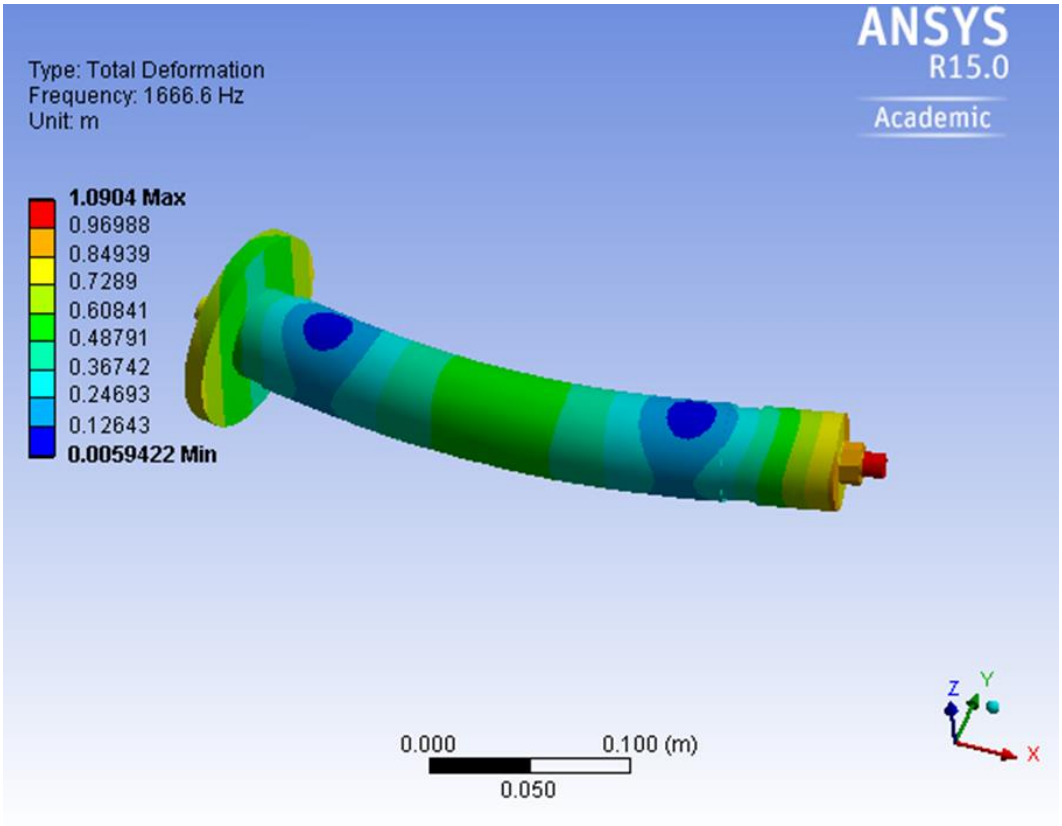

Figure 3-8 Shaft FEM analysis

Moreover, the XLRotor software is used to predict the free-free natural frequencies of the shaft. Figure 3-9 shows the shaft beam element model. From the free-free natural frequency map (Figure 3-9) it is observed that the shaft's bending mode natural frequency is around 97,000 rpm, which confirms the bending mode frequency predicted by FEM model.

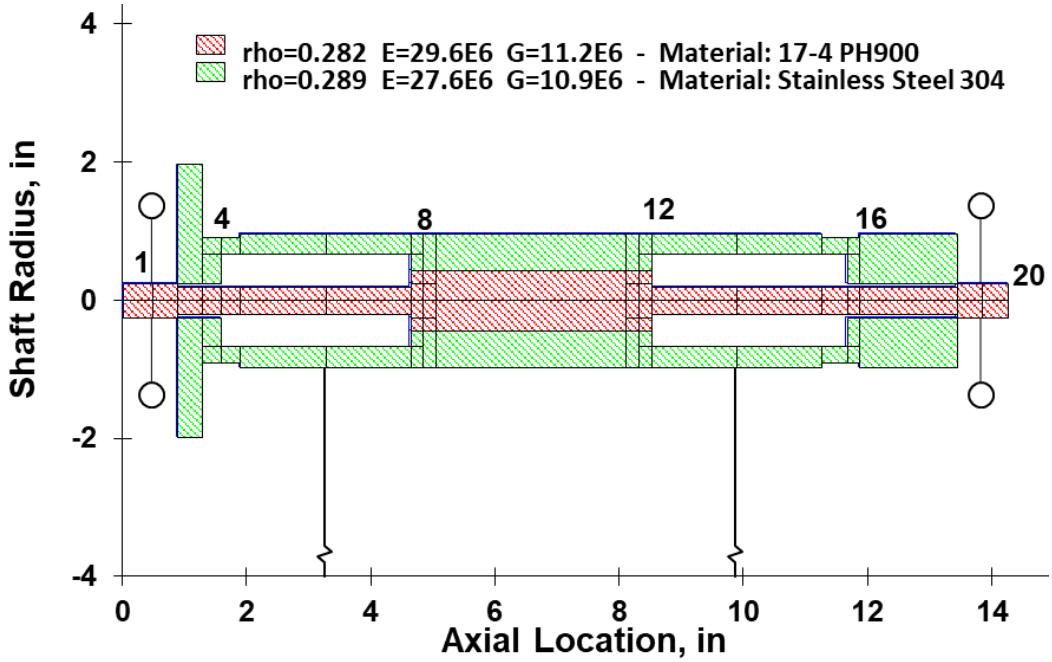

Figure 3-9 Beam element model of the shaft

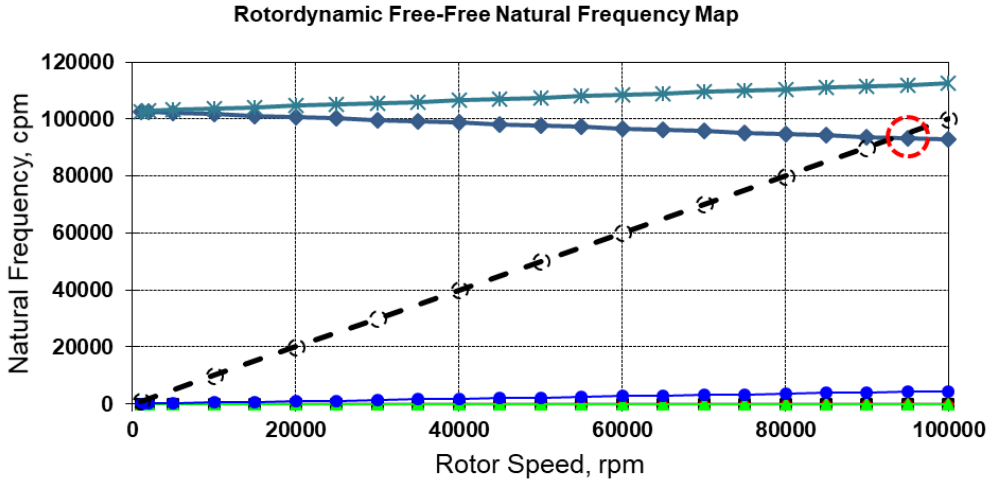

Figure 3-10 Shaft free-free natural frequency map

The free-free natural frequency of the shaft is measured after the shaft is assembled using 3,500 psi tension force. Figure 3-11 shows the setup for measuring the

shaft free-free natural frequency. Free-free natural frequency are measured by measuring the shaft vibration frequency using an accelerometer and applying an impact force to the shaft, while the shaft is hanged from a pair of long plastic ropes. Figure 3-12 shows the measured vibration frequency, the peak in the plot represents the bending mode natural frequency. It is observed that the shaft bending mode natural frequency is about 1,270 HZ (76,200 rpm). Since the bending mode natural frequency is above the maximum operating speed, it is acceptable to consider the shaft as a single rigid-body shaft.\

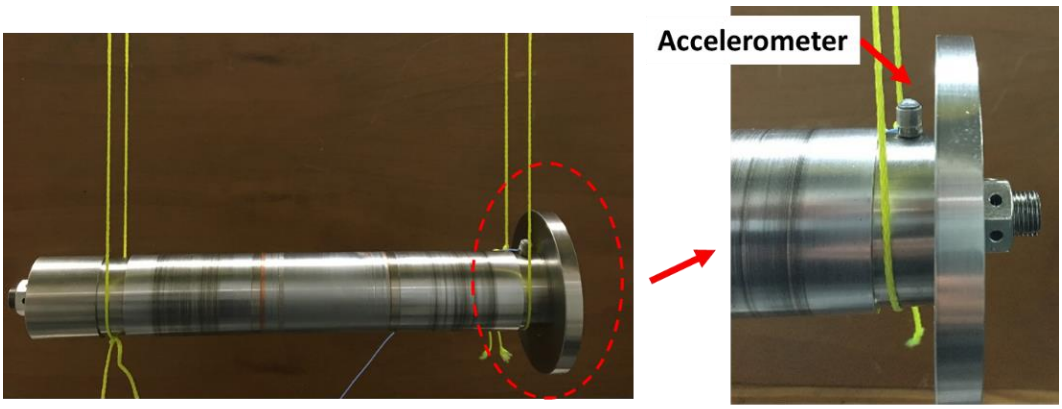

Figure 3-11 Shaft natural frequency measurement setup

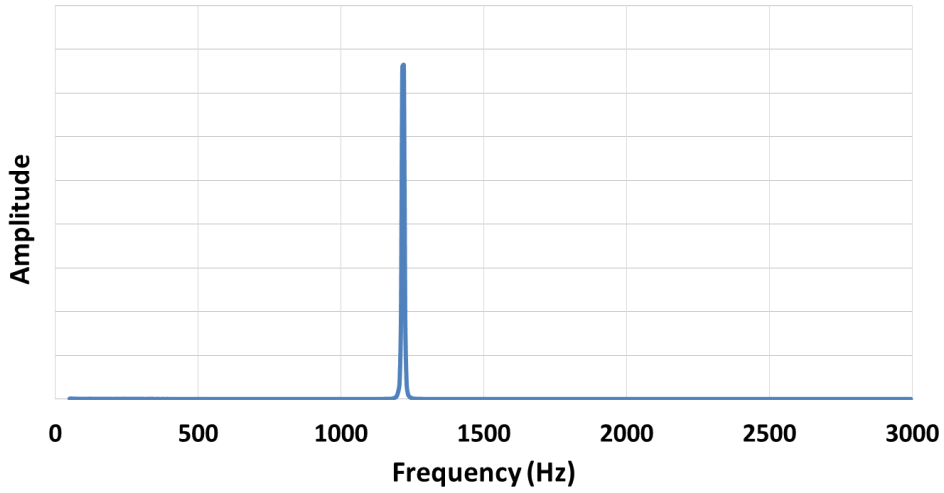

Figure 3-12 Shaft natural frequency measurement

3. 3. Air foil thrust bearing manufacturing and parameters

A set of air foil thrust bearings (AFTBs) are used to constrain the rotor's axial motion. Figure 3-13 shows the six pad AFTB that is used for rotordynamic test rig. Top foils are made from stainless steel material (0.127 mm thickness). Each top foil is spot welded to an assembly shim at the leading edge. The assembly shim is fixed on the bearing housing using a screw and a locating dowel pin.

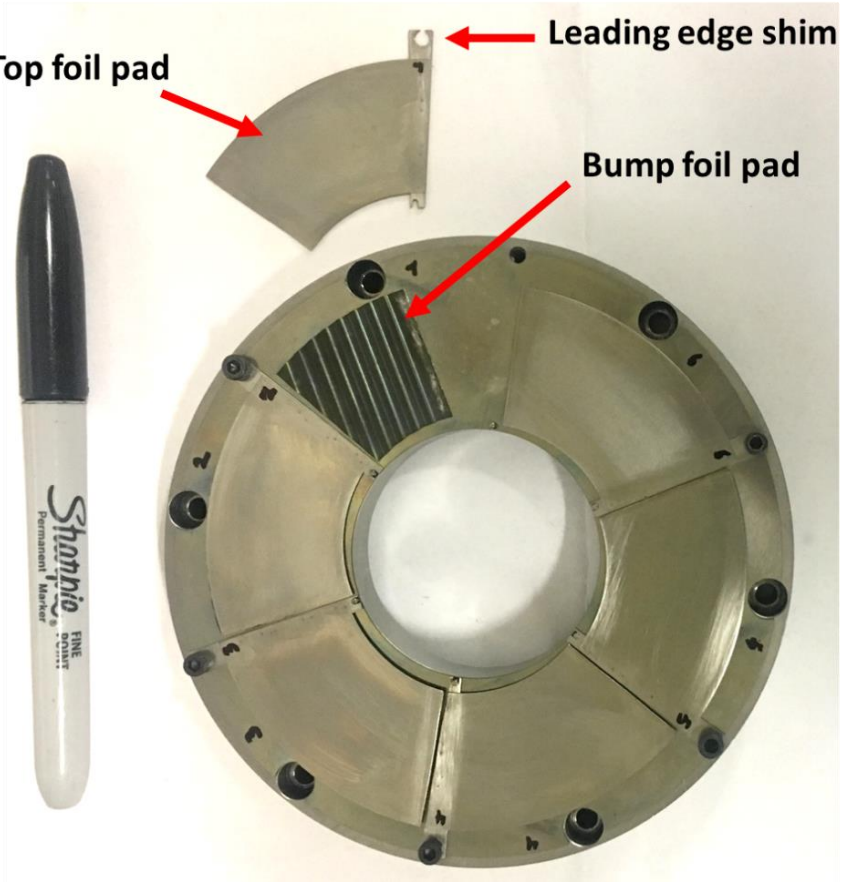

Figure 3-13 Six pad thrust air foil bearing

Figure 3-14 shows the forming jig for AFTB bump foils. Each bump foil stripe has eight bumps, distributed radially. Bump foil stripes are spot welded on the back plate, and they cover half of the top foil arc angle. Bump foils are made from Inconel 750 (0.127 mm thickness). Measured bump height distribution for one bump foil stripe is presented in Table 2. Based on measured values, the bump height is 0.456 +/- 0.003 mm.

Figure 3-14 Thrust bearing bump foil tooling for radial bump foil arrangement

Table 2 Bump height measurement for thrust bearing bump foil

Bump #	Bump height (mm)		
1	0.460	0.458	0.458
2	0.460	0.456	0.457
3	0.455	0.456	0.454
4	0.454	0.453	0.453
5	0.454	0.454	0.453
6	0.453	0.453	0.453
7	0.453	0.452	0.452

3. 4. High-speed rotordynamic test rig and experimental instrumentation

Figure 3-15 shows the cross-section view and the general layout of the high-speed rotordynamic test rig which is used to conduct experimental analysis. Test rig housing holds two radial HAFBs on each side of the motor, and one set of double acting AFTB on the thrust runner side. A 10 KW built-in, two-pole, asynchronous, high-speed and medium frequency induction motor, drives the test rig. The cooling jacket around the motor stator provides thermal management for the motor stator. The cooling jacket has a series of circumferential grooves (channels), and the pressurized air is injected to the grooves to remove the heat from the motor stator. Two sets of orthogonally positioned eddy current sensors, located next to each HAFB, record the rotor vibration in the horizontal and the vertical directions. The eddy current sensors (Bently Nevada 8 mm 3300 XL Series Proximitor System) have a linear range of 2 mm, with 0.25 mm minimum distance from the target, and maximum distance of 2.3 mm (approximately 1 to 17 Vdc). Due to the operating nature of eddy current sensors, the gain and offset values of the eddy current sensors depend on the material and the geometries of the target. Therefore, all proximity sensors are calibrated using the actual shaft, and for the same location based on their position in the test rig

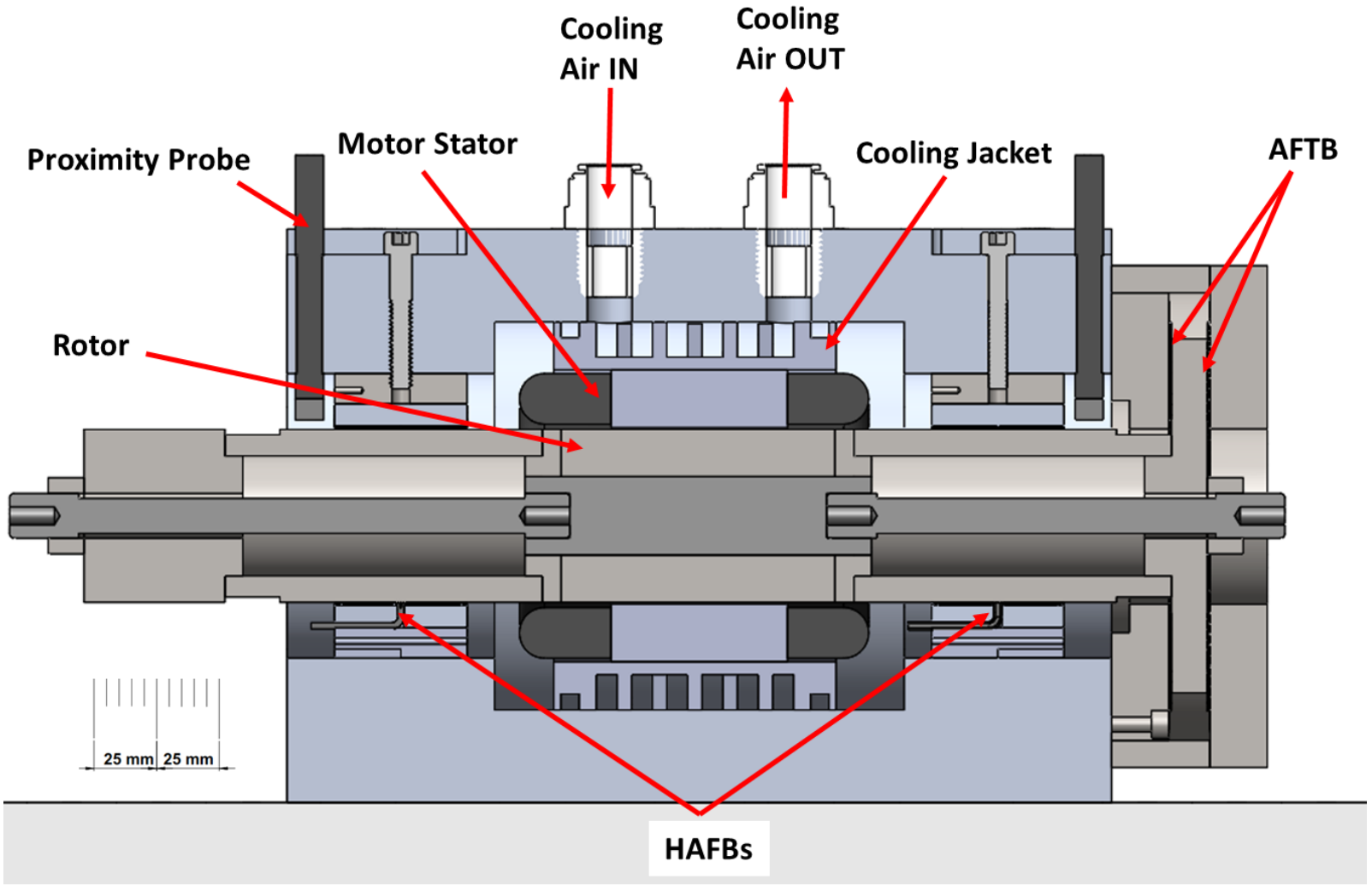

Figure 3-15 Cross-section view of high-speed rotordynamic test rig

Chapter 4

ROTORDYNAMIC ENHANCMENT BY CONTROLLED HYDROSTATIC INJECTION OF HYBRID AIR FOIL BEARING

This chapter presents the analytical and experimental evaluation of the rotordynamic performance of a rotor supported by two three-pads HAFBs with the controlled hydrostatic injection, which utilizes the injections at particular locations to control eccentricity and attitude angle. For the numerical analysis, both time-domain orbit simulations and frequency-domain modal analyses are presented. In the experimental analysis, the simulation results are verified by measuring the rotor imbalance responses in a high-speed test rig.

4. 1. Rotor-HAFB imbalance response prediction for controlled hydrostatic injection

The first part of the simulations is the imbalance response prediction of rotor-HAFB via time-domain orbit simulations. The time-domain orbit simulation solved the time-space dependent pressure distribution inside the bearing's air film. By deploying the orbit simulation to solve the nonlinear governing equations in the time domain, it is possible to capture the nonlinear phenomena that happen in the rotor-bearing system, such as limit cycle behavior of the rotor that is the nonsynchronous rotor vibration. The predicted imbalance responses of the rotor at the sensor locations during the speed-up simulations are used to identify the onset speed of instability. Simulated imbalance response are from 3,000 rpm up-to the speed that the amplitude of the subsynchronous vibration becomes more than the bearing radial clearance. The speed increment is 1,000 rpm and the simulations are carried out for as many cycles as required to achieve the steady-state orbit at each speed. The test rig is designed in a way that the HAFBs are located symmetrically from the rotor's mass center of gravity. Since the two HAFBs are identical, it is assumed that each bearing carries half of the rotor's weight.

A pair of three pad HAFBs (Figure 4-1) are used for investigation of the controlled hydrostatic injection. The three-pad HAFBs have three orifices with one orifice welded in the middle of each top foil pad. The overall geometries and parameters of the three pad HAFBs are given in Table 3 and the exploded view of a three pad HAFB is shown in Figure 4-2.

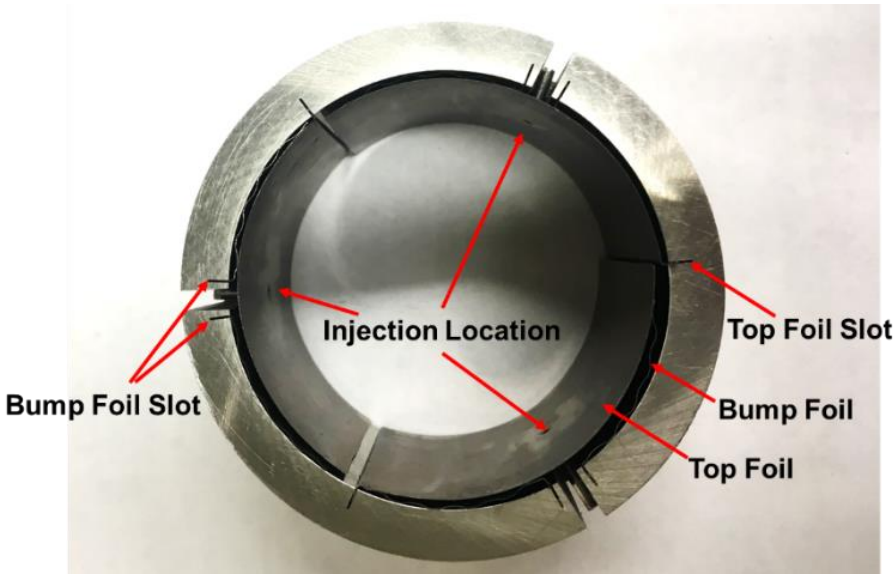

Figure 4-1 Three pad HAFB

Table 3 Three pad HAFB parameters

Parameters	SI Unit	English unit
Bearing axial length, L	37.5 mm	1.476 in
Bearing nominal radial clearance, C	0.07 mm	0.003 in
Hydrodynamic preload of each pad, r_p	0.03 mm	0.001 in
Offset ratio, γ	0.5	
Number of bumps per pad, N_{bumps}	11	
Top foil thickness	0.152 mm	0.006 in

Bump foil thickness	0.152 mm	0.006 in
Bump height	0.406 mm	0.016 in
Orifice tube outer diameter	1.829 mm	0.072 in
Orifice tube inner diameter	1.529 mm	0.060 in
Supplied hydrostatic pressure, P_s	4.14 bar	60 psi

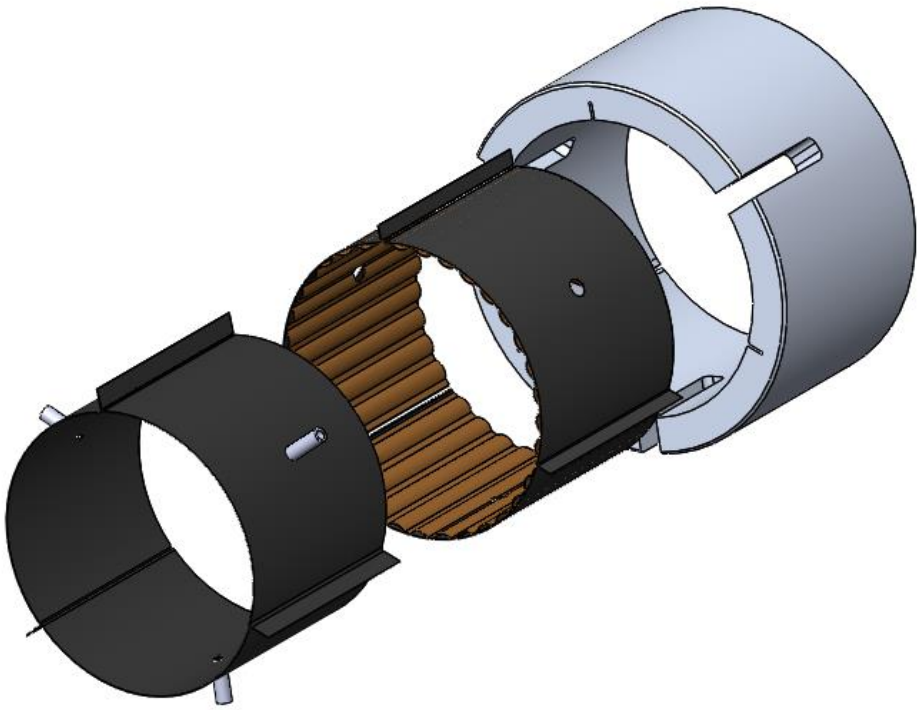

Figure 4-2 Exploded view of three pad HAFB

The shaft that is used for rotordynamic evaluation is described in chapter 3. The overall parameters of the shaft are given in Table 4.

Table 4 Rotor parameters

Parameters	SI Units	English Units
Rotor length, L_r	302 mm	11.89 in
Rotor mass, m_r	4.84 kg	10.67 lbm
Rotor radius at bearings location R	24.5 mm	0.964 in
Bearing span L_b	165.1 mm	6.4 in
Rotor imbalance mass	2500 mg-mm	0.217 lbm-in
Rotor transverse moment of inertia, I_T	0.051 $\mathrm{kg\,mm^2}$	0.00017 $\mathrm{lbm\ in^2}$
Rotor polar moment of inertia, I_P	0.002 $\mathrm{kg\,mm^2}$	0.000007 $\mathrm{lbm\ in^2}$

In the following numerical analysis, rotordynamic performance for three different cases are predicted and compared. For case-1, both HAFBs are operating with all three orifices closed (pure hydrodynamic operation). For Case-2, the HAFBs are operating with all orifices open (full hybrid operation). For case-3, the system starts with all three orifices open, and after the HAFBs hydrodynamic pressure is fully built-up, the bottom orifice is closed and rotor speed-up continues with the two top orifices open.

4. 1. 1 Case-1: Pure hydrodynamic operation

In this section, prediction results for the case when both bearings are operating on a pure hydrodynamic mode (all three orifices are closed) are presented. Figure 4-3 presents the waterfall plots of the rotor's vibration with an in-phase imbalance of 2,500 mg-mm, when both bearings are operating on a pure hydrodynamic mode The onset speed of subsynchronous vibration is around 22,000 rpm. Amplitude of the subsynchronous vibration grows and becomes larger than the bearing radial clearance around 30,000 rpm. The critical speeds along X and Y directions are around 12,000 rpm and 4,000 rpm respectively. Since the X direction is the bearing's loading direction (the

gravity direction), the critical speed is higher in the X-direction compares to the Y-direction. The larger subsynchronous vibration has the same frequency as the critical speed along the Y-direction, and the frequency of the smaller subsynchronous vibration matches to the critical speed along the X-direction. Figure 4-4 shows the predicated synchronous imbalance response when both bearings are operating on a pure hydrodynamic mode. For the case with in-phase imbalance, the frequency of the critical speed matches to the frequency of the subsynchronous vibration observed in the waterfall plots.

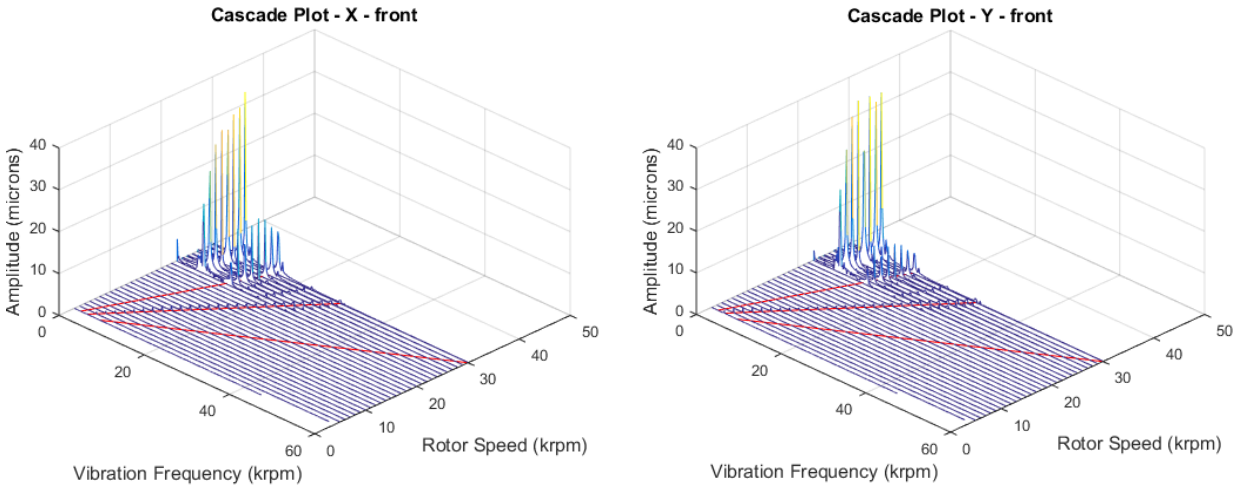

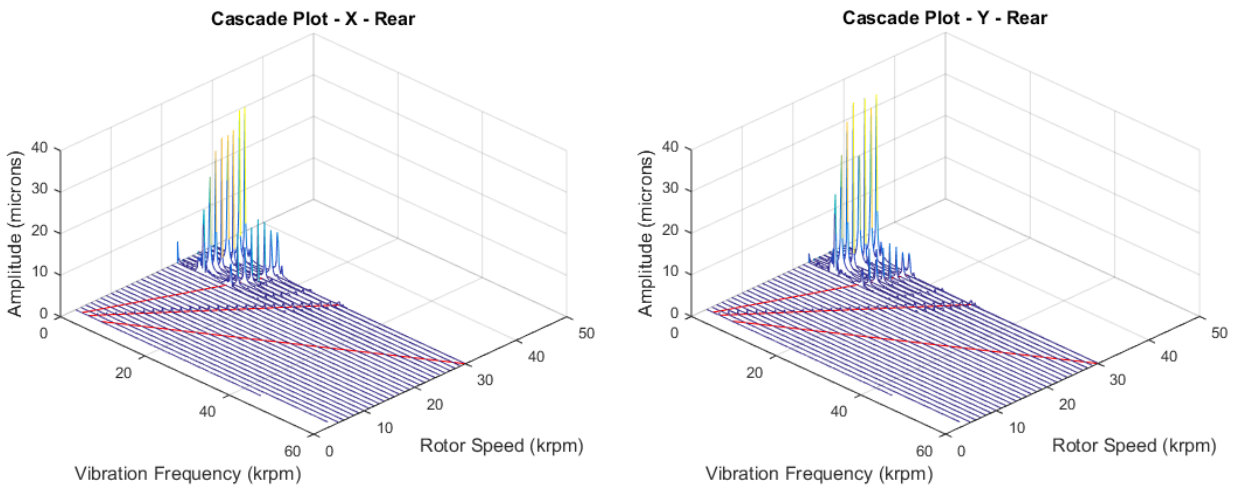

Figure 4-3 Simulated waterfall plots for the pure hydrodynamic operation

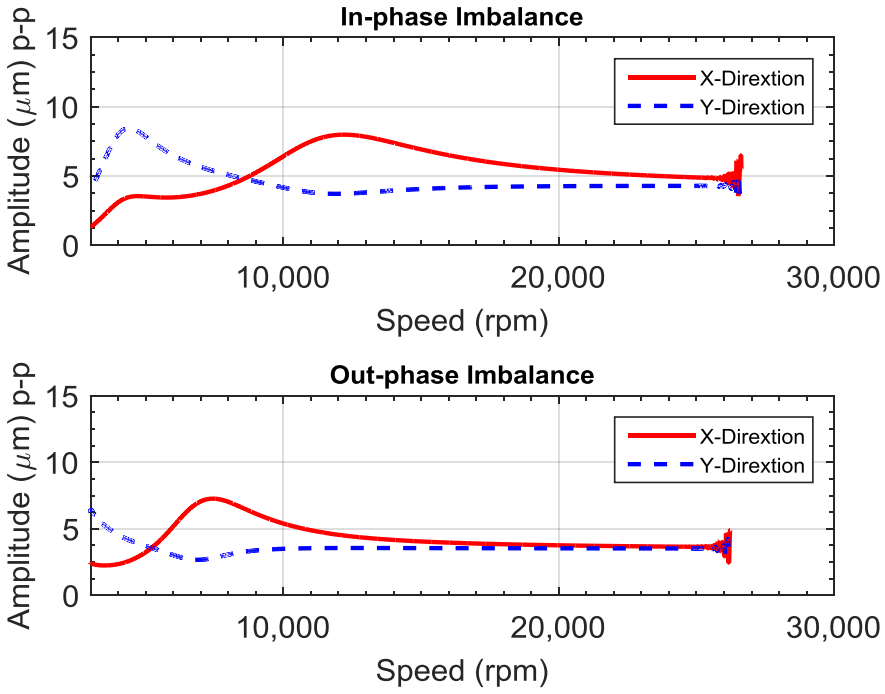

Figure 4-4 Predicted synchronous peak-to-peak vibration of the rotor with pure hydrodynamic bearings for in-phase and out-phase imbalances

4. 1. 2 Case-2: Full hybrid operation

Figure 4-5 shows the waterfall plots when both bearings are operating with all three orifices open (denoted as “full hybrid mode”). The supply pressure is 4.14 bar. The onset speed of subsynchronous vibration appears to be around 32,000 rpm. The bounded subsynchronous vibration grows gradually as the speed increases, and the maximum speed of the rotor is extended up to 50,000 rpm (improvement in maximum operating speed is observed compared to the pure hydrodynamic mode), at which the subsynchronous vibration becomes larger than the bearing radial clearance. Figure 4-6 is the predicted synchronous vibration when both bearings are operating on the full hybrid mode. Compare to the pure hydrodynamic mode, enhancement in the onset speed of instability is observed. However, the amplitude of vibrations at the critical speed is higher compare to ones for the pure hydrodynamic mode.

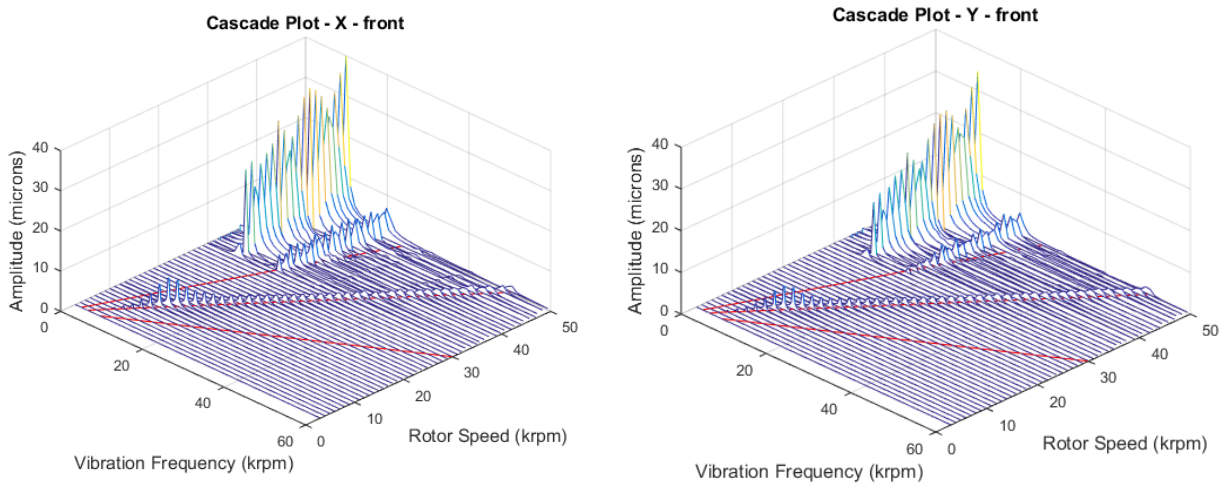

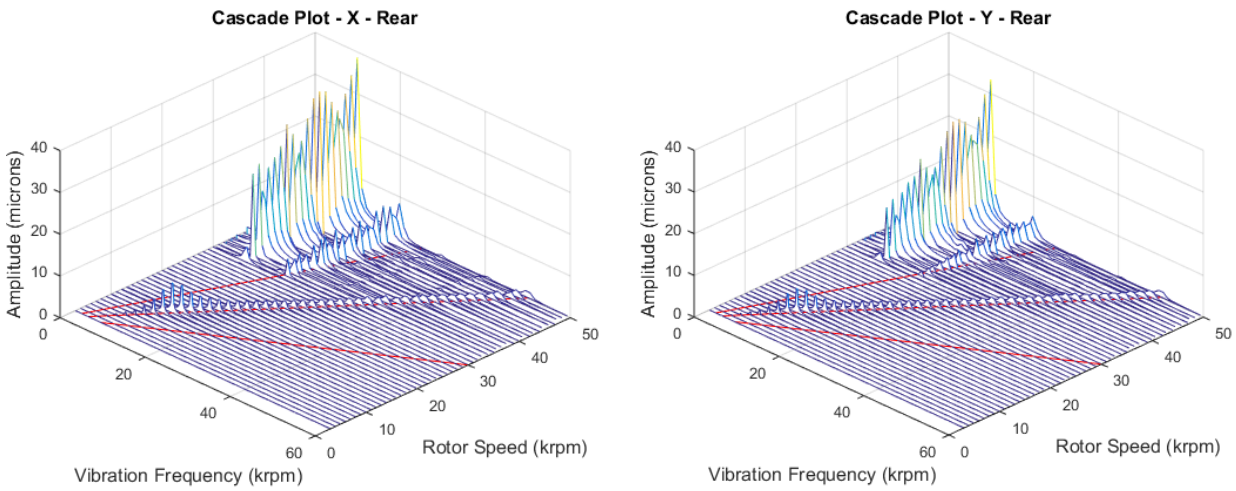

Figure 4-5 Simulated waterfall plots for the full hybrid operation

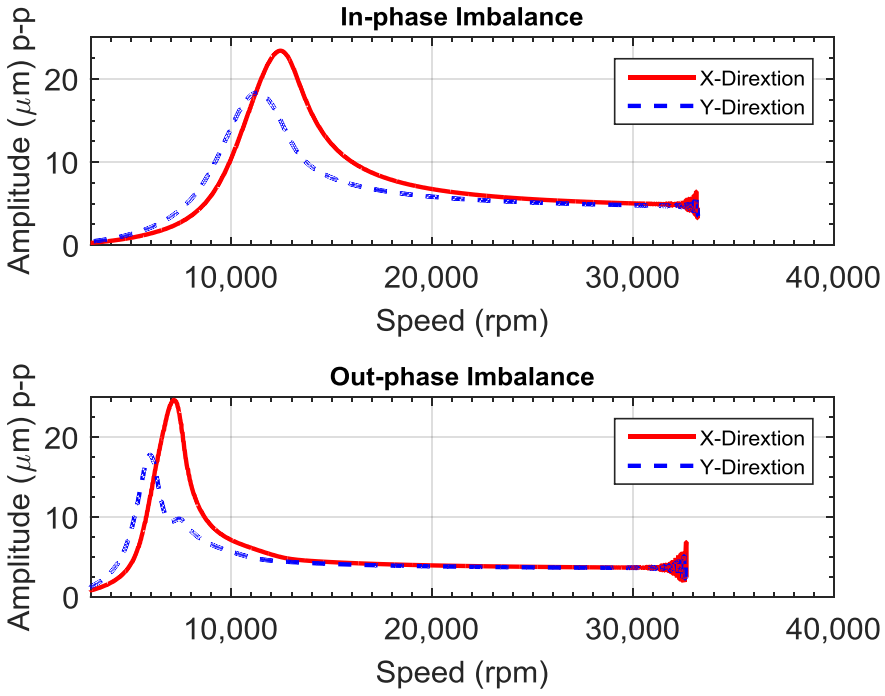

Figure 4-6 Predicted synchronous peak-to-peak vibration of the rotor with the full hybrid operation for in-phase and out-phase imbalances

4. 1. 3 Case-3: Controlled hybrid operation

Figure 4-7 presents the waterfall plots for the case of both HAFBs operating with a controlled hydrostatic injection, where the bottom orifice ($\theta = 180^{\circ}$) is closed at speeds higher than 6,000 rpm while the two top orifices ($\theta = 60^{\circ}, 300^{\circ}$) are remained open (denoted as “controlled hybrid mode”). The onset speed of subsynchronous vibration is further delayed to around 44,000 rpm. In comparison to the hydrodynamic mode and full hybrid mode, a significant enhancement in stability of the rotor-bearing system is observed. From the predicted synchronous responses for the controlled hybrid mode (Figure 4-8), it is observed that the amplitude of vibration at the critical speed is lower than the hybrid mode, and the onset speed of instability is higher than both pure hydrodynamic mode and full hybrid mode.

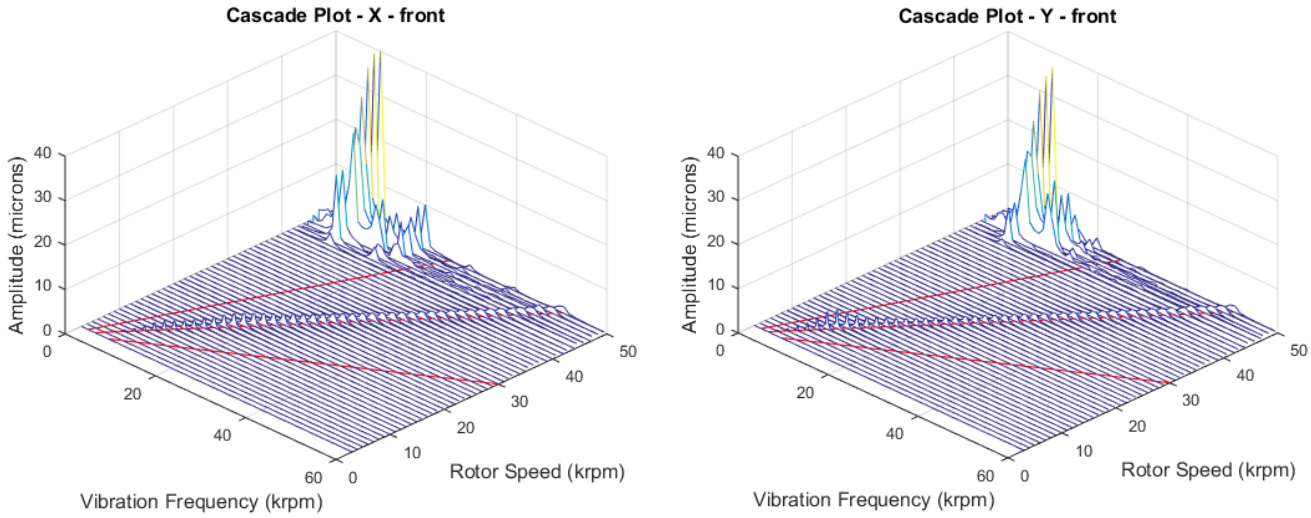

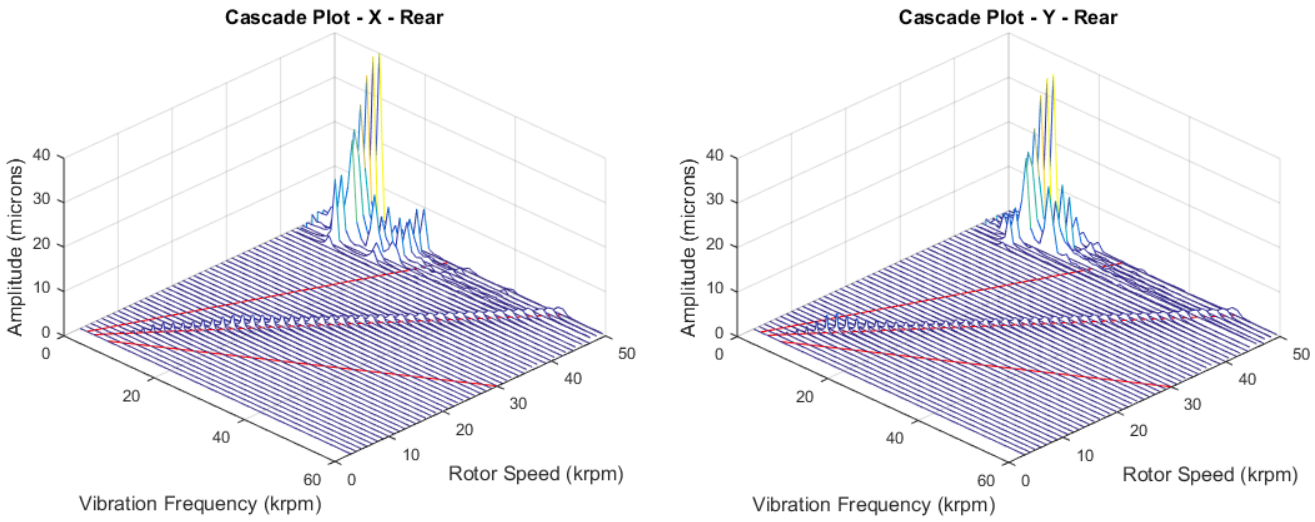

Figure 4-7 Simulated waterfall plots for the controlled hybrid operation

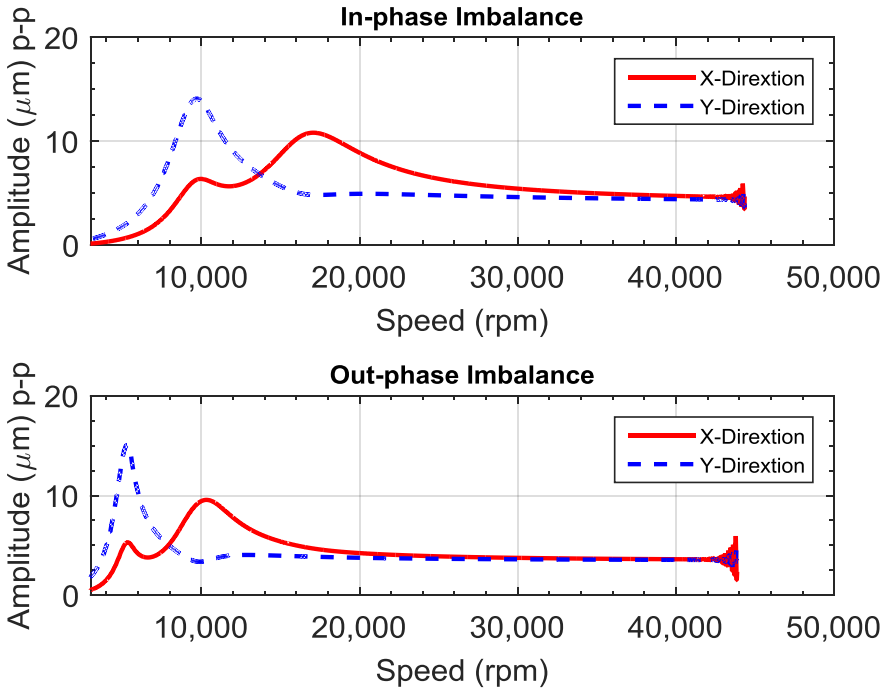

Figure 4-8 Predicted synchronous peak-to-peak vibration of the rotor with the controlled hybrid operation for in-phase and out-phase imbalances

The predicted rotor eccentricity ($e = \sqrt{e_x^2 + e_y^2}$) and attitude angle versus the rotor's speed are presented in Figure 4-9 (a) and Figure 4-9 (b) respectively. In general, a combination of a large eccentricity and a small attitude angle results in a small cross-coupled stiffness and a higher stability. The controlled injection mode results in the largest eccentricity, but the attitude angle is not the smallest (However it is smaller than the hydrodynamic mode up to about 36,000 rpm). Interestingly, the full hybrid mode results in the smallest attitude angle and eccentricity for the entire simulated speeds. The hydrodynamic mode results in a relatively large eccentricity but its attitude angle is very large from the very low speed, which causes the hydrodynamic mode to be the most unstable case.

In summary, stability characteristics of the bearing is a result of the combinational effect of the rotor eccentricity and attitude angle. It is possible to optimize the circumferential location of the hydrostatic injections to increase the eccentricity while maintaining the attitude angle small.

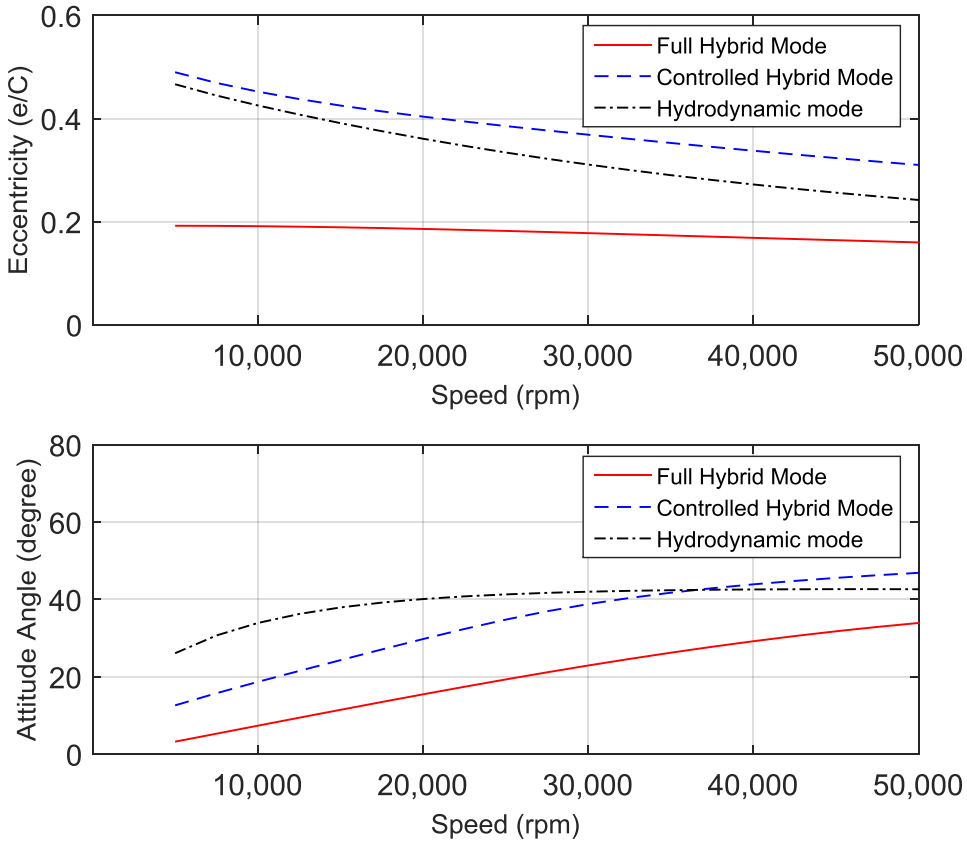

Figure 4-9 Predicted rotor's eccentricity and attitude angle versus speed

Figure 4-10 shows the simulated orbit ($\varepsilon = e/C$) at 40,000 rpm for (a) full hybrid mode and (b) controlled hybrid mode. Dashed line represents the bearing clearance. A large subsynchronous vibration is observed for the full hybrid mode. Figure 4-11 shows the normalized pressure ($P = p/p_a$) contour in the film at 20,000 rpm for (a) hydrodynamic mode, (b) full hybrid mode, and (c) controlled hybrid mode. For all three cases, the bottom top foil pad has the peak pressure. Figure 4-12 shows the non-dimensional film thickness profile ($H = h/C$) at 20,000 rpm for (a) hydrodynamic mode,

(b) full hybrid mode, and (c) controlled hybrid mode. As it is expected, the bottom top foil pad has the lowest film thickness for all three cases.

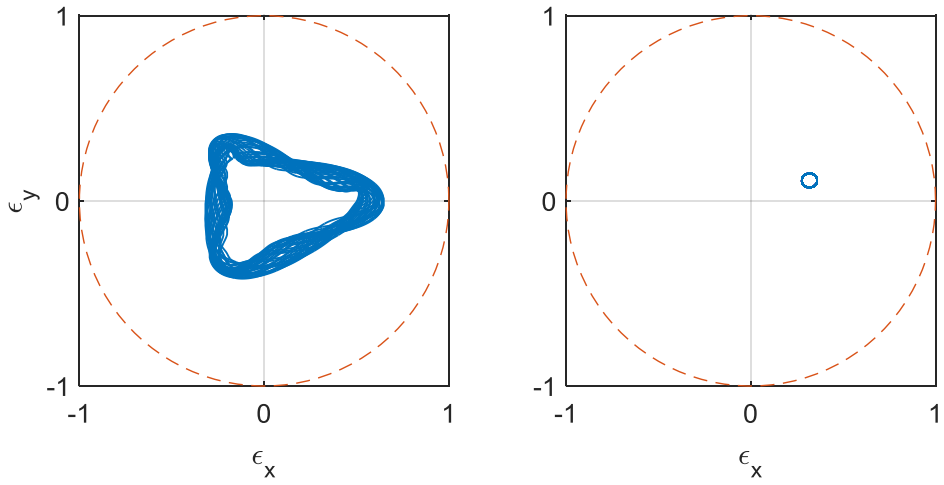

Figure 4-10 Simulated orbits at 40,000 rpm (a) Full hybrid (b) Controlled hybrid operation

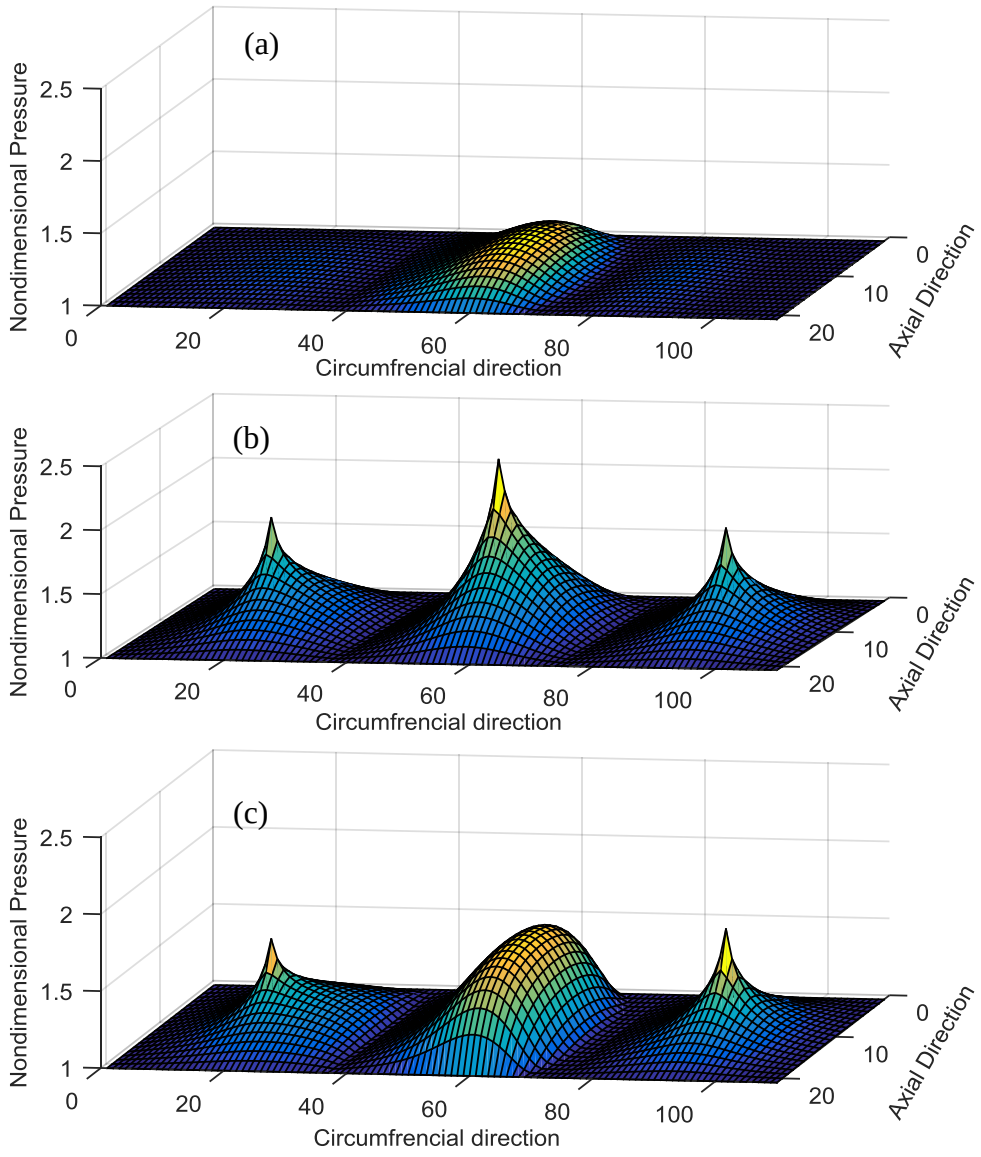

Figure 4-11 Normalized pressure profile at 20,000 rpm (a) Hydrodynamic operation (b) Full hybrid operation(c) Controlled hybrid operation (Feed pressure is 4.14 bar)

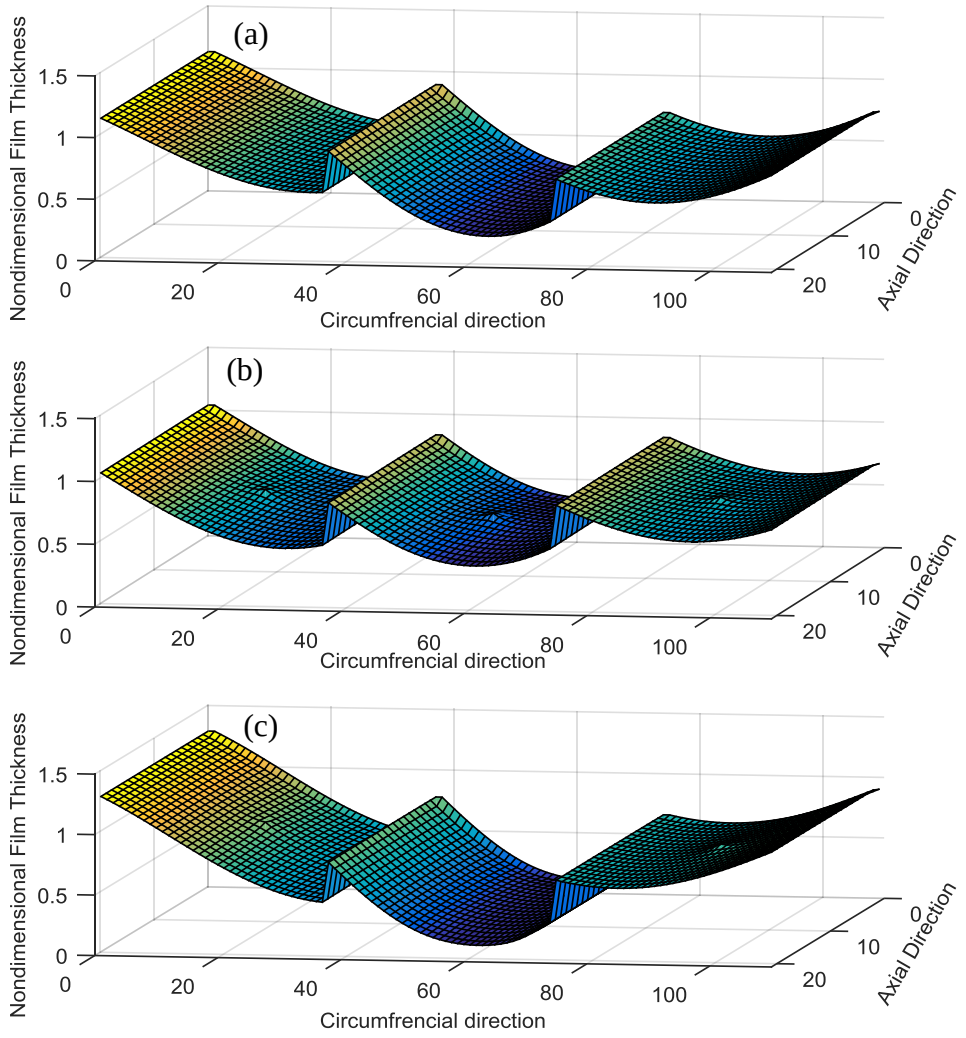

Figure 4-12 Normalized film thickness profile at 20,000 rpm (a) Hydrodynamic operation (b) Full hybrid operation(c) Controlled hybrid operation (Feed pressure is 4.14 bar)

4. 2. Modal Analysis

It is noted that the frequency domain modal analyses, using the excitation frequency-dependent bearing coefficients, provide better insight to the stability characteristics of the rotor-bearing in different operating modes. Modal analyses for both cylindrical and conical modes are presented in Figure 4-13 and Figure 4-14. The

hydrodynamic AFB and the HAFB with the full hybrid operation have a negative modal damping at the low excitation frequencies. For the HAFB operating with the controlled hybrid mode, the modal impedances are not only positive for the entire frequencies (both cylindrical and conical modes), but also they are larger than those of the hydrodynamic mode and the full hybrid mode. The frequency domain analyses show that the overall stability of the rotor-bearing system is improved significantly when HAFBs are operating on the controlled hybrid mode, and the results also confirm the rotordynamic analyses from the time–domain orbit simulations.

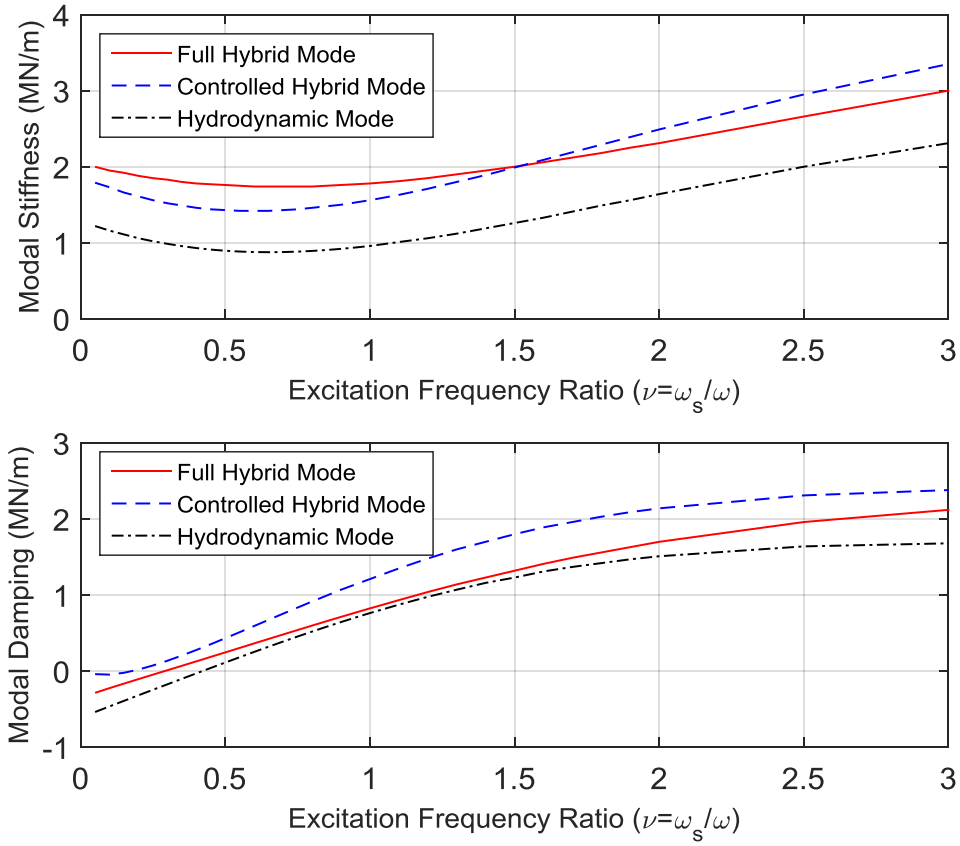

Figure 4-13 Modal impedances for the forward whirl versus the excitation frequency ratio for cylindrical mode at 40,000 rpm

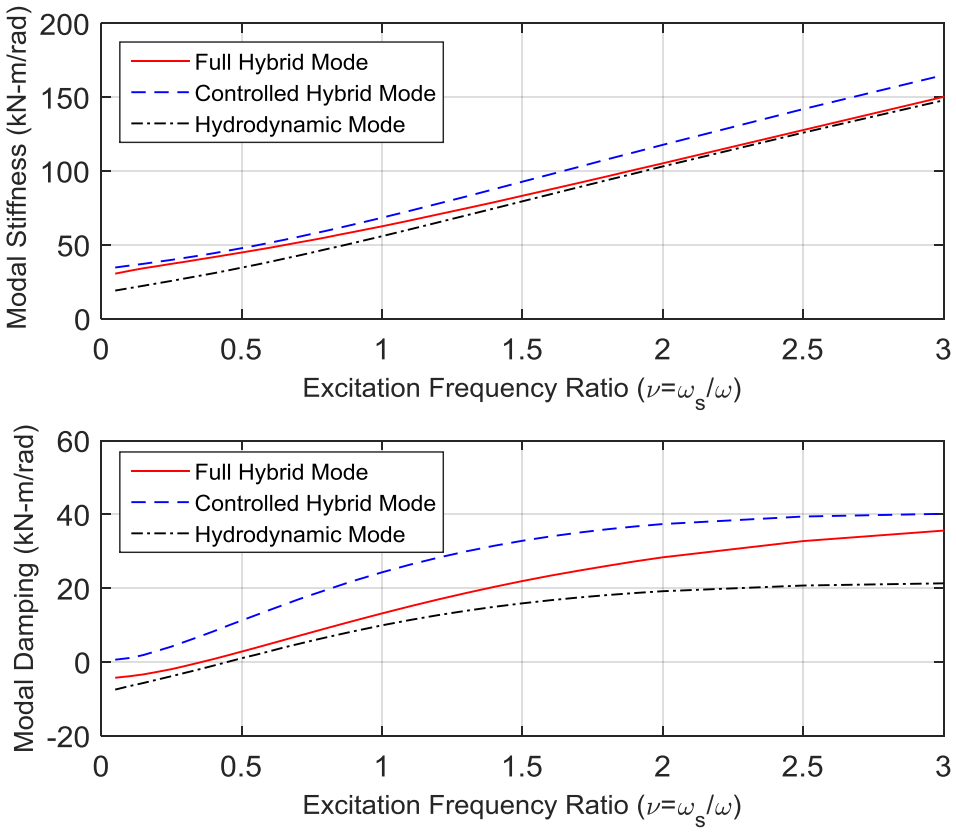

Figure 4-14 Modal impedances for the forward whirl versus the excitation frequency ratio for conical mode at 40,000 rpm

4. 3. Rotor-HAFB imbalance response measurement results and comparison to prediction

Numerical analyses are compared with the experimental results adopted from [64]. The experimental analyses consist of the measured imbalance responses for both full hybrid mode the controlled hybrid mode. For the controlled hybrid mode, the experiments starts with all orifices open (with supply pressure of 4.14 bar), and the bottom orifice is closed once subsynchronous vibration begins to appear. Figure 4-15 presents the measured imbalance responses of the rotor at (a) 35,000 rpm (b) 40,000

rpm and (c) 45,000 rpm. For the full hybrid case, a bounded subsynchronous vibration with the vibration frequency of about 9,000 rpm (942 Hz) is detected. For all the three speeds, closing the bottom orifice eliminates the subsynchronous vibration while the amplitudes of synchronous vibrations remain unchanged. Figure 4-16 presents the predicted rotor imbalance response at various speeds for both full hybrid mode and controlled hybrid mode. The predicted imbalance responses match to the test results in general tendency; the subsynchronous vibrations are disappeared or are substantially reduced when the bottom orifice is closed. However, there is a substantial difference in the magnitude of both subsynchronous and synchronous vibrations. The measured synchronous vibration is much larger than predictions because the raw data contains the rotor run out and additional artifact possibly from the variation of magnetic permeability (affecting the characteristics of eddy current type probes) of the rotor surface along the circumferential direction.

The difference in the subsynchronous vibrations needs more attention. The amplitude of the measured subsynchronous vibration is much lower than predictions. There are several factors to consider. Firstly, equivalent viscous damping coefficients of the bump foils are calculated from the structural loss model given by Eq. (4-1);

$$c_{bump} = \frac{\eta k_{bump}}{\omega_s} \tag{4-1}$$

, where c_{bump} and k_{bump} are the equivalent viscous damping coefficient and stiffness coefficient of bump foils (independent spring-dampers in the current model), η is an empirical parameter for the structural loss factor of each independent spring-damper, and ω_s is the excitation frequency to the independent spring-damper. Typically, structural loss factor of the entire support structure of the bearing is determined by the load vs. displacement measurement for the entire bearing [51], but the structural loss factor of the

entire bearing cannot be necessarily interpreted as the loss factor of an individual bump (or independent spring-damper). In addition, current orbit simulations use the synchronous frequency (rotor speed) for the excitation frequency in the denominator of Eq. (4-1). When there are both subsynchronous and synchronous vibrations at the same time, the motions of the bumps are much more complicated than a simple harmonic motion synchronous to the rotor speed. The nature of complicated motion of the bump foils prevents accurate prediction of subsynchronous vibrations and their magnitude using the currently available structural model, Eq. (4-1).

One approach is to apply the subsynchronous excitation frequency observed in the experiment to Eq. (4-1) and with higher loss factors than 0.2, which was used for Eq. (4-1) in the baseline simulations. To investigate the effect of the different loss factors and the excitation frequency on the rotor imbalance response, different cases are compared (see Figure 4-16). For Case 1, $\omega_s = \omega$ and the loss factor is 0.2. For Cases 2, 3 and 4, the loss factor is 0.2, 0.5 and 0.8 respectively with $\omega_s = 942.48$ rad/s (9,000 rpm). The purpose of the augmented loss factors is to account for possibly more damping due to more complicated nature of the bump dynamics than the simple harmonic motion of independent spring-damper model. From Figure 4-16 it is observed that case-1 has the largest subsynchronous vibration. For the Cases-2, 3 and 4, the amplitudes of the subsynchronous motions are reduced but they are still much larger than those from the experiment.

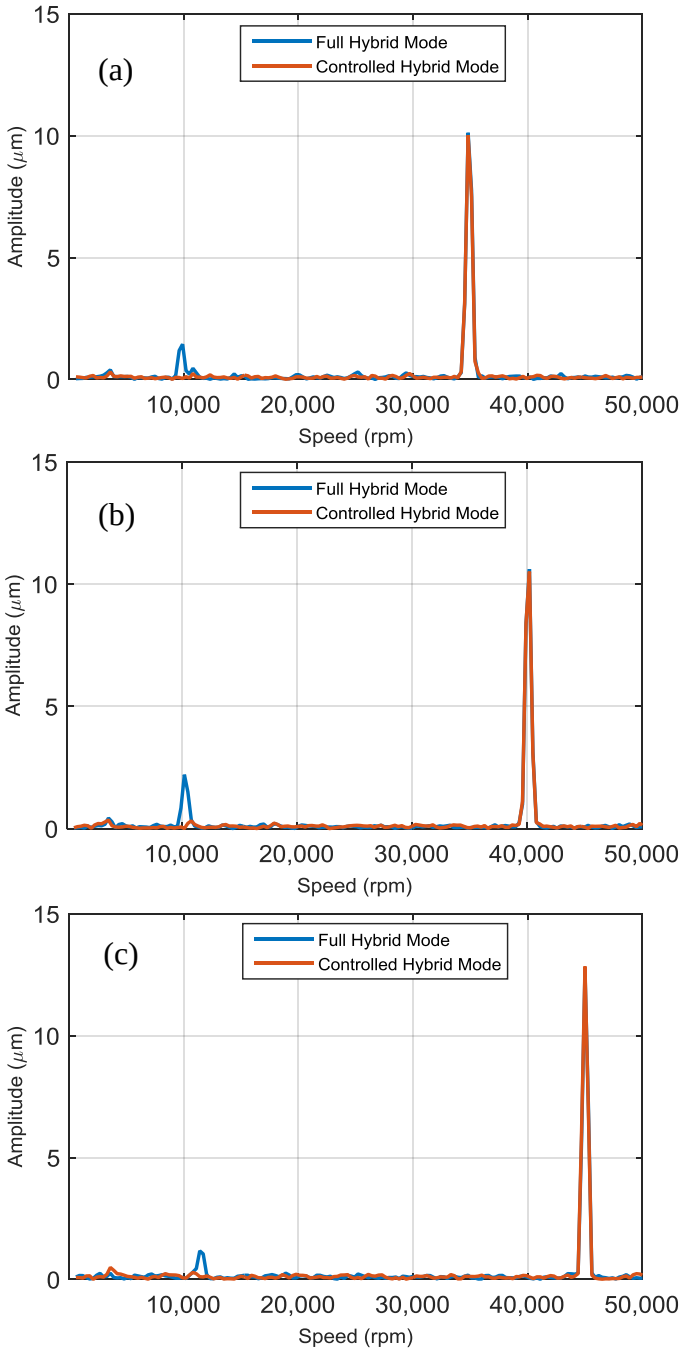

Figure 4-15 Rotor imbalance response; (a) 35,000 rpm (b) 40,000 rpm (c) 45,000 rpm

(Feed pressure is 4.14 bar) (Adopted from [64])

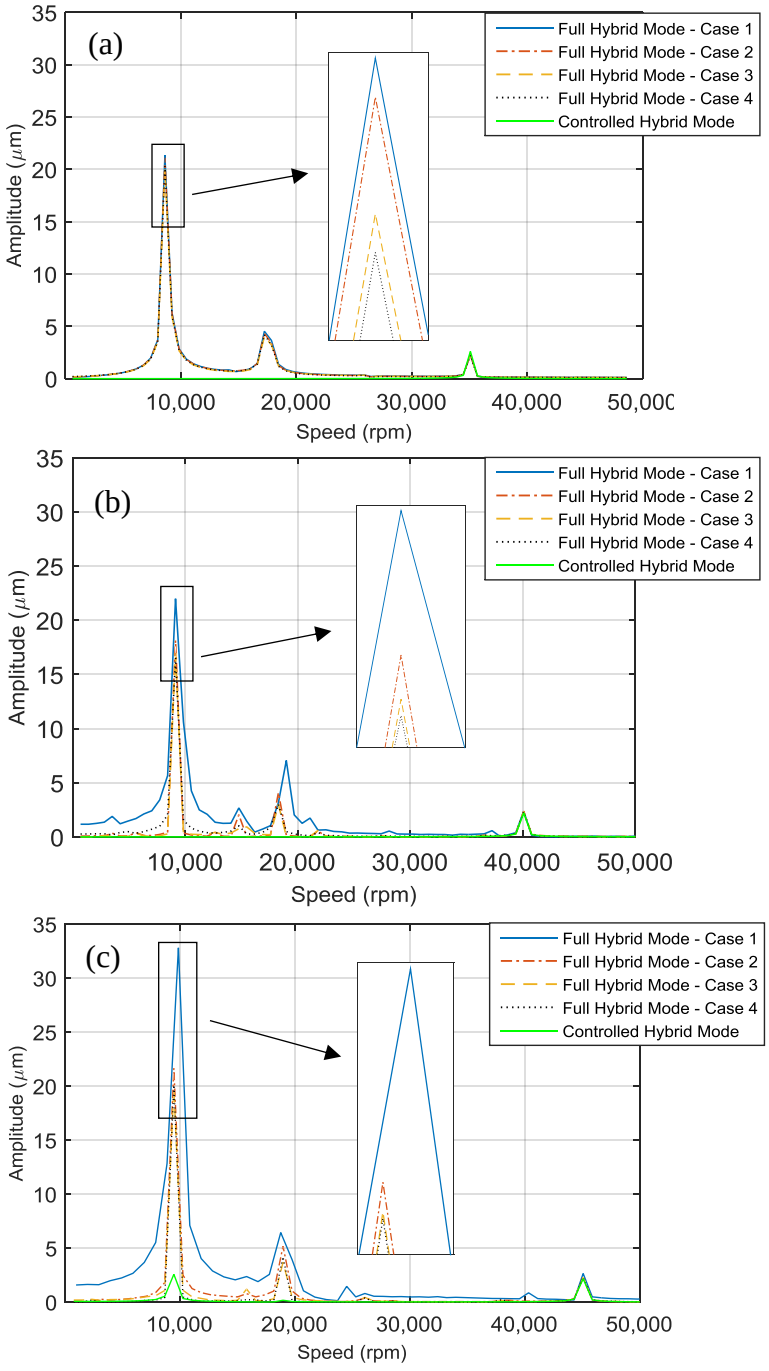

Figure 4-16 Simulated rotor imbalance response; (a) 35,000 rpm (b) 40,000 rpm (c) 45,000 rpm (Feed pressure is 4.14 bar[64])

Chapter 5

EFFECT OF ANGULAR LOCATION FOR HYDROSTATIC RADIAL INJECTION ON THE ROTOR-HAFB ROTORDYNAMIC PERFORMAEC

In the previous chapter, it was shown that the semi-active operation of HAFB significantly enhances the rotordynamic performance. However, the effect of circumferential location of the hydrostatic injection is chosen to be in the middle of top foil pads. Next, it is crucial to consider the effect of the circumferential location of hydrostatic injection on the rotordynamic stability of HAFBs. The circumferential position of hydrostatic injections in HAFBs can be optimized based on the rotor attitude angle and eccentricity to further improve the dynamic characteristics of HAFBs. In general, a large attitude angle and small rotor eccentricity lead to higher rotordynamic instability. The circumferential location of hydrostatic injection in HAFBs can be adjusted to achieve a large eccentricity and small attitude angle. To address this objective, this chapter presents predictions and measurements of rotordynamic performance of rotor-HAFB system with different angular location of hydrostatic injection. The following analysis consists of rotor-HAFB performance prediction through time-domain orbit simulation and frequency domain modal analysis. Furthermore, the prediction results are confirmed using a high-speed rotordynamic test rig.

5. 1. Rotor-HAFB imbalance response prediction with different hydrostatic injection locations

For the analysis, three sets of single-pad HAFBs are constructed with different circumferential positions of orifices. Each set has three orifices which inject externally pressurized air into the bearing clearance. All three sets of single-pad HAFBs have identical geometries except for the circumferential location of orifices. The first set of HAFBs (case-1) has orifices located at 30, 180, and 330 degrees (Figure 1). The orifices

of second set (case-2) are located at 60, 180, and 300 degrees. For the third set (case-3), the orifices are located at 90, 180, and 270 degrees. In general, all three cases have a single orifice at the bottom (opposite to the loading direction), but the angular locations of the two top orifices are different for each case. The overall geometries and parameters of the single-pad HAFBs are given in Table 5. The shaft parameters which is used for rotordynamic evaluation is given in Table 6.

Table 5 Parameters of single pad HAFB

Parameters	SI Unit	English Unit
Bearing axial length L	37.5 mm	1.476 in
Bearing radial clearance C	0.05 mm	0.002 in
Number of bumps N_{bump}	33	
Top foil thickness	0.127 mm	0.005 in
Bump foil thickness	0.127 mm	0.005 in
Bump height	0.406 mm	0.016 in
Orifice tube outer diameter	1.829 mm	0.072 in
Orifice tube inner diameter	1.529 mm	0.06 in
Supplied hydrostatic pressure p_s	4.14 bar	60 psi

Table 6 Shaft parameters

Parameters	SI Unit	English Unit
Rotor length L	318.351 mm	12.533 in
Rotor mass m_r	4.22 kg	9.303 lbm
Rotor radius at bearings location R	24.5 mm	0.964 in
Bearing span L_b	165.1 mm	6.5 in

Rotor imbalance mass m_{imb}	2532 mg-mm	0.22 lbm-in
Rotor transverse moment of inertia I_t	0.04383 $\mathrm{kg\,mm^2}$	0.00015 $\mathrm{lbm\,in^2}$
Rotor polar moment of inertia I_p	0.00201 $\mathrm{kg\,mm^2}$	0.0068×10^{-6} $\mathrm{lbm\,in^2}$

The following simulation analyses include the imbalance response of the rotor at the HAFB location during speed-up. The hydrostatic pressure supplied into the bearing film is 4.14 bar, and each bearing carried half of the rotor weight (two identical HAFBs are located symmetrically from the rotor mass center of gravity).

5. 1. 1 Case-1: Hydrostatic injection at 30, 180, and 330 degree.

Figure 5-1 shows the case-1 single-pad HAFB . Three orifices attached to the top foil with the angular location of 30, 180 and 330 degree provide the externally pressurized air in to the bearing clearance. The axial position of the orifices is at the center of the bearing sleeve

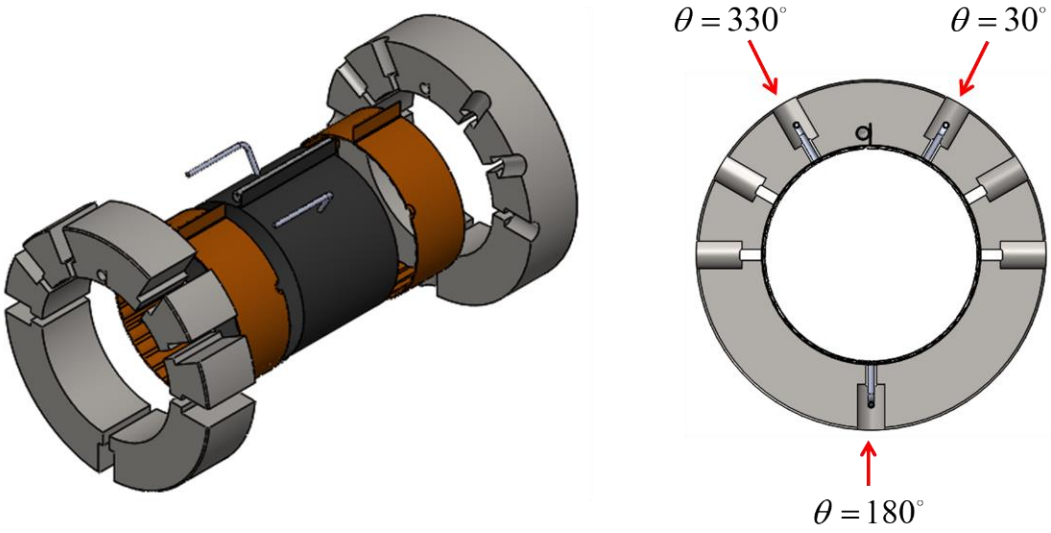

Figure 5-1 Front-view and isometric-view of case-1 single-pad HAFB

Figure 5-2 presents the predicted imbalance responses for the full hybrid mode and the controlled hybrid mode. The presented waterfall plots in Figure 5-2 are the imbalance responses of the rotor at the bearings location in the X-direction (vertical) and the Y-direction (horizontal). The waterfall plots are from 3,000 rpm up to the speed where the amplitude of subsynchronous vibration becomes larger than bearing's radial clearance. The speed increment for the waterfall plots is 1,000 rpm. For the case-1 HAFB (full hybrid operation), the subsynchronous vibration starts to appear around 34,000 rpm. For the controlled hybrid operation, the onset speed of instability is observed to be around 42,000 rpm. A significant enhancement in the stability is observed when the bearings are operating on controlled hybrid mode.

Figure 5-3 and Figure 5-4 present the predicted rotor synchronous vibration (bode plots) with an in-phase imbalance mass and an out-phase imbalance mass respectively. For both in-phase and out-phase imbalance masses, the maximum speed of the rotor is increased significantly when the bearings are operating on the controlled hybrid mode. More interestingly, the amplitude of vibration at the critical speed in the X-direction (gravitational direction) is reduced significantly for the controlled hybrid mode. However, the reduction in the amplitude of vibration at the critical speed in Y-direction is not significant. Since the X-direction is the loading direction, the amplitude of vibration at critical speed is larger in the X-direction compare to the Y-direction. For the case with the out-phase imbalance mass (Figure 5-4), the amplitude of vibration at the critical speed is higher than the case with the in-phase imbalance mass. Also, the onset speed of instability is observed to be lower for the case with the out-phase imbalance mass.

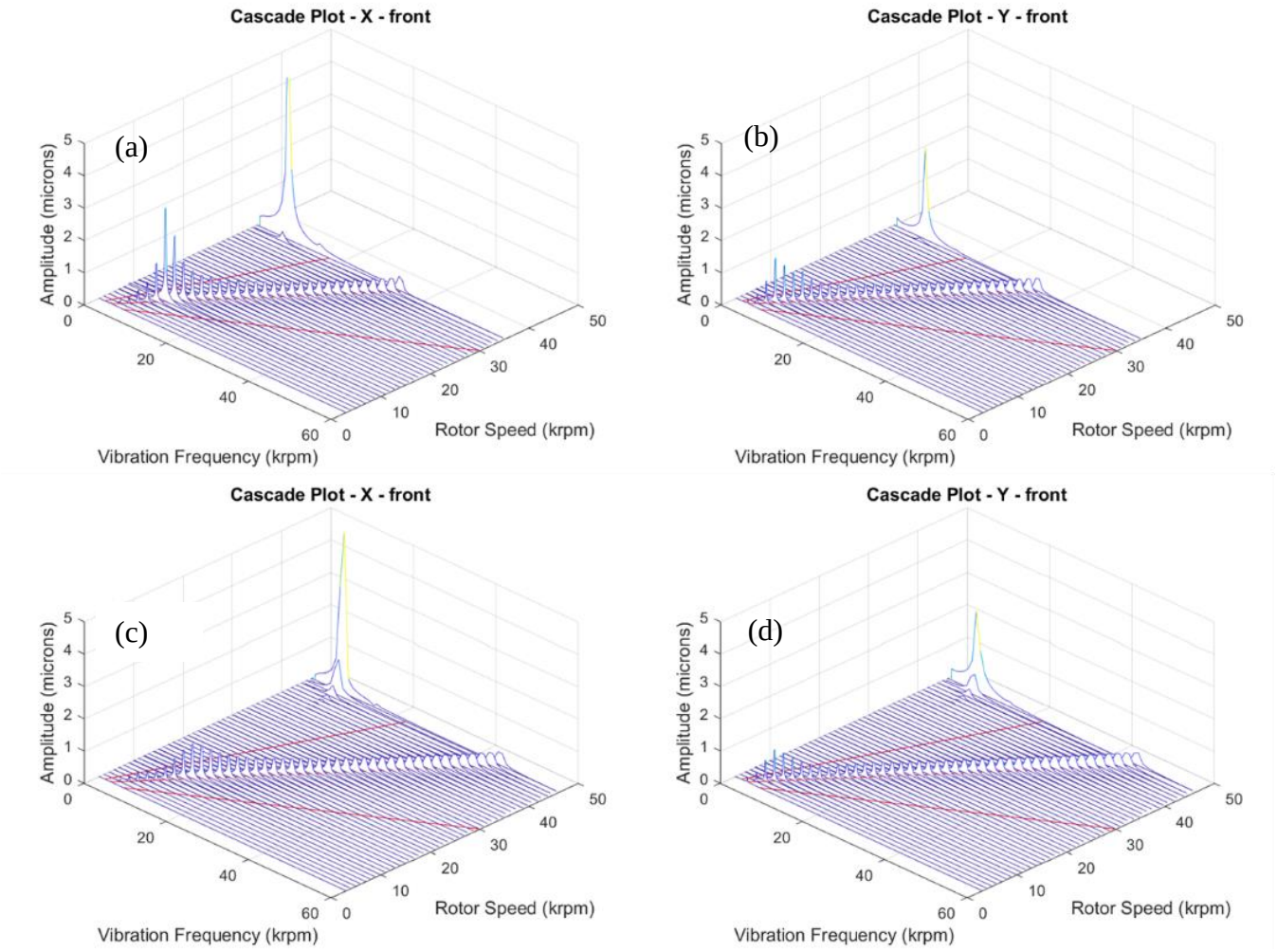

Figure 5-2 Simulated waterfall plots for Case-1 HAFB (a) full hybrid operation X-direction (b) full hybrid operation Y-direction (c) controlled hybrid operation X-direction (d) controlled hybrid operation Y-direction

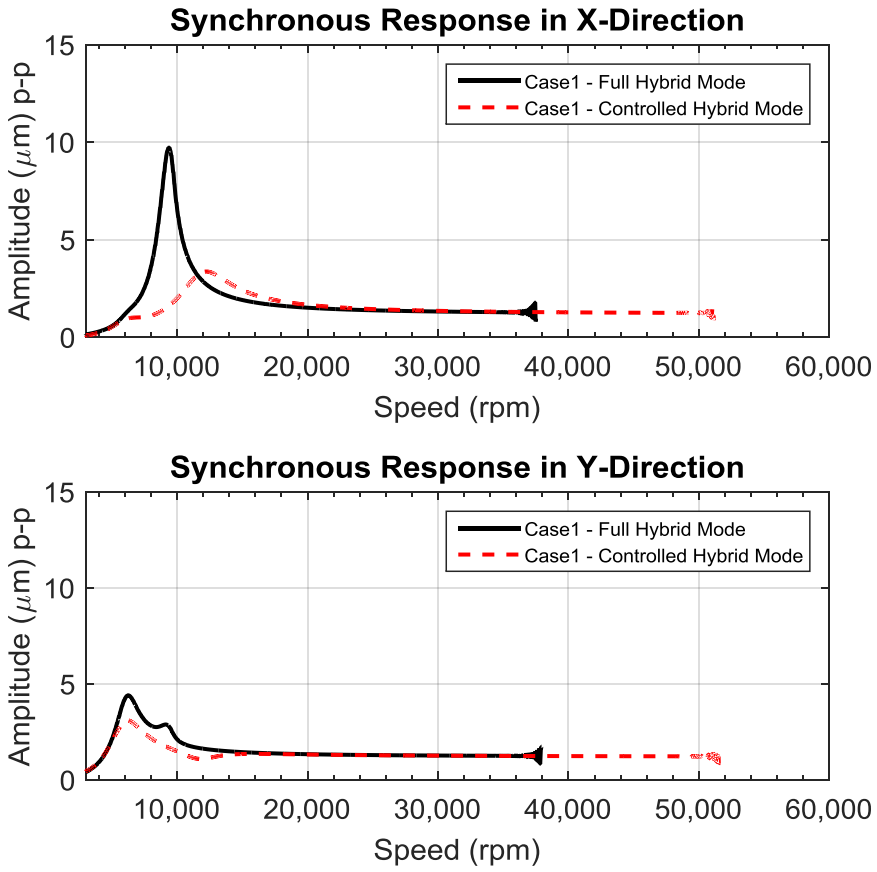

Figure 5-3 Predicted synchronous peak-to-peak vibration with the in-phase imbalance mass

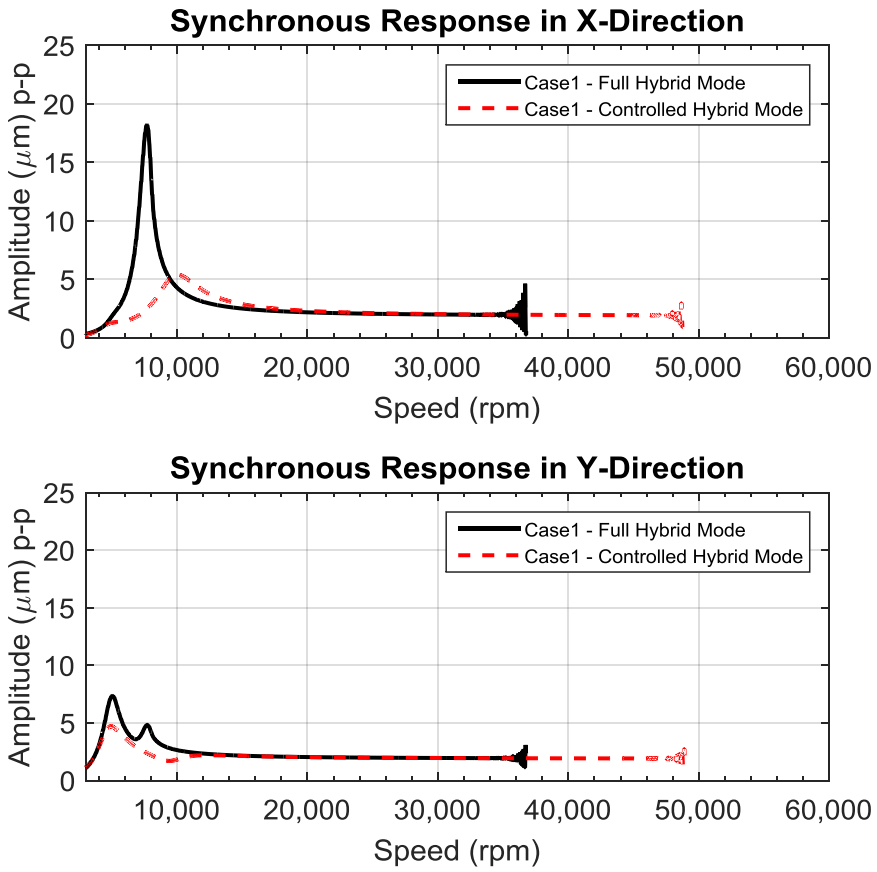

Figure 5-4 Predicted synchronous peak-to-peak vibration with the out-phase imbalance mass

5. 1. 2 Case-2: Hydrostatic injection at 60, 180, and 300 degree

The case 2 HAFB is illustrated in Figure 5-5. The angular location of orifices for case-2 HAFB is 60, 180 and 300 degree.

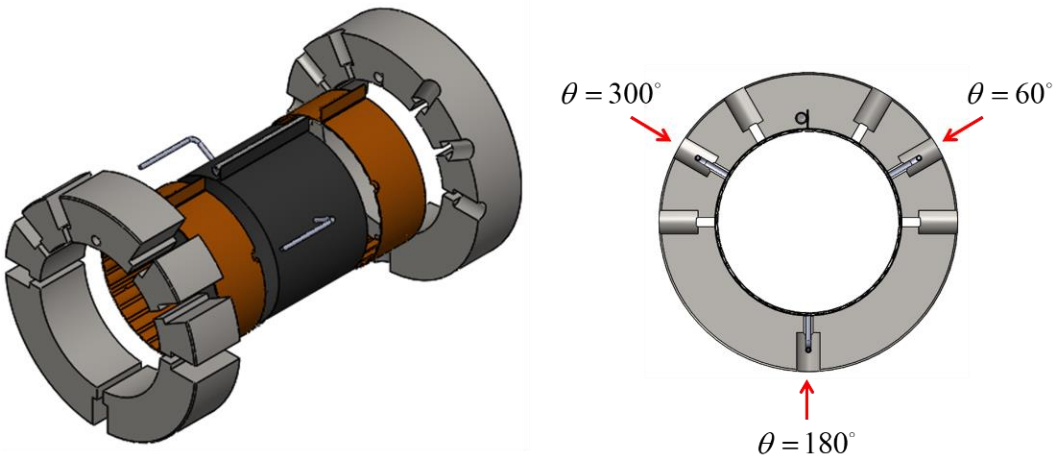

Figure 5-5 Front-view and isometric-view of case-2 single pad HAFB

Figure 5-6 presents the waterfall plots of case-2 HAFB for the full hybrid operation and the controlled hybrid operation. The onset speed of instability for the full hybrid operation is around 28,000 rpm, and bounded subsynchronous vibration is observed up to 34,000 rpm. Onset speed of instability for the controlled hybrid operation is around 31,000 rpm with bounded subsynchronous vibration up to 34,000 rpm. It is observed that the improvement in rotor-HAFB stability for case-2 HAFB when the bearings are operating on controlled hybrid mode is not as significant as case-1 HAFB.

The predicted synchronous imbalance responses for case-2 HAFB are presented in Figure 5-7 (in-phase imbalance mass) and Figure 5-8 (out-phase imbalance mass). Similar to case-1 HAFB, a significant reduction in the amplitude of vibration at critical speed in the X-direction is observed when the bearings are operating under the controlled hybrid mode. However, the critical speed is slightly shifted to a higher speed for the controlled hybrid operation.

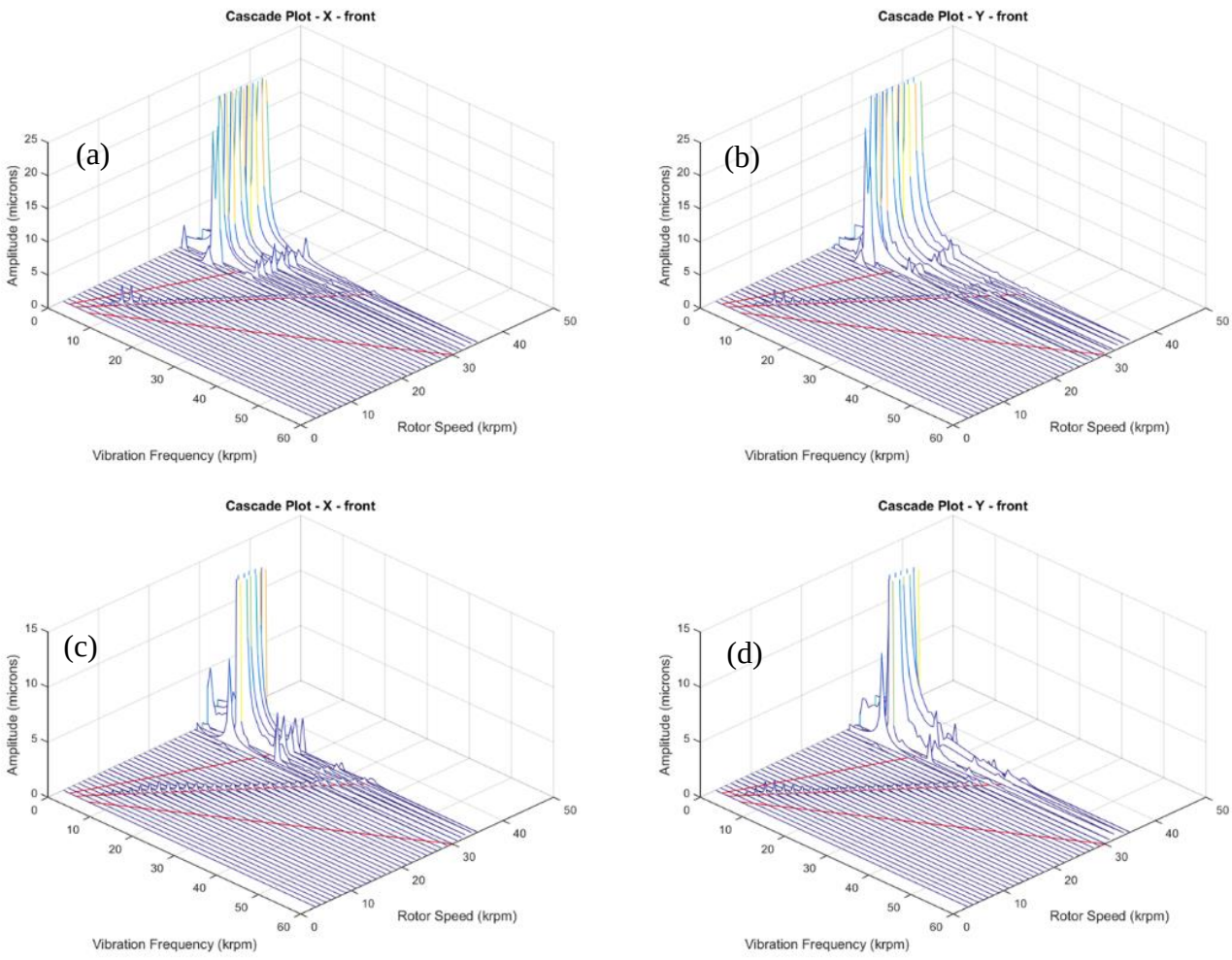

Figure 5-6 Simulated waterfall plots for Case-2 HAFB (a) full hybrid operation X-direction (b) full hybrid operation Y-direction (c) controlled hybrid operation X-direction (d) controlled hybrid operation Y-direction

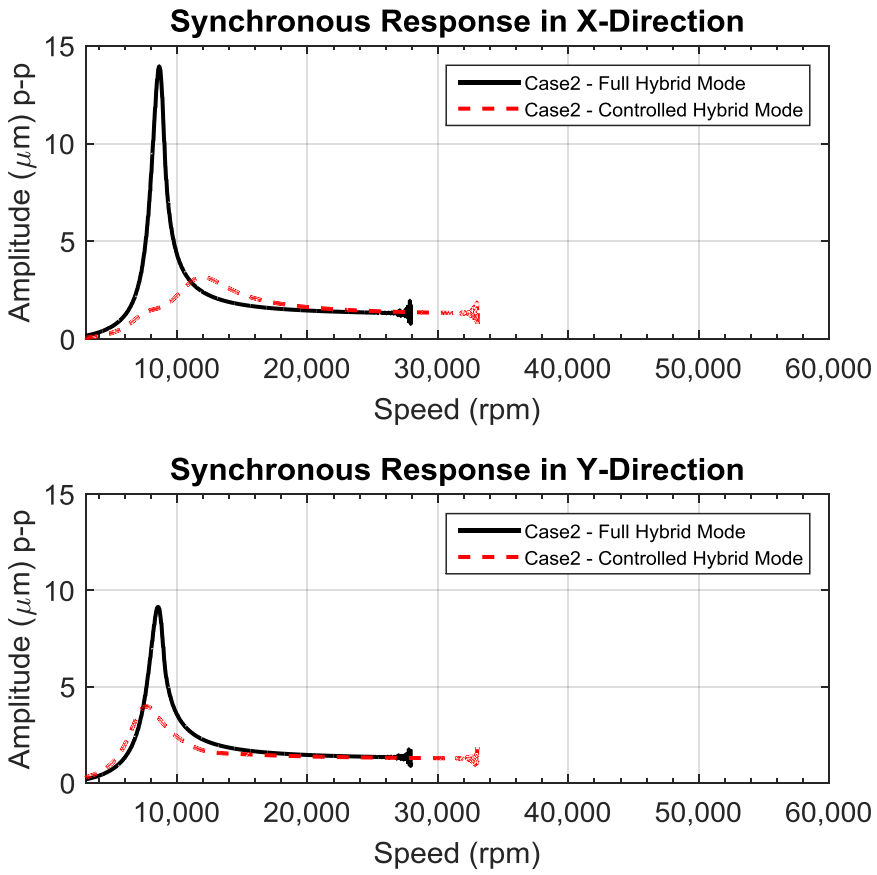

Figure 5-7 Predicted synchronous peak-to-peak vibration with the in-phase imbalance mass

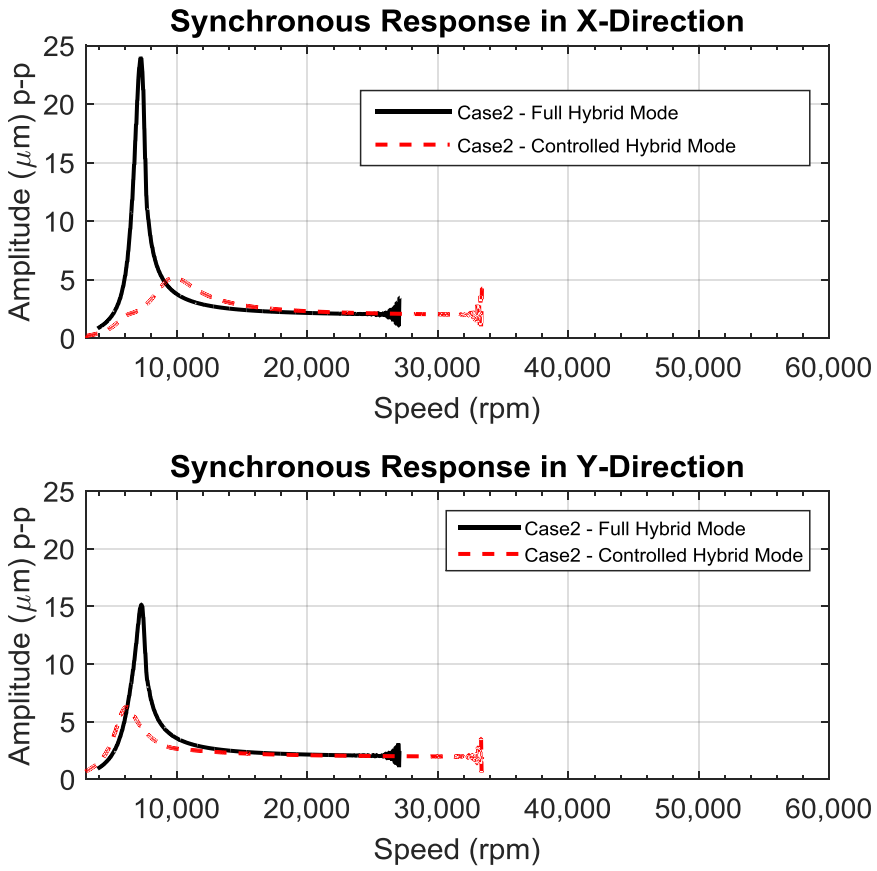

Figure 5-8 Predicted synchronous peak-to-peak vibration with the out-phase imbalance mass

5. 1. 3 Case-3: Hydrostatic injection at 90, 180, and 270 degree

Figure 5-9 presents the orifice configuration of case-3 HAFB. For case-3 HAFB, orifices are located at 90, 180 and 270 degree.

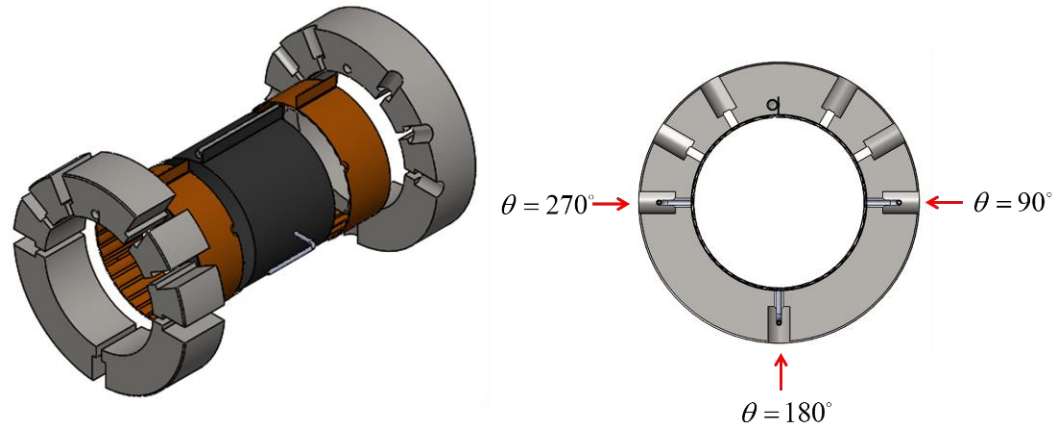

Figure 5-9 Front-view and isometric-view of case-3 single-pad HAFB

Predicted waterfall plots for the full hybrid operation and the controlled hybrid operation are presented in Figure 5-10. For the full hybrid operation, the onset speed of instability is observed to be around 34,000 rpm. The onset speed of instability for controlled hybrid mode is around 32,000 rpm. These results show that the controlled hybrid operation of case-3 HAFB reduces the onset speed of instability.

The predicted synchronous responses for the in-phase and the out-phase imbalance masse are presented in Figure 5-11 and Figure 5-12. For both in-phase and out-phase imbalance masses the maximum speed of the rotor is higher when the bearings are operating on the full hybrid mode. In comparison to the case-1 and case-2, the controlled hybrid operation of case-3 HAFB does not provide improvement for the rotordynamic performance.

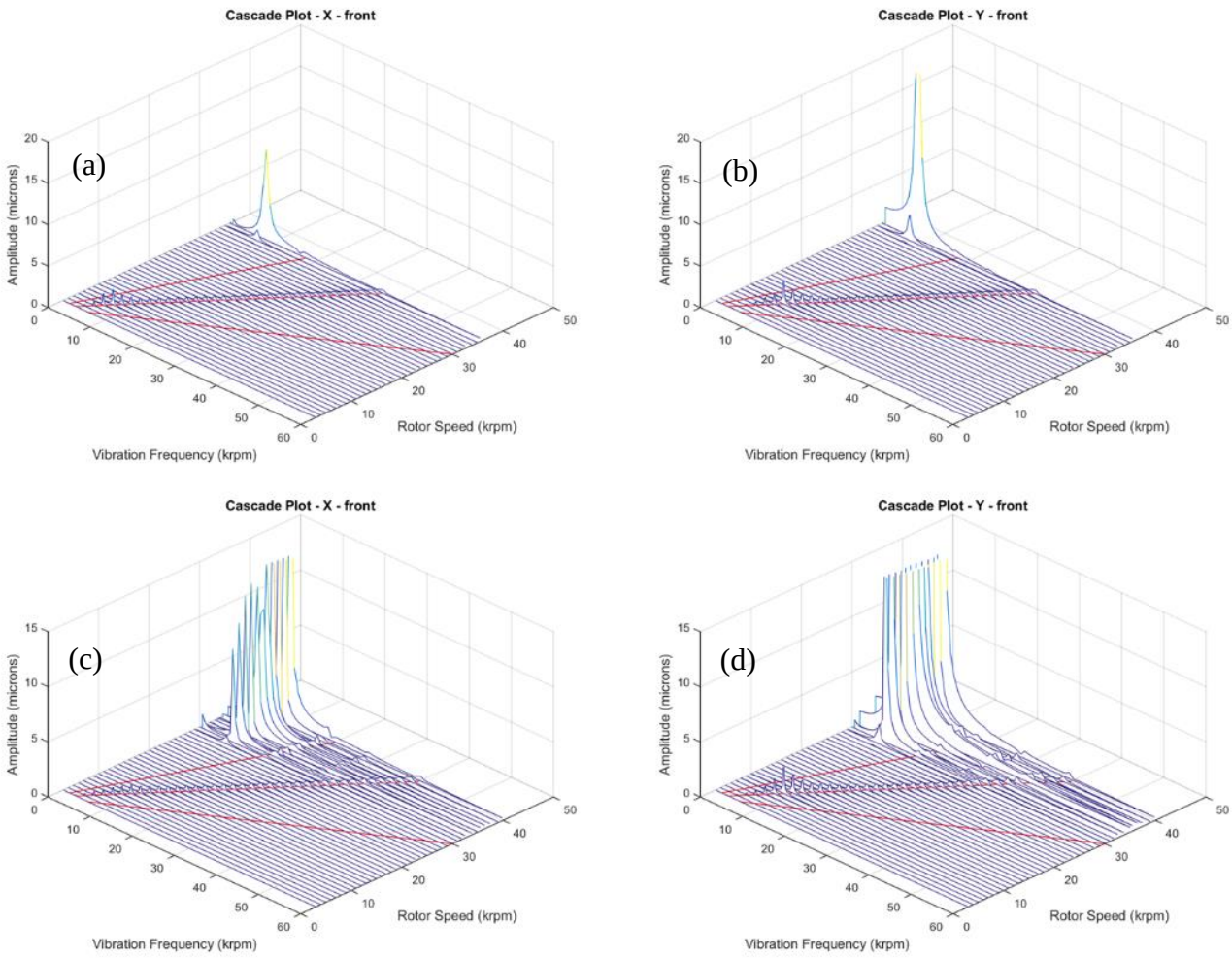

Figure 5-10 Simulated waterfall plots for Case-3 HAFB (a) full hybrid operation X-direction (b) full hybrid operation Y-direction (c) controlled hybrid operation X-direction (d) controlled hybrid operation Y-direction

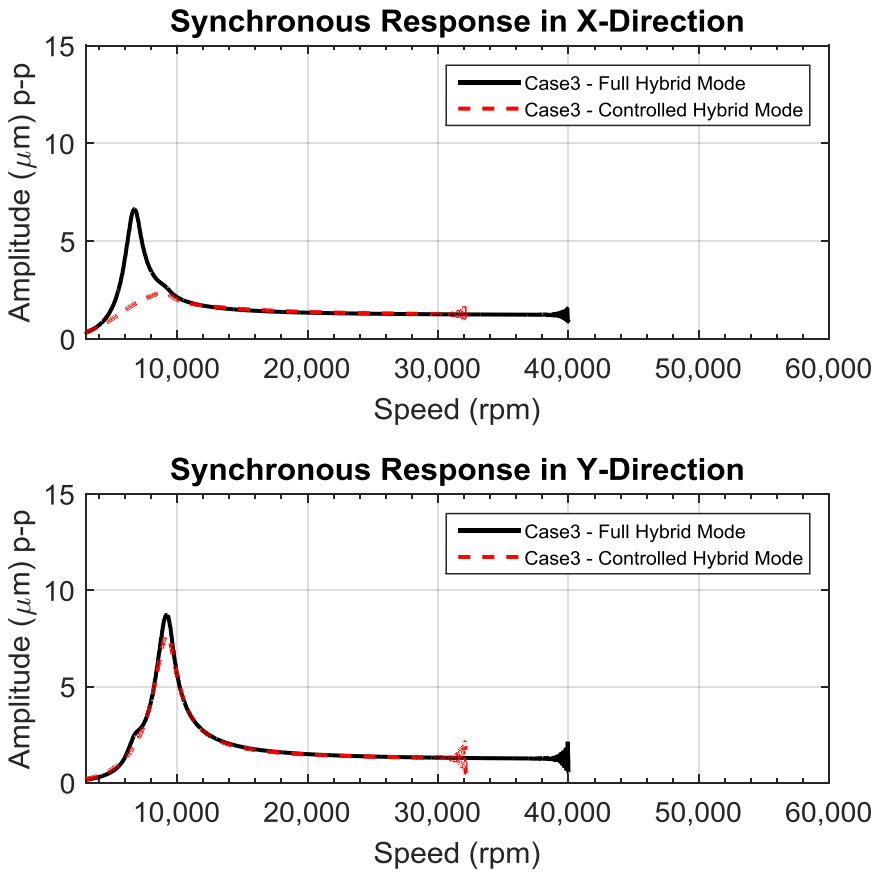

Figure 5-11 Predicted synchronous peak-to-peak vibration with the in-phase imbalance mass

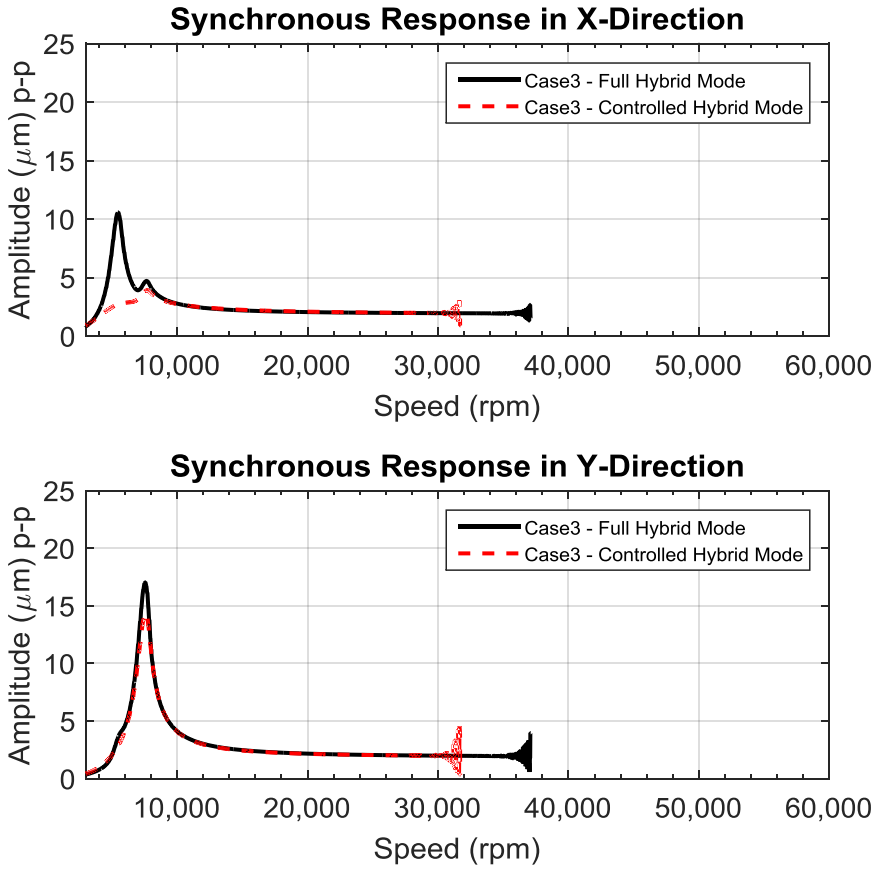

Figure 5-12 Predicted synchronous peak-to-peak vibration with the in-phase imbalance mass

5. 1. 4 Rotordynamic performance comparison of three different cases

The synchronous imbalance responses of all three cases are plotted in Figure 5-13. The highest onset speed of instability is achieved when the case-1 HAFB is operating on the controlled hybrid mode. The amplitude of vibration at the critical speed is lower for the case-3 HAFB compare to the two other cases. The amplitude of vibration at the critical speed for case-2 HAFB is higher than the case-1 HAFB, when the bearings are operating on the full hybrid mode. However, for the controlled hybrid operation, the

vibration amplitude at the critical speed for the case-1 HAFB and the case-2 HAFB is almost identical.

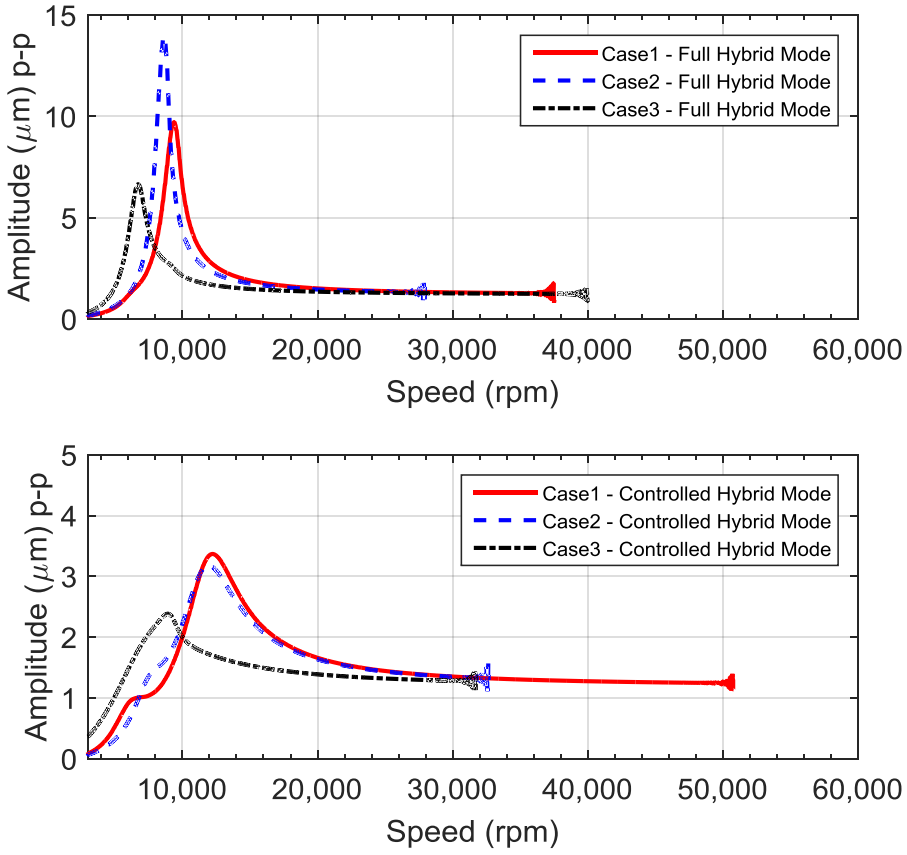

Figure 5-13 Comparison of predicted synchronous peak-to-peak vibration with the in-phase imbalance mass

The predicted rotor eccentricity and attitude angle versus rotor's speed for the full hybrid operation is presented in Figure 5-14. For the full hybrid operation, the case-1 HAFB has the highest rotor eccentricity and the lowest attitude angle.

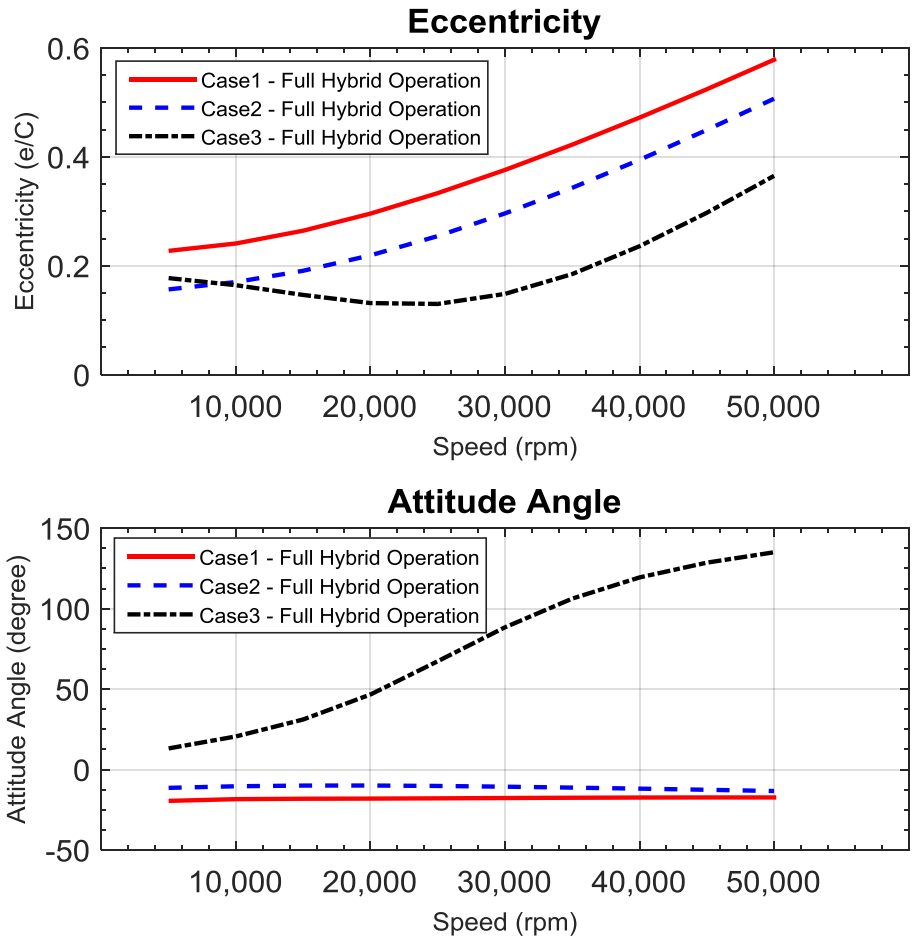

Figure 5-14 Predicted rotor eccentricity and attitude angle for full hybrid operation

Figure 5-15 presents the rotor eccentricity and attitude angle for all three cases when the bearing are operating on the controlled hybrid mode. Case-1 HAFB has the highest rotor eccentricity but the attitude angle of the case-1 HAFB is not the lowest.

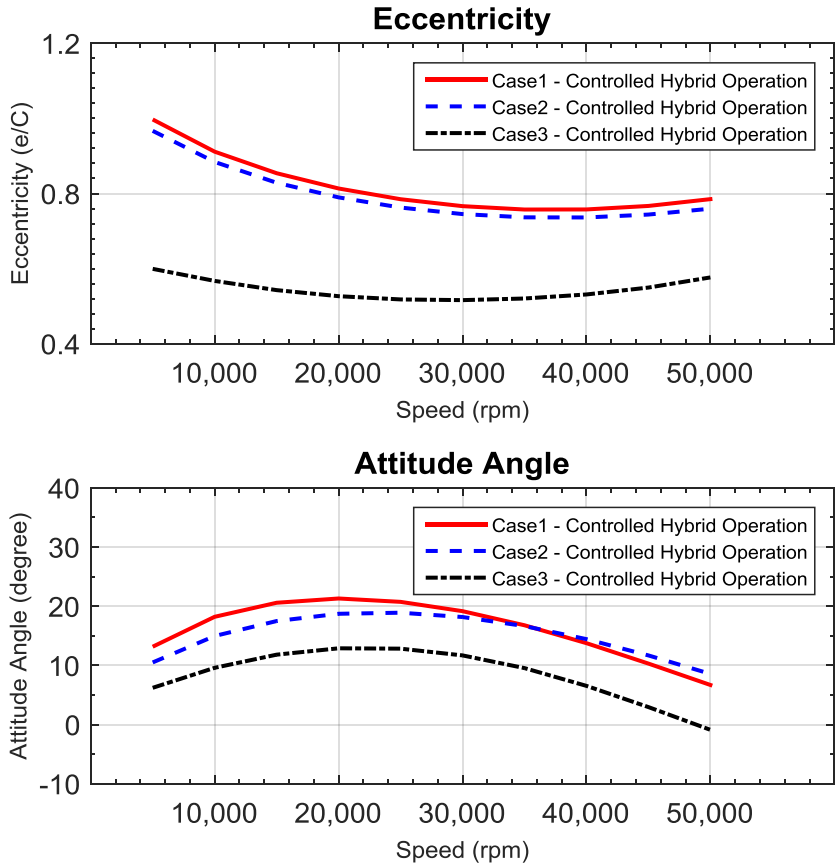

Figure 5-15 Predicted rotor eccentricity and attitude angle for controlled hybrid operation

5. 2. Modal analysis

Figure 5-16 presents the modal stiffness and the modal damping for the forward whirl at 35,000 rpm for the full hybrid operation. Imbalance response plots for the full hybrid operation (in the previous section) showed that the case-1 HAFB and the case-3 HAFB are stable at 35,000 rpm, whereas case-2 HAFB is not stable. From modal damping plot for full hybrid operation (Figure 5-16), it is observed that both case-1 HAFB and case-3 HAFB have a positive damping for the small excitation frequency ratios ($\nu < 0.35$ or $\omega_s = 204.167\,Hz$), but case-2 HAFB has a negative damping, therefore case-2 HAFB is not stable if the rotor is excited by vibrations with small frequencies.

Moreover, case-1 HAFB has the highest modal damping for the entire excitation frequency ratio compare to the two other cases. From modal stiffness plot for the full hybrid operation (Figure 5-16), it is observed that both case-1 HAFB and case-3 HAFB have much higher stiffness compare to the case-2 HAFB.

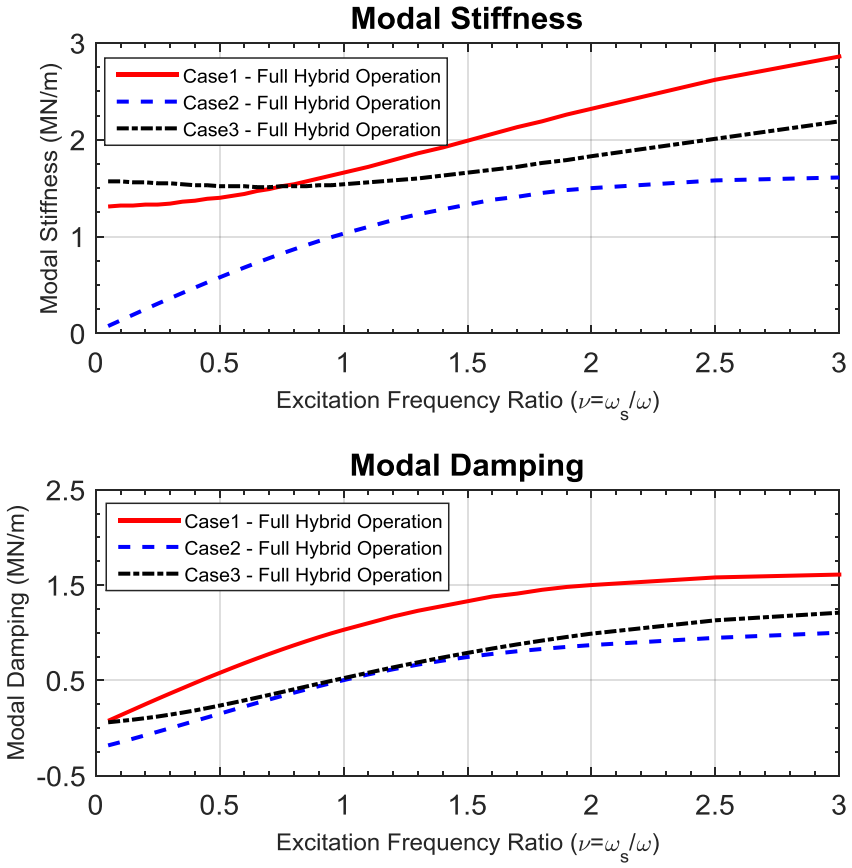

Figure 5-16 Modal impedances for the forward whirl versus the excitation frequency ratio for the full hybrid operation at 35,000 rpm

Modal stiffness and modal damping for the forward whirl at 40,000 rpm for controlled hybrid operation are presented in Figure 5-17. From imbalance response plots for the controlled hybrid operation at 40,000 rpm, it is observed that only case-1 HAFB is stable at 40,000 rpm. The modal damping plot shows that the case-1 HAFB has a

positive damping at low excitation frequency ratios whereas case-2 HAFB and case-3 HAFB have a negative modal damping. These results indicate that case-2 HAFB and case-3 HAFB are not stable at 40,000 rpm if vibrations with low frequency ratios excite the rotor. Modal stiffness plot for the controlled hybrid operation at 40,000 rpm shows that the case-2 HAFB has a lower stiffness compares to the case-1 HAFB and case-3 HAFB. In general, a higher stability for case-1 HAFB compares to the other configurations is a result of a higher modal stiffness and damping and a positive modal damping for the entire excitation frequency ratio.

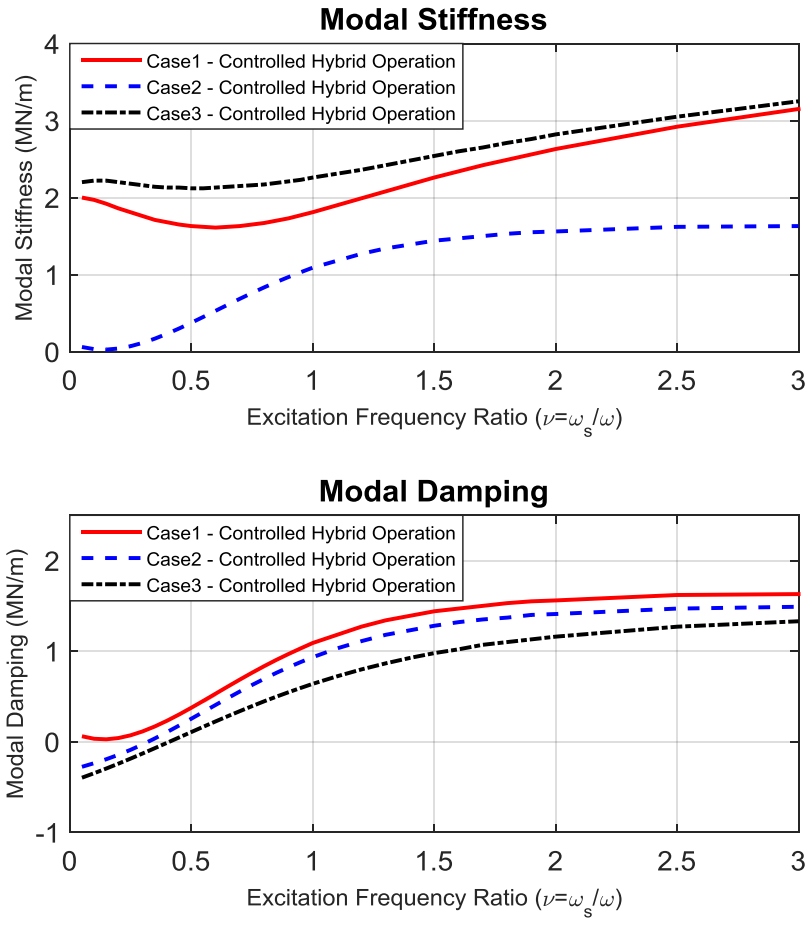

Figure 5-17 Modal impedances for the forward whirl versus the excitation frequency ratio for controlled hybrid operation at 40,000 rpm

5. 3. Rotor-HAFB imbalance response measurement and comparison to the prediction

In order to validate the prediction results presented in the previous section, the rotordynamic performance of the single-pad HAFBs with different orifice configuration is evaluated using a high-speed rotordynamic test rig. The details of the rotor, measuring instruments, and the high-speed rotordynamic test rig were presented in the chapter 3.

For experimental analysis, two sets of single-pad HAFBs are manufactured. The first set has orifice configuration similar to the case-1 HAFB, and the second set has orifice configuration of case-2 HAFB. Figure 5-18 shows the single-pad HAFB which is used for experimental analysis. The bearing sleeve had several openings which accommodate using it for different orifice configurations. One axial slot is EDMed in to the bearing sleeve for assembling the top foils and bump foils. A stainless steel assembly pin is used to hold the foils inside the slot.

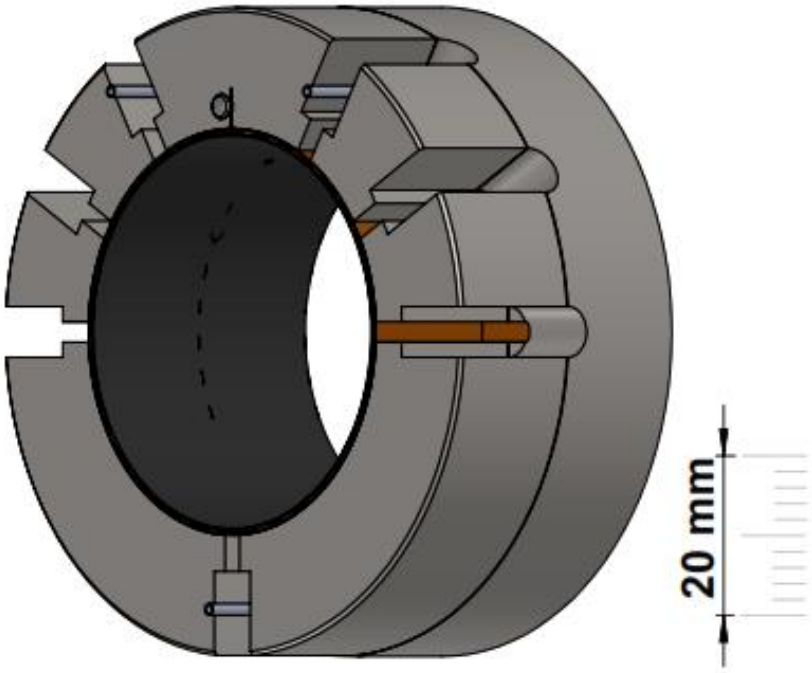

Figure 5-18 Schematic-view of case-1 single-pad HAFB

The top foil for case-1 single pad HAFB is shown in Figure 5-19. Three stainless steel orifice tubes are laser welded to the top foil. To access the orifice tubes from outside of the test rig housing, plastic extension tubes are attached to the stainless steel orifice tubes. Figure 5-20 shows the bump foil for the case-1 single pad HAFB. For the assembly propose the bump foils are split into two stripes. As it is mentioned in the chapter 3, the bump foil tooling is only capable of making bump foil stripes with11 bumps. Since the single pad HAFB has 33 bumps, three bump foil stripes are spot welded on a back plate foil (Inconel 750 and 0.127 mm thickness) to form a single bump foil stripe with 33 bumps.

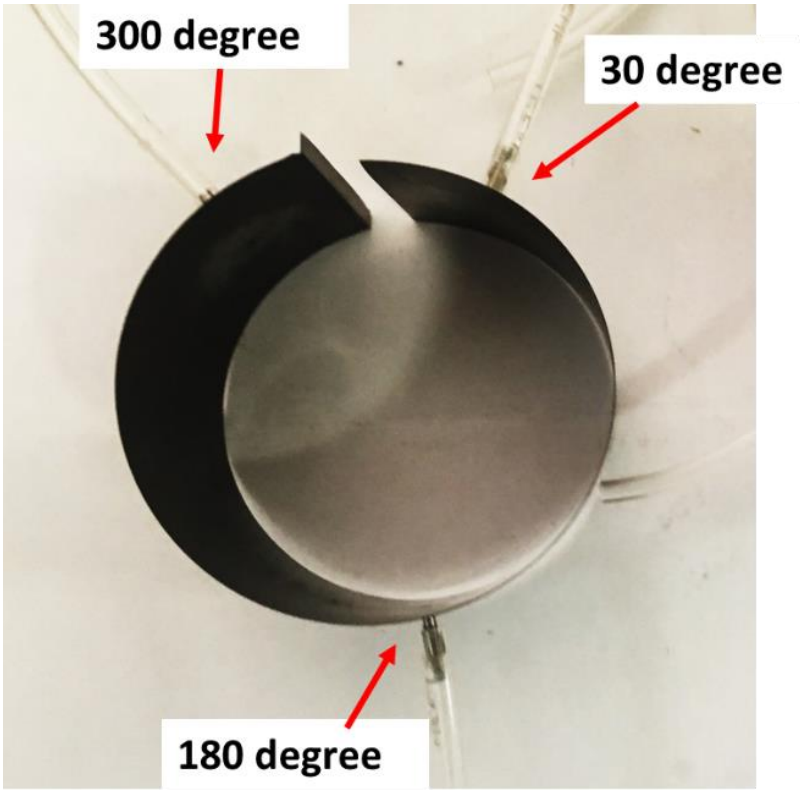

Figure 5-19 Circular top foil for case-1 single pad HAFB

Figure 5-20 Split type bump foil stipes for case-1 single pad HAFB

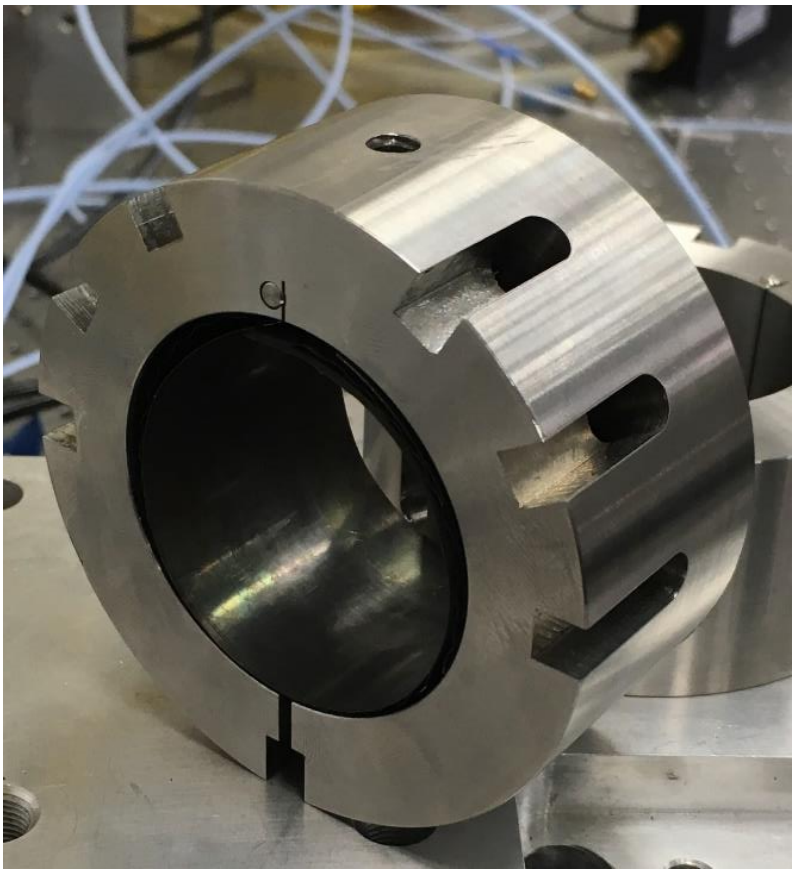

Figure 5-21 Single pad HAFB

Since the prediction results showed that the case-3 HAFB does not provide any rotordynamic enhancement, the performance of case-3 HAFB is not evaluated in the experimental investigation. During each experiment test, the initial startup is performed with HAFBs operating on the full hybrid mode. The rotor imbalance response is measured during speed up with the full hybrid mode until the subsynchronous vibrations start to appear. After observing the subsynchronous vibration, rotor speed is reduced to the point where the subsynchronous vibration is disappeared, then the bottom orifice is closed and the rotor speed is increased while the bearings are operating on the controlled hybrid mode.

Figure 5-22 presents the measured waterfall plot of case-1 HAFB operating on the full hybrid mode. The critical speed is around 12,000 rpm. The rotor is stable up to 40,000 rpm and around 40,200 rpm a small subsynchronous vibration starts to appear. Figure 5-23 shows the measured waterfall plot of case-1 HAFB operating on the controlled hybrid mode. Rotor is stable up to 53,000 rpm, and a subsynchronous vibration with a small magnitude appears at speeds higher than 53,000 rpm. This result confirms the prediction results and shows a significant improvement in rotor-HAFB performance with controlled hybrid operation of case-1 HAFB. Figure 5-24 shows the measured imbalance response of case-1 HAFB at 42,000 rpm for both full hybrid operation and the controlled hybrid operation. The vibration magnitude for 1X component is identical for both full hybrid and controlled hybrid operation. A subsynchronous vibration with the magnitude of 2.25 microns is observed for the full hybrid operation whereas the controlled hybrid operation does not show any subsynchronous vibration.

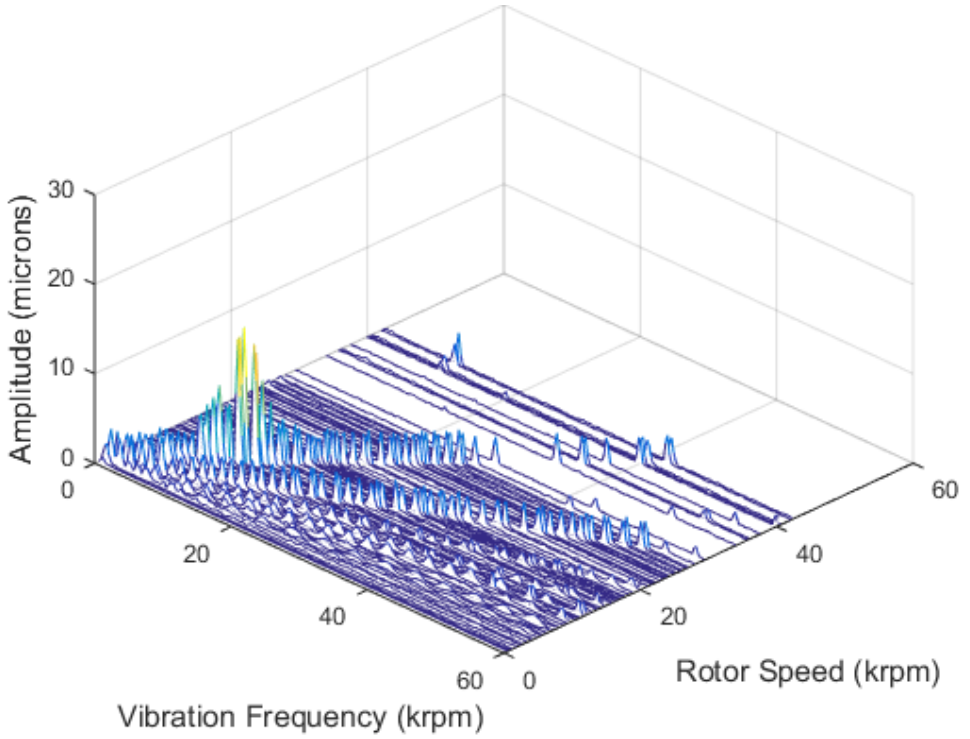

Figure 5-22 Measured imbalance response in X-direction for Case-1 HAFB (full hybrid operation)

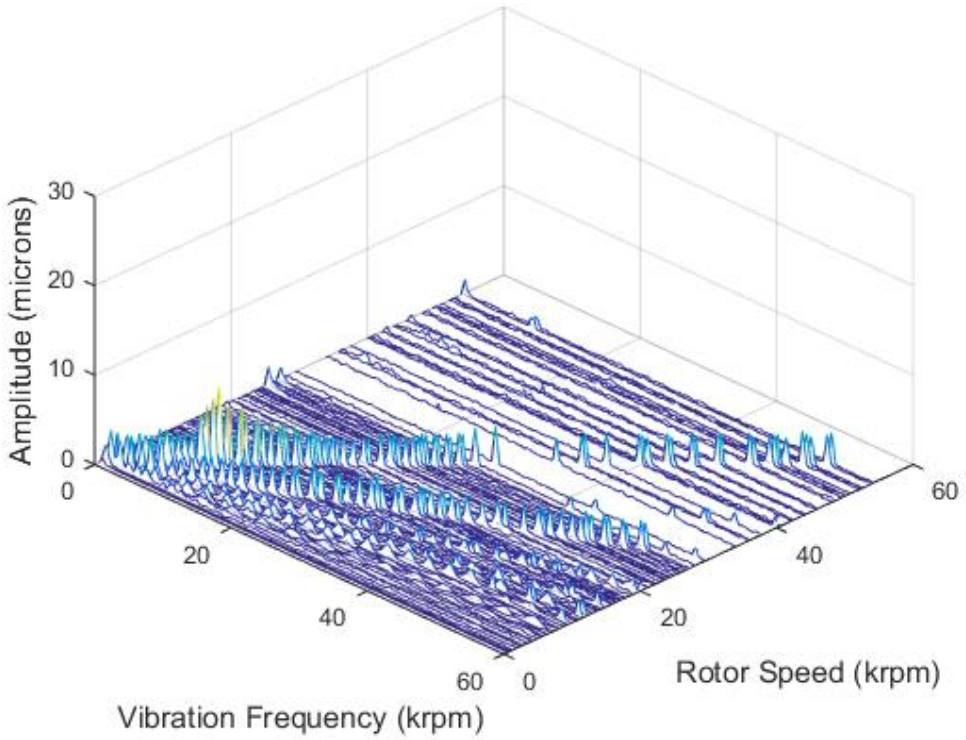

Figure 5-23 Measured imbalance response in X-direction for Case-1 HAFB (controlled hybrid operation)

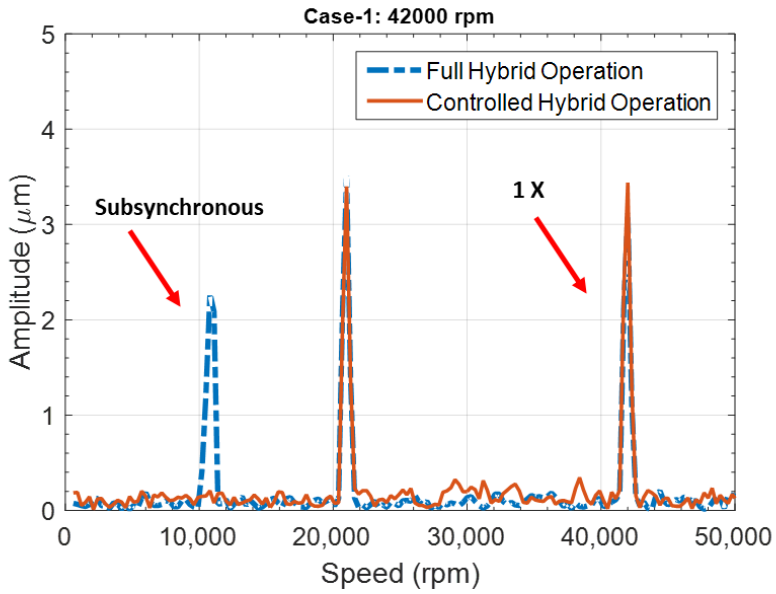

Figure 5-24 Measured imbalance response of case-1 HAFB for full hybrid operation and controlled hybrid operation at 42,000 rpm

Figure 5-25 shows the waterfall plot for the full hybrid operation of case-2 HAFB. Subsynchronous vibration is observed around 28,000 rpm and the magnitude of subsynchronous vibration increases slowly as the rotor's speed increases. Figure 5-26 presents the measured imbalance response of case-2 HAFB operating on the controlled hybrid mode. It is observed that the onset speed of subsynchronous vibration is delayed when the bearings are operating on controlled hybrid mode. Measured imbalance response of the rotor with case-2 HAFB for both full hybrid and controlled hybrid operations at 29,700 rpm is shown in Figure 5-27. For the full hybrid operation, a subsynchronous vibration with the magnitude of 3.2 microns is observed but the subsynchronous vibration is disappeared when the bearings operating on the controlled hybrid mode.

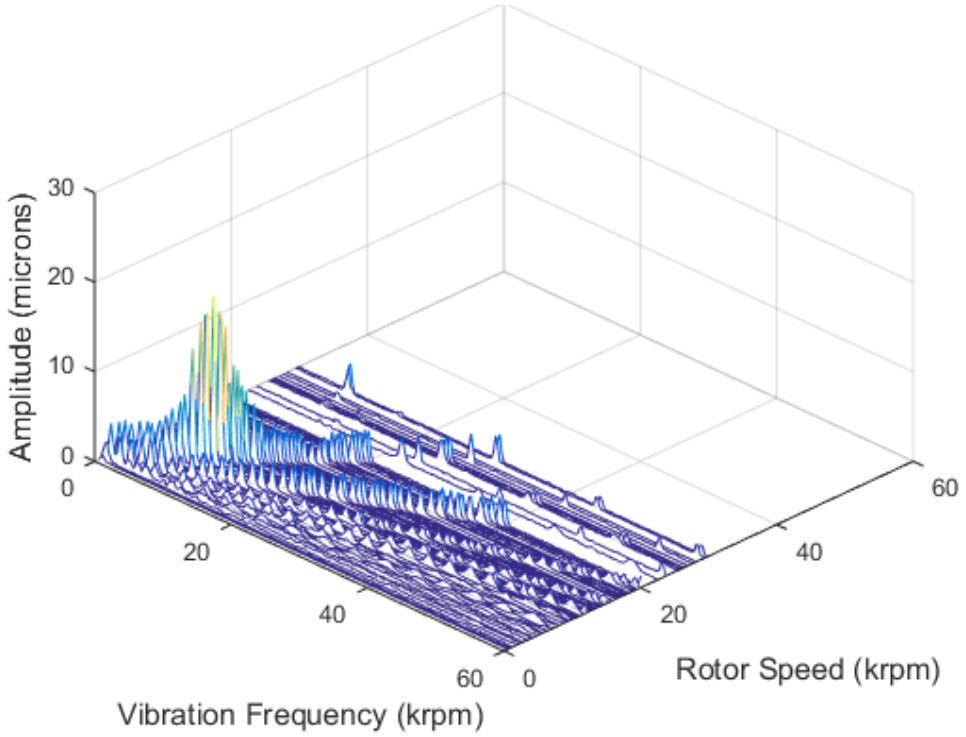

Figure 5-25 Measured imbalance response in X-direction for Case-2 HAFB (full hybrid operation)

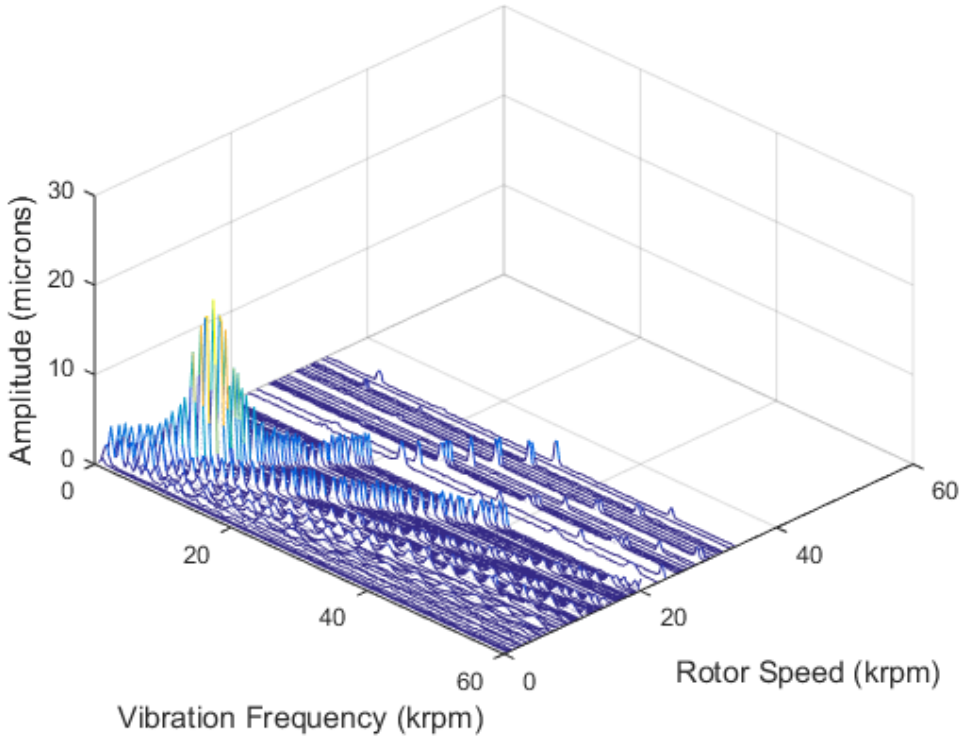

Figure 5-26 Measured imbalance response in X-direction for Case-2 HAFB (controlled hybrid operation)

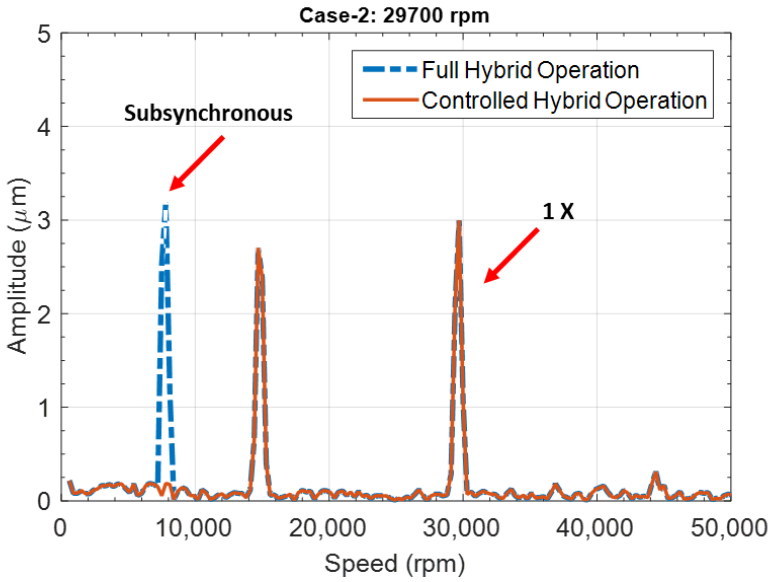

Figure 5-27 Measured imbalance response of case-2 HAFB for full hybrid operation and controlled hybrid operation at 29,700 rpm

Figure 5-28 (a) shows the measured synchronous imbalance response of case-1 HAFB and case-2 HAFB for the controlled hybrid operation. Significant improvement in the rotor-HAFB stability is observed for case-1 HAFB. The maximum speed of the rotor increases from 30,000 rpm to 54,000 rpm. During the experiment, both case-1 HAFB and case-2 HAFB are operating on the full hybrid mode while passing the critical speed. It is observed that the amplitude of vibration at the critical speed is lower for case-1 HAFB; however, the critical speed is slightly shifted to a higher speed. The predicted peak-peak imbalance response is in agreement with the measured data.

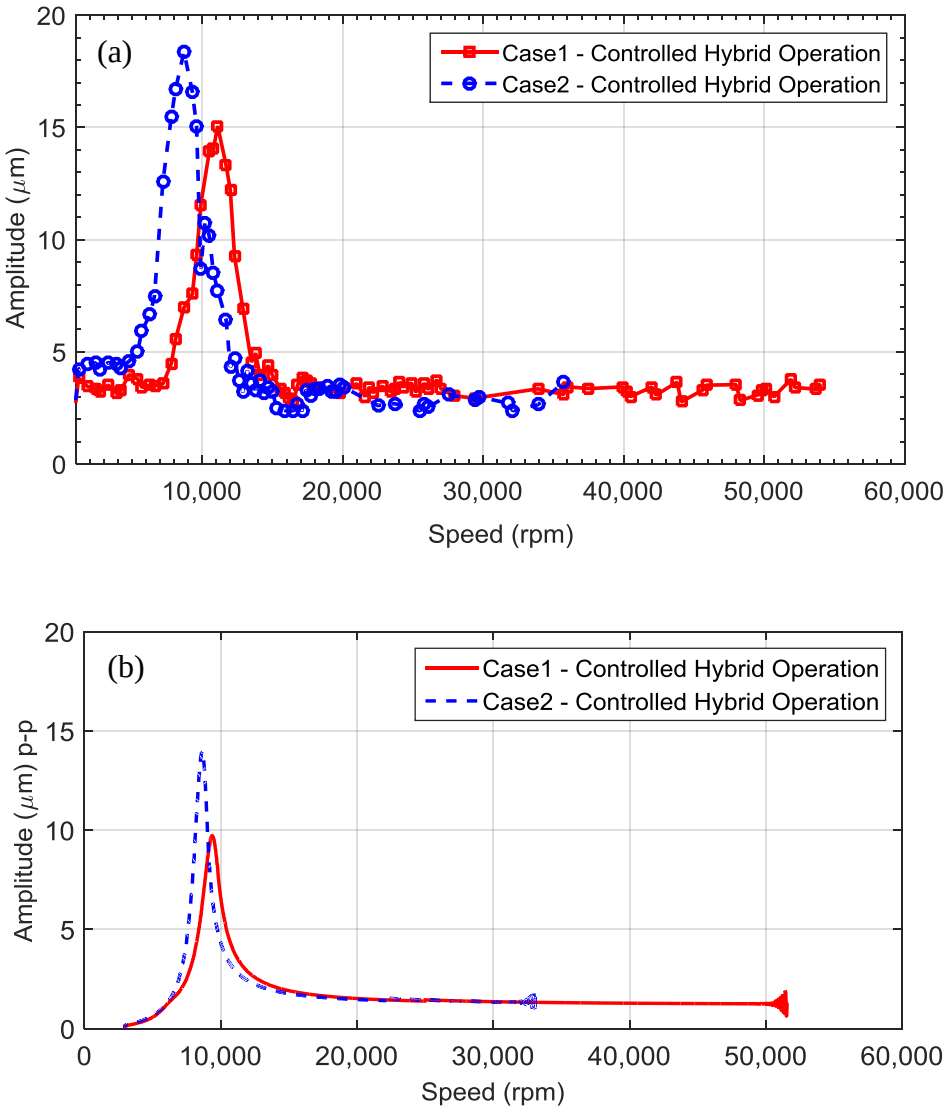

Figure 5-28 Peak-peak imbalance response for controlled hybrid operation (a) measured imbalance response (b) predicted imbalance response

Chapter 6

SUMMARY AND CONCLUSIONS

Hybrid air foil bearings (HAFBs) utilize the radial injection of externally pressurized air into the radial clearance of the traditional hydrodynamic AFBs. HAFB has a negligible friction torque during start/stop compare to pure hydrodynamic air foil bearing. HAFB provides solution for the thermal management through injection of externally pressurized air in to bearing compartment. Also, HAFB has the ability to carry load at zero speed, whereas the hydrodynamic AFB has zero load capacity when the rotor is stationary.

This dissertation investigates the rotordynamic enhancement by utilizing the controlled hydrostatic injection of HAFBs. The rotordynamic performance of a rotor-HAFB under different operating modes (pure hydrodynamic operation, full hybrid operation, and controlled hybrid operation), and with different orifice configuration (orifices at different circumferential locations) is evaluated both numerically and experimentally. The numerical analyses consist of the time-domain orbit simulation and frequency-domain modal analysis. For the experimental analysis, the imbalance response of the rotor-HAFB is measured using a high speed rotordynamic test rig.

Comparison between the predicted imbalance responses show that the onset speed of subsynchronous vibration is delayed and the maximum speed of the rotor is extended when HAFBs are operating on the controlled hybrid from 27,000 rpm to around 45,000 rpm, and the amplitude of the synchronous vibration at the critical speed is reduced significantly. The beneficial effect of the controlled hybrid mode was also confirmed experimentally. The predictions agree with experiments in general tendency, i.e., controlled hybrid mode eliminates the subsynchronous vibrations in both experiments and simulations. However, predicted subsynchronous vibrations are much larger than

measured values. The limitation of the current simple equivalent viscous damping model (adopted for orbit simulations) using the synchronous excitation frequency was identified as one of the possible reasons for the discrepancy. Another possible reason for the discrepancy is feasibility of much more damping from the foil structure than that predicted from loss factor of 0.2, which might steam from more complicated bump dynamics. Eccentricity and attitude angles were compared for hydrodynamic, full hybrid and controlled hybrid modes. In general, a combination of large eccentricity and small attitude angle promotes the stability but more general stability characteristics can be investigated using the frequency-domain modal analyses. The modal impedance curves of the controlled hybrid mode for both cylindrical and conical modes show that the modal damping becomes positive for entire excitation frequencies confirming the experimental observation as well as time-domain orbit simulations.

The effect of the circumferential location of the radial hydrostatic injection on the rotordynamic performance of HAFBs is also investigated. Comparison of the rotordynamic performances of three sets (cases) of single-pad HAFBs with different circumferential locations of hydrostatic injection is conducted numerically and experimentally. Case-1 HAFB has orifices at $\theta = 30^{\circ}, 180^{\circ}, 300^{\circ}$, case-2 HAFB orifices are located at $\theta = 60^{\circ}, 180^{\circ}, 300^{\circ}$, and for case-3 HAFB the circumferential position of orifices is $\theta = 90^{\circ}, 180^{\circ}, 270^{\circ}$.

The rotordynamic performance for each case is evaluated for full hybrid operation and controlled hybrid operation. In general, the controlled hybrid operation provides a better rotordynamic stability, except for case-3 which doesn't show any improvement in stability when operating on the controlled hybrid mode. The imbalance response prediction from the orbit simulation shows that the case-1 HAFB has the

highest rotordynamic stability, while the case-3 HAFB results in the lowest rotor-bearing stability. The predicted results are confirmed experimentally. Imbalance response measurements for the case-1 HAFB and case-2 HAFB show a better rotordynamic stability for the case-1 HAFB. Predicted rotor peak-peak synchronous responses show that the case-3 HAFB has the largest magnitude of critical speed and the lowest operating speed. Predicted rotor eccentricity and attitude angle show that the case-1 HAFB has the largest eccentricity and case-3 HAFB the lowest. Frequency domain modal analyses at 40,000 rpm show that the case-2 HAFB and case-3 HAFB have a negative modal damping for external excitations with frequency ratios smaller than 0.35 ($\nu < 0.35$). For the case-1 HAFB, the modal damping is positive for the entire excitation frequency ratio. In general, a combination of large rotor eccentricity and positive damping coefficient results in the highest rotordynamic stability and better performance for the case-1 HAFB. The frequency domain modal analyses are in agreement with the experimental analyses as well as orbit simulations.

APPENDIX A

LIFT-OFF SPEED TEST RIG AND LIFT-OFF SPEED MEASURMENT

Appendix-A presents the detail and description of the lift-off test, and the results from the lift-off speed measurement for HAFB. Generally, lift-off speed measurement can be used as a tool to evaluate the performance of HAFBs. Comparing the measured lift-off speed with the design values can be used as preliminary evaluation of a manufactured HAFB and to identify whether the manufacturing process is done properly or not. Figure A-1 shows the details and the layout of the lift-off test rig. The test rig is driven by a 15 KW electric motor. The rotor and the shaft are connected using a high-speed coupling. Two rolling element bearing, located inside the ball bearing housing, support the shaft radially. An overhanging test journal (49 mm diameter) is bolted to the shaft. The test bearing floats on the journal once the shaft starts spinning. The details and dimensions of the test journal are shown in Figure A-2. A static load is applied to the HAFB's housing in the vertically direction (to simulate the gravitational load on the bearing in the actual rotordynamic test). The axial location of the static load on the bearing housing is exactly at the center. A torque rod attached to the bearing housing in the horizontal direction prevents the bearing housing from rotation, and it is used to measure the HAFB drag torque during start/stop tests. The torque arm is connected to a pre-loaded load cell which measures the friction force between the HAFB surface (top foil) and the journal.

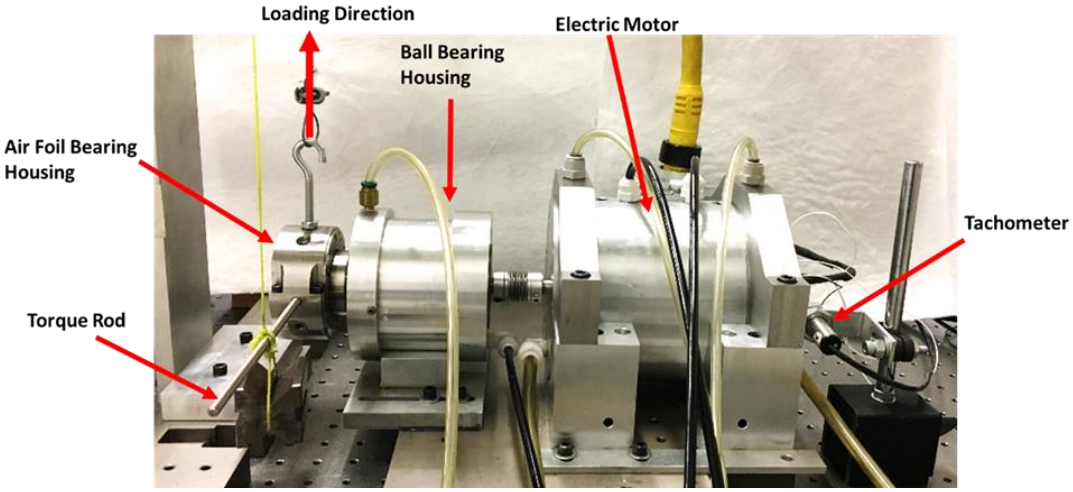

Figure A-1 Lift-off Test rig layout

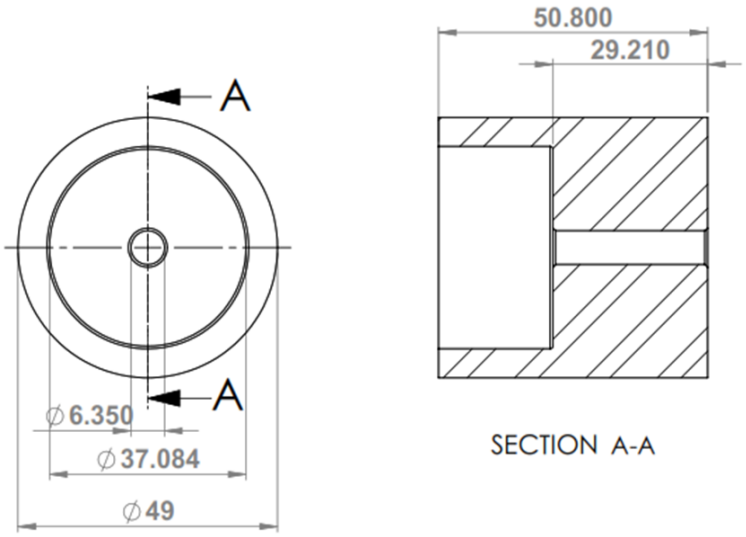

Figure A-2 Lift-off speed journal

As the journal starts to spinning, the bearing housing tends to rotate in the same direction as the journal. The dry sliding between the HAFB surface and the journal is due to the friction torque between the journal and the bearing surface (top foil). As the bearing housing starts to rotate, the torque rod rotates and the load on the load cell is reduced. As journal speed increases, the hydrodynamic pressure inside the bearing film increases until the bearing reaction force, due to the hydrodynamic pressure, balances the static load applied the bearing. At this moment, the bearing is fully lifted-off and the friction torque on the bearing surfaces reduces significantly. The bearing lift-off speed is identified by measuring the friction toque during the rotor start/stop.

Figure A-3 shows the measured friction torque for the case-1 single-pad HAFB during the rotor speed-up/coast-down under 22.226 N static load (equal to half of the rotor weight). The start/stop friction torque of the single-pad HAFB is almost same as the airborne friction torque. It is observed that the bearing is fully lifted-off because of the hydrostatic pressurization and the friction torque is minimum. This result indicates that the HAFB performs well and the manufacturing process has been done properly.

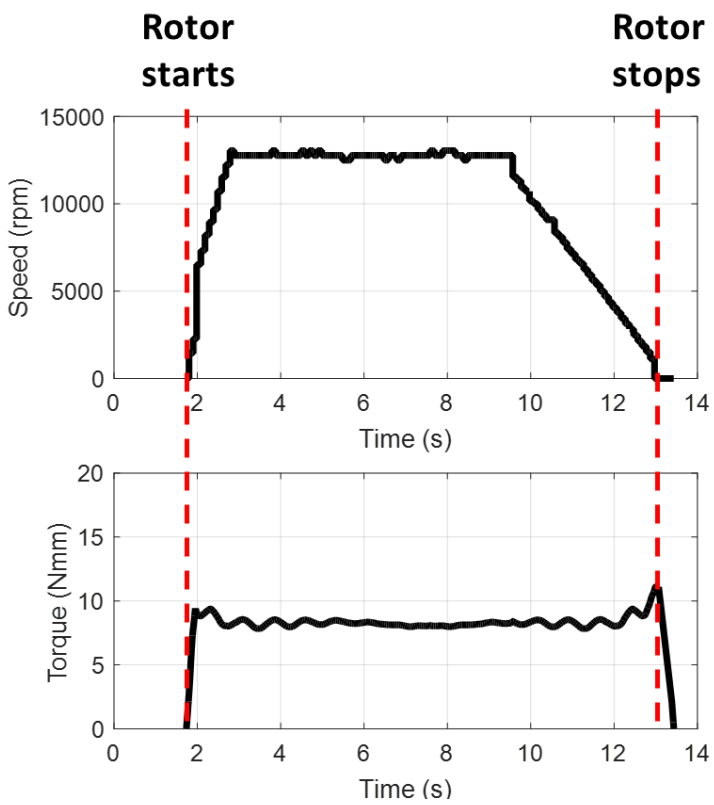

Figure A-3 Friction torque for case-1 single-pad HAFB under 22.226 N static load

APPENDIX B

LOAD-DEFLECTION TEST

The static load-deflection test is conducted to measure the bearing's radial clearance, bearing's static structural stiffness, and bearing's loss factor. The static load-deflection test setup and instrumentation is shown in Figure B-1. The test setup of load deflection test is similar to the test setup described in [65]. The bearing housing is mounted on a rigid dummy shaft which is constrained at both ends by a pair of V-blocks (the dummy shaft diameter is equal to the bearing journal diameter 49 mm). V-blocks are bolted to table to insure that no shaft deflection occurs during the load-deflection test. Horizontal static load is applied to the bearing housing through a loading mechanism consists of a long threaded rod that rotates inside a fixed pedestal. At the other end of the threaded rod, a piston-cylinder mechanism converts the rotating motion of the threaded rod into a linear motion. A strain gauge type load cell, connected to the bearing housing, measures the applied static load. An eddy current proximity probe, bolted to the table on the opposite side of the load cell, measures the linear motion of the bearing housing along the loading direction.

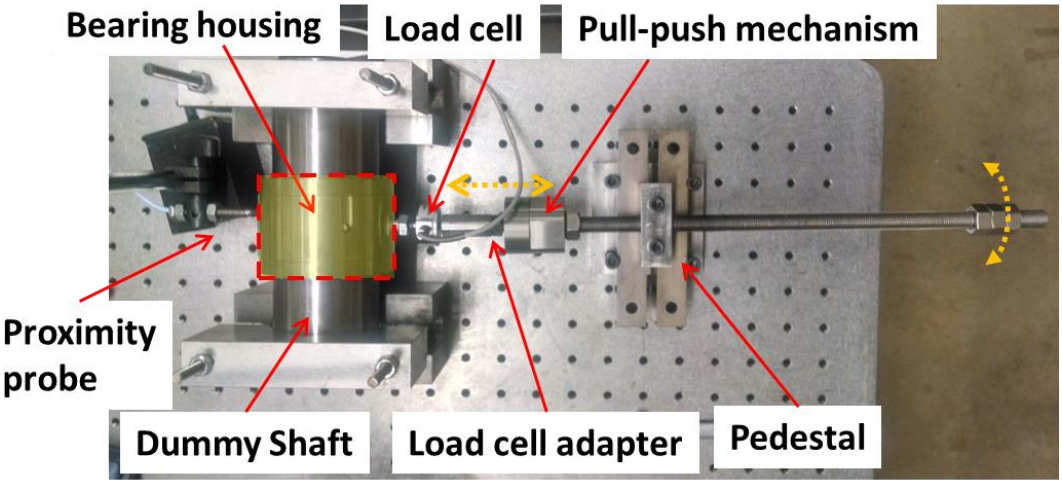

Figure B-1 Load-deflection test setup

For each load-deflection test, four loading/unloading cycles are applied to the test bearing, and the static loads and the corresponding displacements are recorded. Figure B-2 shows the load-displacement plot for the case-1 single-pad HAFB after 4 loading/unloading cycles.

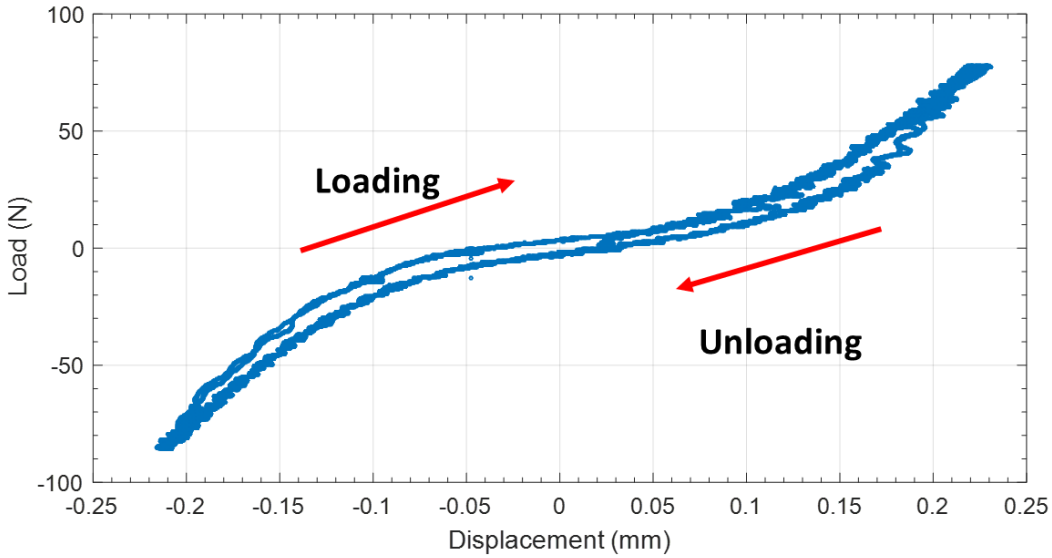

Figure B-2 Load-displacement curve for case-1 single-pad HAFB

Load-displacement curve can be expressed as a third order polynomial;

$$F = k_1 x + k_2 x^2 + k_3 x^3 + k_4 \tag{7-1}$$

, where F is the applied load, x is the displacement of bearing housing, and $\{k_i\}_{i=1,2,3,4}$ is a polynomial constant determined from the test data. The polynomials for loading and unloading cycles, for the above load-deflection tests (Figure B-2), is given in Table 7.

The static structural stiffness of the test bearing is calculated by integrating the load-displacement polynomial, and it is expressed as

$$K = \frac{\partial F}{\partial x} = k_1 + 2k_2 x + 3k_3 x^2 \tag{7-2}$$

Figure B-3 shows the plot of measured static structural stiffness versus the bearing housing displacement.

Table 7 Load-displacement curve polynomial

Force direction	Load-displacement polynomial
Loading	$F = (1.26\times10^{5})x - (2.798\times10^{8})x^{2} + (5.263\times10^{12})x^{3} + 5.773$
Unloading	$F = (1.122\times10^{5})x - (1.129\times10^{8})x^{2} + (5.726\times10^{12})x^{3} - 3.91$

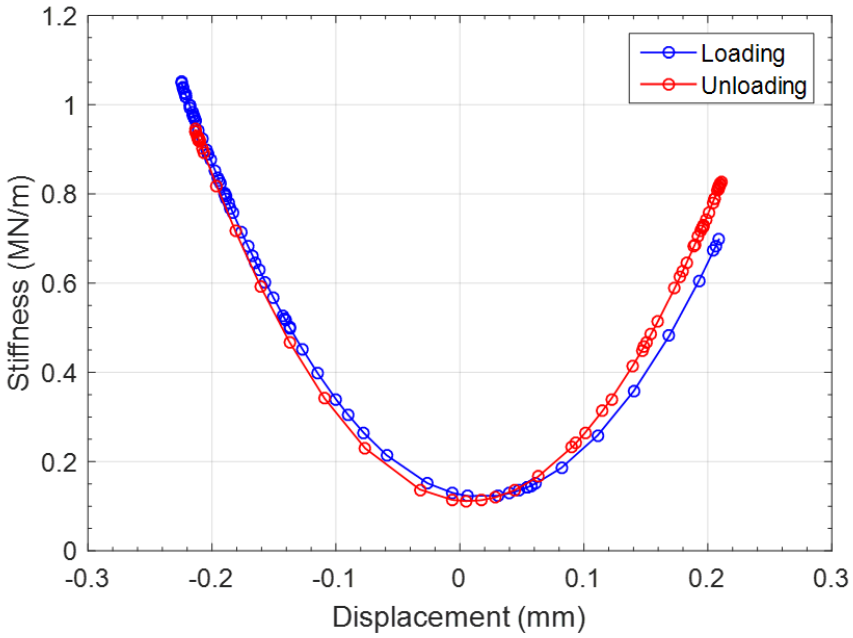

Figure B-3 Measured static structural stiffness vs. displacement for case-1 single-pad HAFB

The static linear stiffness of HAFB is measured by finding the slope of a tangent line on the force-displacement curve. The linear structural stiffness is measured to be

around 1.0 MN/m. Flat region in the load-displacement curve represents the bearing clearance. As it is shown in Figure B-4, the radial clearance of case-1 single-pad HAFB is measured to be 0.05 mm.

The hysteresis loop in the load-deflection curve is used to predict the HAFB structural loss factor. The static structural loss factor (η) is defined as;

$$\eta = \frac{\Delta W}{K \pi X_{\max}^2} \tag{7-3}$$

, where ΔW is the dissipated energy by the bump foils and it is equal to the area inside the hysteresis loop. K is the static linear stiffness, and $X_{\max}$ is the maximum static displacement. From the hysteresis curve, the measured loss factor for the case-1 single-pad HAFB is equal to 0.193

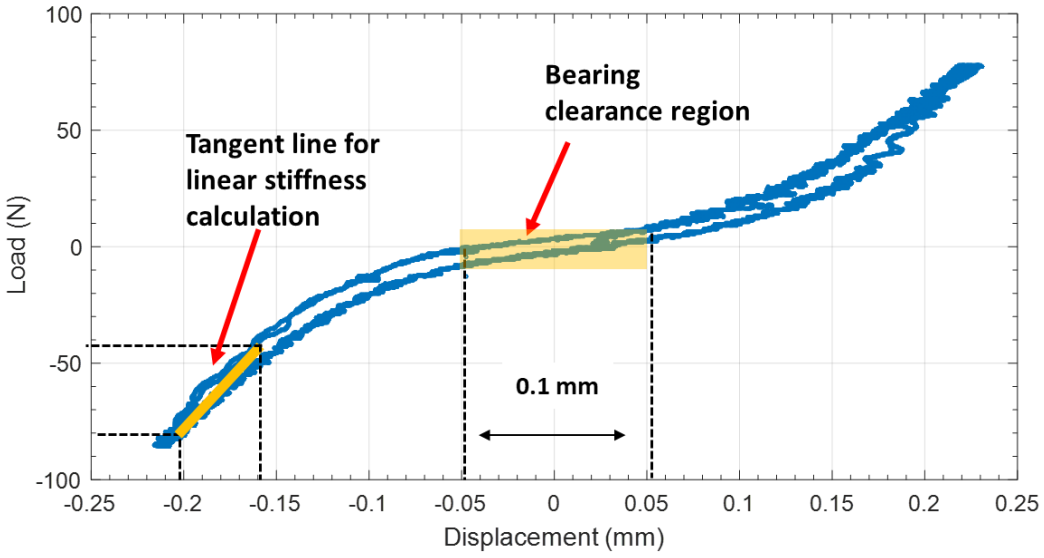

Figure B-4 Measured linear stiffness and radial clearance from the load-displacement curve

REFERENCES

[1] DellaCorte, C., 1997, "A New Foil Air Bearing Test Rig for use to 700 ºC and 70,000 Rpm", NASA Technical Memorandum 107405, .

[2] Visser, W. P. J., Shakariyants, S., de Later, M. T. L., 2012, "Performance Optimization of a 3kW Microturbine for CHP Applications", Proceedings of the ASME Turbo Expo 2012: Turbine Technical Conference and Exposition, Copenhagen, Denmark, June 11–15, 2012, Paper No. GT2012-68686.

[3] Valco, M. J., and DellaCorte, C., 2002, "Emerging Oil-Free Turbomachinery Technology for Military Propulsion and Power Applications", Proceedings of the 23rd US Army Science Conference, Anonymous Fort Lauderdale, FL, .

[4] Heshmat, H., and Hermelb, P., 1993, "Compliant Foil Bearings Technology and their Application to High Speed Turbomachinery", Thin Films in Tribology, Proceedings of the 19th Leeds-Lyon Symposium on Tribology, pp. 559-575.

[5] Capstone Turbine Corporation, 2017, "The Capstine Microturbine," Capstone Turbine Corporation, Chatsworth, CA, .

[6] Bladon Jets, 2017, "Bladon Jets Micro Gas Turbine Gensets," Bladon Jets, Coventry, UK,.

[7] Agnew, G., Bozzolo, M., Moritz, R., R., 2005, " The Design and Integration of the Rolls-Royce Fuel Cell Systems 1MW SOFC", Proceedings of the ASME Turbo Expo 2005: Power for Land, Sea, and Air, Reno, Nevada, USA, June 6–9, 2005, Paper No. GT2005-69122,.

[8] Mueller, F., Gaynor, R., Auld, A., E., 2008, "Synergistic Integration of a Gas Turbine and Solid Oxide Fuel Cell for Improved Transient Capability", Journal of Power Sources, 176(1) pp. 229-239.

[9] Tucker, D., Lawson, R., VanOsdol, J., 2006, "Examination of Ambient Pressure Effects on Hybrid Solid Oxide Fuel Cell Turbine System Operation using Hardware Simulation", Proceedings of the ASME Turbo Expo 2006: Power for Land, Sea, and Air Barcelona, Spain, May 8–11, 2006, Paper No. GT2006-91291.

[10] Feng, K., Liu, W., Yu, R., 2017, "Analysis and Experimental Study on a Novel Gas Foil Bearing with Nested Compression Springs", Elsevier J. Tribol. Int., pp. 65-76.

[11] Song, J., and Kim, D., 2007, "Foil Gas Bearing with Compression Springs: Analyses and Experiments", ASME J. Tribol, 129(3) pp. 628-639.

[12] Ertas, B. H., 2008, "Compliant Hybrid Journal Bearings using Integral Wire Mesh Dampers", ASME J. Eng. Gas Turbines Power, 131(2) pp. 022503-022514.

[13] San Andrés, L., and Chirathadam, T. A., 2012, "A Metal Mesh Foil Bearing and a Bump-Type Foil Bearing: Comparison of Performance for Two Similar Size Gas Bearings" ASME J. Eng. Gas Turbines Power, 134(10) pp. 102501.

[14] Feng, K., Liu, Y., Zhao, X., 2016, "Experimental Evaluation of the Structure Characterization of a Novel Hybrid Bump-Metal Mesh Foil Bearing" ASME J. Tribol, 138(2) pp. 021702.

[15] Chirathadam, T.A., 2012, "Metal mesh foil bearings: prediction and measurement of static and dynamic performance characteristics", Master Thesis, Texas A&M University, .

[16] San Andres, L.,Chirathadam, T.A., 2010, "Identification of Rotordynamic Force Coefficients of a Metal Mesh Foil Bearing using Impact Load Excitations", ASME J. Eng. Gas Turbines Power 133(11), 112501.

[17] Lee, Y., Kim, C. H., Kim, T. H., 2011, "Effects of Mesh Density on Static Load Performance of Metal Mesh Gas Foil Bearings", ASME J. Eng. Gas Turbines and Power, 134(1) pp. 012502-012510.

[18] DellaCorte, C., Radil, K. C., Bruckner, R. J., 2008, "Design, Fabrication, and Performance of Open Source Generation I and II Compliant Hydrodynamic Gas Foil Bearings", STLE J. Tribol. Trans., 51(3) pp. 254-264.

[19] DellaCorte, C., and Edmonds, B.J., 1995, "Preliminary Evaluation of PS300: A New Self-Lubricating High Temperature Composite Coating for Use to 800 C", NASA Lewis Research Center, NASA-TM-107056, Cleveland, OH, United States.

[20] DellaCorte, C., Lukaszewicz, V., Valco, M., 2000, "Performance and Durability of High Temperature Foil Air Bearings for Oil-Free Turbomachinery", STLE J. Tribol. Trans., 43(4) pp. 774-780.

[21] Stanford, M.K., Yanke, A.M., and DellaCorte, C., 2004, "Thermal Effects on a Low Cr Modification of PS304 Solid Lubricant Coating", NASA Glenn Research Center, NASA/TM-2004-213111, Cleveland, OH, United States.

[22] DellaCorte, C., and Valco, M. J., 2000, "Load Capacity Estimation of Foil Air Journal Bearing for Oil-Free Turbomachinery Application", STLE Tribol. Trans., 43(4) .

[23] Kim, D., 2007, "Parametric Studies on Static and Dynamic Performance of Air Foil Bearings with Different Top Foil Geometries and Bump Stiffness Distributions", ASME J. Tribol., 192(2) pp. 354-364.

[24] Bruckner, R. J., and Puleo, B. J., 2008, "Compliant Foil Journal Bearing Performance at Alternate Pressures and Temperatures", Proceedings of the ASME Turbo Expo 2008: Power for Land, Sea, and Air, Berlin, Germany, June 9–13, 2008, Paper No. GT2008-50174.

[25] DellaCorte, C., Radil, K. C., Bruckner, R. J., 2006, "A Preliminary Foil Gas Bearing Performance Map" .

[26] Radil, K. C., and Dellacorte, C., 2010, "A Three-Dimensional Foil Bearing Performance Map Applied to Oil-Free Turbomachinery", Tribology Transactions, 53(5) pp. 771-778.

[27] Radil, K., Howard, S., A., and Dykas, B., 2002, "the Role of Radial Clearance on the Performance of Foil Air Bearings," STLE Tribol. Trans,, 45(4) pp. 485-490.

[28] Dykas, B., and Howard, S. A., 2004, "Journal Design Considerations for Turbomachine Shafts Supported on Foil Air Bearings", STLE J. Tribol. Trans., 47(4) pp. 508-516.

[29] Shrestha, S. K., Kim, D., and Kim, U. C., 2013, "Experimental Feasibility Study of Radial Injection Cooling of Three-Pad Air Foil Bearings", ASME J. Tribol., 135(4) .

[30] Radil, K., and Batcho, Z., 2011, "Air Injection as a Thermal Management Technique for Radial Foil Air Bearings", STLE J. Tribol. Trans., 54(4) pp. 666-673.

[31] Heshmat, H., and Ku, C., 1992, "Compliant Foil Bearing Structural Stiffness Analysis: Part I—theoretical Model Including Strip and Variable Bump Foil Geometry", ASME J. Tribol., 114(2) pp. 394-401.

[32] Ku, C. P., and Heshmat, H., 1994, "Structural Stiffness and Coulomb Damping in Compliant Foil Journal Bearing: Parametric Studies", STLE Tribol. Trans., 37(3) pp. 455-462.

[33] Peng, J., and Carpino, M., 1994, "Coulomb Friction Damping Effects in Elastically Supported Gas Foil Bearings", STLE Tribol. Trans., 37(1) pp. 91-98.

[34] Ku, C. R., and Heshmat, H., 1993, "Compliant Foil Bearing Structural Stiffness Analysis-Part II: Experimental Investigation", ASME J. Tribol., 115pp. 364-364.

[35] Heshmat, H., and and Ku, C., 1994, "Structural Damping of Self-Acting Compliant Foil Journal Bearing", ASME J. Tribol., 116pp. 76-82.

[36] Rubio, D., and San Andres, L., 2007, "Structural Stiffness, Dry Friction Coefficient, and Equivalent Viscous Damping in a Bump-Type Foil Gas Bearing", ASME J. Eng. Gas Turbines and Power, 129(2) pp. 494-502.

[37] Salehi, M., Heshmat, H., and Walton, J. F., 2003, "On the Frictional Damping Characterization of Compliant Bump Foils", ASME J, Tribol., 125(4) pp. 804-813.

[38] Howard, S. A., 1999, "Preliminary Development of Characterization Methods for Compliant Air Bearings", STLE Tribol. Trans., 42(4) pp. 789-794.

[39] Howard, S. A., Dellacorte, C., Valco, M. J., 2001, "Steady-State Stiffness of Foil Air Journal Bearings at Elevated Temperatures," Tribology Transactions, 44(3) pp. 489-493.

[40] Howard, S., Dellacorte, C., Valco, M. J., 2001, "Dynamic Stiffness and Damping Characteristics of a High-Temperature Air Foil Journal Bearing", STLE Tribol. Trans., 44(4) pp. 657-663.

[41] Gray, S., 1982, "Development of Foil Journal Bearings for High Load Capacity and High Speed Whirl Stability", Journal of Lubrication Technology APRIL, 104pp. 149.

[42] San Andrés, L., Rubio, D., and Kim, T. H., 2007, "Rotordynamic Performance of a Rotor Supported on Bump Type Foil Gas Bearings: Experiments and Predictions", ASME J. Eng. Gas Turbines and Power, 129(3) pp. 850-857.

[43] Balducchi, F., Arghir, M., and Gaudillere, S., 2014, "Experimental Analysis of the Unbalance Response of Rigid Rotors Supported on Aerodynamic Foil Bearings", ASME J. Vib. Acoust 137(6), 061014.

[44] Kim, T. H., and San Andrés, L., 2009, "Effect of Side Feed Pressurization on the Dynamic Performance of Gas Foil Bearings: A Model Anchored to Test Data", ASME J. Eng. Gas Turbines and Power, 131(1) pp. 012501.

[45] Sim, K., Koo, B., Lee, J. S., 2014, "Effects of Mechanical Preloads on the Rotordynamic Performance of a Rotor Supported on Three-Pad Gas Foil Journal Bearings", ASME J. Eng. Gas Turbines and Power, 136(12) pp. 122503.

[46] LaTray, N., and Kim, D., 2017, "Rotordynamic Performance of a Shaft with Large Overhung Mass Supported by Foil Bearings", ASME J. Eng. Gas Turbines Power, 139(4) pp. 042506.

[47] Kim, D., and Park, S., 2009, "Hydrostatic Air Foil Bearings: Analytical and Experimental Investigation", Tribol. Int., 42(3) pp. 413-425.

[48] Kim, D., and Zimbru, G., 2011, "Start-Stop Characteristics and Thermal Behavior of a Large Hybrid Airfoil Bearing for Aero-Propulsion Applications", ASME J. Eng. Gas Turbines and Power, 134(3) .

[49] Kumar, K., and Kim, D., 2008, "Parametric Studies on Dynamic Performance of Hybrid Airfoil Bearing", ASME J. Eng. Gas Turbines and Power, 130(6) .

[50] Wang, Y. P., and Kim, D., 2014, "Experimental Identification of Force Coefficients of Large Hybrid Air Foil Bearings", ASME J. Eng. Gas Turbines and Power, 136(3) pp. 032503.

[51] Yazdi, B. Z., Kim, D., and Xu, F., 2016, "Enhancement of the Rotordynamic Performance of a Shaft Supported by Air Foil Bearings With Vibration Damper", Proceedings of ASME Turbo Expo 2016: Turbomachinery Technical Conference and Exposition, Anonymous American Society of Mechanical Engineers, .

[52] Turbomachinery and Energy Systems Laboratory, The University of Texas at Arlington, 2017, "Turbomachinery and Energy Systems Laboratory Hybrid Air Foil Bearing", Arlington, Texas, .

[53] Feng, K., Li, W., Deng, Z., 2016, "Thermohydrodynamic Analysis and Thermal Management of Spherical Spiral Groove Gas Bearings", STLE J. Tribol. Trans., pp. 1-16.

[54] Mori, H., and Miyamatsu, Y., 1969, "Theoretical Flow-Models for Externally Pressurized Gas Bearings", ASME J. Lubr. Technol., 91(1) pp. 181-193.

[55] Han, D., Park, S., Kim, W., 1994, "A Study on the Characteristics of Externally Pressurized Gas Bearings", Precision Engineering, 16(3) pp. 164-173.

[56] Kumar, M., and Kim, D., 2010, "Static Performance of Hydrostatic Air Bump Foil Bearing", Tribol. Int., 43(4) pp. 752-758.

[57] Kim, D., and Varrey, M. K., 2012, "Imbalance Response and Stability Characteristics of a Rotor Supported by Hybrid Air Foil Bearings", STLE Tribol. Trans., 55(4) pp. 529-538.

[58] Horikawa, O., Sato, K., and Shimokohbe, A., 1992, "An Active Air Journal Bearing", Nanotechnology, 3(2) pp. 84.

[59] Mizumoto, H., Arii, S., Kami, Y., 1996, "Active Inherent Restrictor for Air-Bearing Spindles", Elsevier J. Prec. Eng., 19(2-3) pp. 141-147.

[60] San Andrés, L., and Ryu, K., 2008, "Hybrid Gas Bearings with Controlled Supply Pressure to Eliminate Rotor Vibrations while Crossing System Critical Speeds", ASME J. Eng. Gas Turbines Power, 130(6) pp. 062505.

[61] Pierart, F. G., and Santos, I. F., 2016, "Adjustable hybrid gas bearing–Influence of piezoelectrically adjusted injection on damping factors and natural frequencies of a flexible rotor operating under critical speeds", Proceedings of the Institution of Mechanical Engineers, Part J: Journal of Engineering Tribology, Anonymous SAGE Publications Sage UK: London, England, 230, pp. 1209-1220.

[62] Kim, D., Lee, A. S., and Choi, B. S., 2014, "Evaluation of Foil Bearing Performance and Nonlinear Rotordynamics of 120 Kw Oil-Free Gas Turbine Generator" ASME J. Eng. Gas Turbines Power, 136(3) pp. 032504.

[63] Kumar, M., 2009, "Analytical and Experimental Investigations of Hybrid Air Foil Bearings", MS Thesis, Texas A&M University, College Station, TX.

[64] Gudemane, S., 2014, "Rotordynamic Performance of A Rotor Supported by Three Pad Hybrid Foil Bearings with Controlled Air Injection", M.S. Thesis, the University of Texas at Arlington, Arlington, TX.

[65] Yazdi, B. Z., Kim, D., Xu, F., 2016, “Enhancement of the Rotordynamic Performance of a Shaft Supported by Air Foil Bearings with Vibration Damper”, Proceedings of the ASME Turbo Expo 2016: Turbomachinery Technical Conference and Exposition, Seoul, South Korea, June 13–17, 2016, Paper No. GT2016-56790, pp. V07BT31A021; 8 pages.

BIOGRAPHICAL INFORMATION

Behzad Zamanian Yazdi received his Bachelor degree in Mechanical Engineering from Azad University of Mashhad, Iran in 2012. He joined the Turbomachinery and Energy systems Laboratory guided by Dr. Daejong Kim while pursuing his PhD program in Mechanical Engineering at the University of Texas at Arlington in 2012. He joined the Energy Recovery Inc. as a Mechanical Engineer in 2017.